PRACTICAL ANALYSIS OF RIVER FLOWS AROUND SELECTED HYDRAULIC STRUCTURES

AL HINAI SAIF SAID SALAM

2010

PRACTICAL ANALYSIS OF RIVER FLOWS AROUND SELECTED HYDRAULIC STRUCTURES

AL HINAI SAIF SAID SALAM

Department of Urban Management
Kyoto University

November, 2010

ABSTRACT

The goal of this study is to investigate and analyze the flow patterns around selected hydraulic structures. One-dimensional and two-dimensional physical, mathematical, and numerical models are the main tools used to achieve the aim of this research. In some topics included in this thesis, verifications between the three models were made.

Firstly, we applied a one-dimensional numerical model to a flume which contains two backward-facing steps. Flow features such as the formation of the hydraulic jump downstream the step is studied by this model. The model is tested under different grid sizes. Although, numerical oscillations occurred, the model with smaller grid size is capable to reproduce the creation of the hydraulic jumps downstream the backward-facing steps.

The study of the flow over backward-facing steps is extended by conducting a fundamental study of the flow subjected to sudden change in the geometry of the channel due to the existence of a single backward-facing step and the abrupt expansion immediately downstream the step. The oblique shockwaves generated downstream the step is represented clearly by establishing a two-dimensional numerical model applied in a curvilinear grid.

The two-dimensional numerical model which is used to simulate the flow over a single backward-facing step is applied again simultaneously with a bed-load sediment transport model. It is used to study the sediment deposition downstream the step, in addition to the formation of alternate sand patterns in the Kamo River. The alternate sandbars formation along the river course, and the triangular shape sandbars downstream the steps are represented. An emphasis is given to the effect of these sandbars in the habitat of the Kamogawa-chidori birds which is the bare bar surfaces.

Theoretical investigation is conducted by using the linearlized equations of two-dimensional (2-D) shallow flows to study the spatial variations of steady open channel flows downstream of an obstacle attached on the sidewall of a flume. The periodic wavy patterns, the standing waves, and the relation between Froude number and the attenuation rate are considered. The theoretical results are verified with hydraulic experiments and a two-dimensional numerical model executed under the experiments conditions.

Some of the arid countries such as Oman are destroyed with severe flash floods in the last few years. Such floods are usually caused by excessive rainfalls in a short period of time, and they created hazardous situations for people and cause severe damages to properties. In this research, we concerned in the possibility to reproduce flash floods with a high Froude number, by using one depth hydrograph at one site. A long mathematical process considering both linear and nonlinear solutions is discussed in details in chapter six of this thesis.

The study of flash floods is continued in this thesis, by dealing with the existence of box culverts at dry rivers “wadies” during flash floods in Oman. A two-dimensional numerical model is established and executed under observed conditions, in order to represent flow during flash floods under highways in Oman. Backwater effects and overflows from culvert are considered with giving more attention to the interaction between open channel free surface flow and pressurized flow inside the box culvert.

ACKNOWLWDGEMENT

The research work in this thesis has been carried out through the financial support from the Japanese Government Scholarships “Monbusho”, conducted at the River System Engineering and Management Laboratory, Department of Urban Management, Kyoto University. First, I want to thank my God “ALLAH” for allowing me to complete the work in this thesis successfully.

I express my deep and sincere gratitude to my supervisor, Professor Dr. Takashi Hosoda, for his help, support, guidance and encouragement throughout the completion of this work. My warm and sincere thanks are also expressed to Professor Dr. Marko Ivetic who helped and advised me to come and study in Kyoto University.

Beside my advisor, I would like to thank the review committee of this thesis, Professor Dr. Keiichi Toda and Associate Professor Dr. Kenji Kawaike for their valuable comments and discussions of the contents of this research. I am appreciating their effort and patience to complete the review of the dissertation.

Special thanks to the members in the River System Engineering and Management Sub-department: Associate Professor Dr. Kiyoshi Kishida and Assistant Professor Dr. Shinichiro Onda for their technical support and the pleasant working environment they provided. I am especially thankful to my senior research colleague Lecturer Dr. Puay How Tion and to all the students in the laboratory, especially Mr. Fredeick Malembeka Paul, Mr. Manoj Langhi and Mr. Hidekzu Shiari, for fruitful discussions and assistance over many issues.

Special thanks to my dear colleagues and friend in the Ministry of Regional Municipalities and Water Resources in Oman, Dr. Abdulaziz Al-Mahikhi, Eng. Fahad Al-Farsi, Mr. Saif Al-Mamary, Mr. Khalid Al-Kharoosi, Mr. Badr Al-Rawahi and all the staffs in the Ministry for taking my responsibilities there, during my stay in Japan.

I owe my loving thanks to my parents Said and Sabiha, for their support and caring. Their patience while their son studied on the other side of the world is much appreciated, as is everything else they have done for me. I am much indebted to my lovely wife Maryam and my kids Nawras, Khalid, Abdulaziz and Reem for their love, support and patience during the years of the thesis preparation. My loving thanks are due to my brothers and sisters in Oman.

Lastly, I am taking this opportunity to apologize to all of those who supported me in any respect and I have inadvertently omitted from the list.

PREFACE

The content of this thesis includes the contents of the following published and/or submitted papers:

A. Saif, T. Hosoda and H. Shirai (2011). Numerical modeling of unsteady flow around a box culvert and its verification. Annual Journal of Hydraulic Engineering, JSCE. (accepted)

H. Shirai, T. Hosoda and A. Saif (2011). Possibility of reproducing flash floods using one water hydrograph at one site (in Japanese). Annual Journal of Hydraulic Engineering, JSCE. (accepted)

T. Hosoda, A. Saif, H. T. Puay and Y. Kouchi (2010). Some considerations on spatial variations in steep channels with an obstacle at one side wall (in Japanese). Journal of Applied Mechanics, JSCE, Vol. 13, pp. 761-768.

T. Hosoda, A. Saif, H. T. Puay and Y. Kouchi (2010). Spatial water surface variations in open channel flows downstream of side disturbance. Proceeding of the International Conference on Fluvial Hydraulics (River Flow 2010), Braunschweig, Germany, 8-10 September 2010, Vol. 1, pp. 659-664.

A. Saif, T. Hosoda, S. Onda and R. Shigemitsu (2009). Relation between sand bar formation and the habitat of "Kamogawa Chidori" in the Kamo River, Kyoto. Proceeding of the 6th IAHR Symposium on River, Coastal and Estuarine Morphodynamics (RCEM 2009), Santa Fe, Argentina, 21-25 September 2009, Vol. 2, pp. 549-554.

CONTENTS

LIST OF FIGURES

LIST OF TABLES

Chapter 1

INTRODUCTION

1.1 Preliminaries

The study of the flow over and around hydraulic structures is an interested field for civil engineers. Every hydraulic structure has its own benefits in urban areas. For example, dams, which protect from floods and store water for water supply, and sluice gates which are used to control the discharge in rivers and to alleviate flooding. Bridges and culverts, which carry roads and railways over rivers, are very numerous examples of hydraulic structures; few roads are constructed without them. Concrete weirs are used to measure the discharge of rivers. For the purposes of regulating water flow and river sedimentation, backward-facing steps is the major solution of such problems. Beside the advantages of constructing such hydraulic structures, there are many negative effects on rich river natures. Some ecological changes in the ecosystem of the rivers occurred such as the rapid decrease in the number of fishes, birds and trees in these rivers.

This research is giving focuses in some of the hydraulic structures that mentioned above. The flow behavior around these structures is analyzed by using mathematical, physical and numerical models. Flow features caused by the existence of these structures, such as oblique shockwaves and hydraulic jumps are emphasized in more details.

Flow separation by backward-facing steps is the main topic that this study will concentrate on. There are several investigations of flow over a backward-facing step available in the literature. For example, Denham and Patrick (1974) conducted experiments on laminar flow over a backward-facing step. Reattachment lengths and velocity profiles were measured in the study. Armaly et al. (1983) provided data on separation and reattachment points, stream-wise velocity measurements are reported for several Reynolds numbers. Ghia et al. (1989) computed two-dimensional solutions of the backward-facing step flow throughout the laminar regime and found a good agreement with the two-dimensional flows observed by Armaly et al. (1983).

The flow disturbance can be generated by changing flow depth and/or velocity in a section of flow. In this research, an obstacle attached to the sidewall of a flume is the source of the flow disturbance, with giving an attention to the spatial variations of steady open channel flows downstream the obstacle. Struiksma et al. (1985) formulated the spatial amplification of the sandbars generated downstream of a point-bar along a river bend "over-deepening phenomenon of sandbars" mathematically, and derived the critical conditions for the spatial amplification of sandbars. The analytical solution on the temporal change of point-bars in a sinuous meandering channel is derived by Blondeaux and Seminara (1985), by studying the resonance relation between sinuous channel and bars. It is well known nowadays that the condition of the spatial amplification of bars by Struiksma et al. (1985) is coincident with the resonance relation by Blondeaux and Seminara (1985). Hosoda and Nishihama (2006) studied the response of water surface to a sinuous open channel and the flow behavior near the resonance condition. Although there is no resonance condition in the case studied in this paper, it is pointed out that if the bottom variations with the standing wave condition are given, the flow resonates to the bottom variations. Based on these researches, this study doesn't deal with the spatial amplification of sandbars, but it examined the response of the spatial variations of water surface in steady open channel flows downstream of an obstacle attached on the sidewall of a flume.

Flash floods are considered as one of the most dangerous weather-related natural disasters in the world, and can create hazardous situations for people and cause extensive damage to property. They are usually caused by heavy or excessive rainfall in a short period of time. Physical and numerical models are useful in analyzing floods especially in catchments where data is not available for simulating extreme storms. The use of these models is necessary in the urban watershed with high variability of land surface parameters, and absence of calibration data. On the other hand, uncertainty should be taken in account in analyzing the results in such cases. In this study, we concerned with the reproduction of flash floods with a high Froude number by testing the possibility of reproducing such flows by using one depth hydrograph at one site.

Flash floods in arid environments such as Oman are in fact common, but their occurrence is also poorly understood. In such floods we have to deal with dry rivers except in rainy seasons “wadies”. These wadies were intersected with a number of streets, where culverts and bridges have been constructed to provide road flood protection. Box culverts were very common used in Oman to allow water to pass under highways and to carry watercourses under built-up areas. In many cases Muscat City (the capital of Oman) is flooded because the culverts capacity was insufficient to carry large flood flows. A part from this study deals with a numerical model to simulate flow through a box culvert, which represents flow during flash floods under highways in Oman.

1.2 Objectives of Study

The main objective of this study is to investigate a mean of using hydraulic models to better reproduce and quantify some flow features that generated around selected hydraulic structures within river reaches. It is anticipated that the results of such study will provide a tool better linking the hydraulic characteristics of river to the ecological attributes of a stream. Such connection would allow for better investigating how hydrologic parameters drive the hydraulic and morphologic conditions and how consequent hydraulic conditions influence stream ecology. Thus, engineers, ecologists can have a general set of tools, which they can use to describe the flow patterns of importance of their particular studies.

In this study, hydraulic models used in calculating various flow parameters can be listed as:

1. To analyze flow features such as V-shaped oblique shockwaves and hydraulic jumps downstream backward-facing step structures.

2. To make clear the mechanism of the creation of sandbars with triangular shapes downstream the steps, and the alternate sandbars along river course.
3. To study the spatial variations of free surface flows downstream a sidewall attached obstacle.
4. To represent flow during flash floods under highways in arid environments.

Another purpose of this study is to provide a methodology for better reproducing flash floods with less available data, by introducing a theoretical method focusing on the possibility of reproducing flash floods using only one water hydrograph. However, a detailed case study applying this theory is not the main objective here, and authors believe that it will be a great challenge to future researches in this field.

1.3 Thesis Structure and Organization

Eight chapters are included in this manuscript which concerned on the practical analysis of river flows around selected hydraulic structures, including the introduction in chapter one and the conclusion in chapter eight. The structure organization of this thesis is illustrated in the flowchart in Figure 1.1

In chapter two, we used one-dimensional numerical model to analyze the flow over multi backward-facing steps by giving more attention to the hydraulic jumps which formed downstream the steps. The effect of the grid size is tested to avoid the oscillation at the immediate downstream of the step and to reproduce the hydraulic jump in a proper way. Flow over drops “water-free-fall” also studied in terms of the pool behind the free-fall. The numerical simulated results are verified with experiments conducted by the author.

In chapter three, study of flow over backward-facing steps is extended with more emphasis on the flow features such as shockwaves and hydraulic jump downstream the step, which shaped due to the abrupt changes in the flow cross section. A depth-averaged two-dimensional numerical model for unsteady flow in open channel is established using the finite volume method on a curvilinear grid. The shockwaves generated downstream the step can be represented clearly by using this model. The backwater effect due to the increase of the water depth downstream the step is also considered. Flow under partially-submerged and fully-submerged steps is also studied experimentally and numerically. The depth of the supercritical stream immediately downstream the free-over-fall is considered and verified with previous predicted results.

Chapter four presents the ecological changes on the ecosystem of the Kamo River by studying the relation between the habitat of an endangered bird called Kamogawa-Chidori (Charadrius Placidus) and the sandbar formation in the immediate downstream of backward-facing step structures with small abrupt expansion at a few locations of the river course. The computational model with a two-dimensional (2D) simulation of flow and sediment transport was applied to the bar formations in order to make clear the mechanism of the sand deposition in the immediate downstream of step. The results can give an approximate reproduction of the sand deposition downstream the backward-facing steps structures in the Kamo River.

Chapter five deals with the spatial variations of steady open channel flow downstream of an obstacle attached on the sidewall of a flume. Theoretical analysis is applied using the linearlized equations of two-dimensional shallow flows. The theoretical results are verified by hydraulic experiments and a two-dimensional numerical model executed under the hydraulic experiments.

The reproduction of flash floods with high Froude number is concerned in chapter six by testing the possibility that such flows can be reproduced by using one depth hydrograph at one site. Linear analytical solution can be derived when the boundary conditions at upstream are linear functions of time. If the boundary conditions at upstream are quadratic functions of time, nonlinearity was taken in account.

Chapter seven deals with a numerical model to simulate the flow through a box culvert, which represents flow during flash floods under highways in Oman. We firstly show the typical flow patterns with the transition from free surface flows to pressurized flows and overflows over a culvert, based on hydraulic experiments. Then, a numerical model applicable to the full/partial full pressurized flows is tested to simulate the typical flow patterns under the conditions of experiments.

Chapter eight summarizes the overall results and conclusions presented in this research. Some recommendations of further researches are mentioned in this chapter.

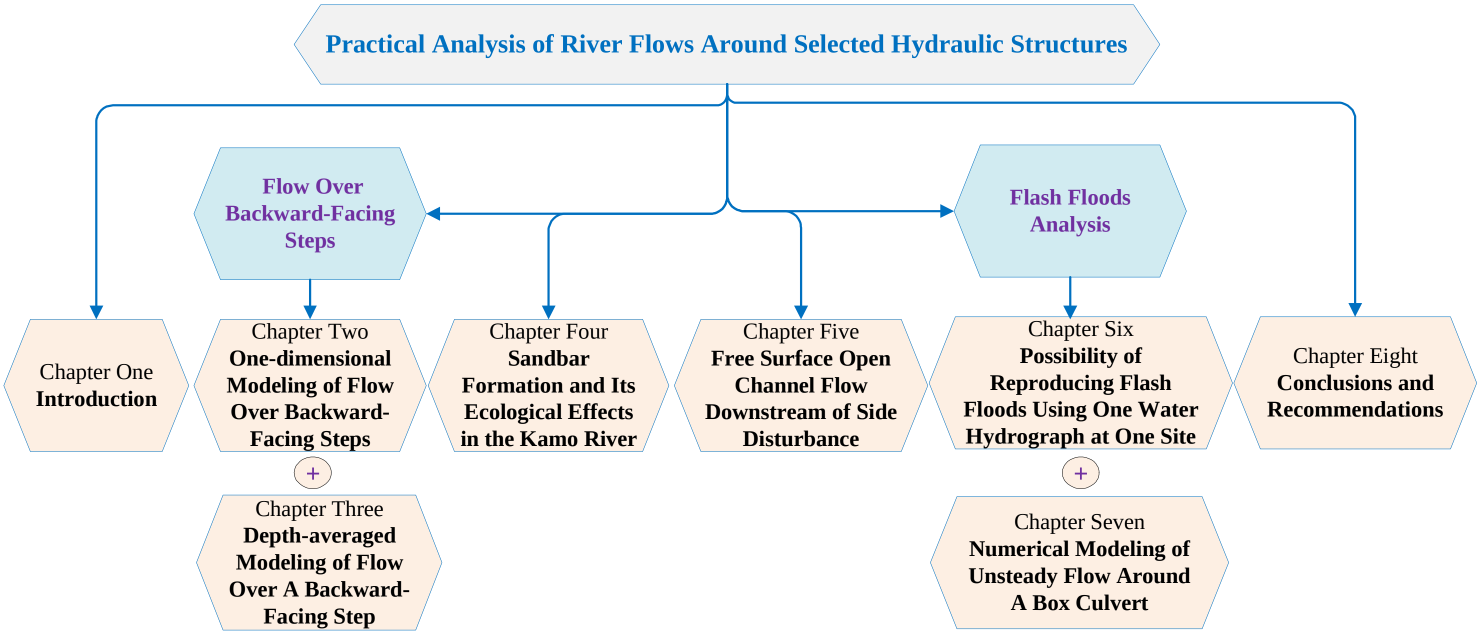

Figure 1.1 Flowchart of the framework of the thesis.

Chapter 2

ONE-DIMENISONAL MODELING OF FLOW OVER BACKWARD-FACING STEPS

2.1 Preliminaries

A free-over-fall or vertical drop from a backward-facing step is a common feature in both natural and artificial channels. Natural drops are formed by river erosion while drop structures are built in irrigation systems to reduce channel slope (Rajaratnam and Chamani, 1995). Investigations on drops started in early times. Some of the published literatures that studied the flow characteristics of drops are Moore (1943), White (1943), Rand (1955), Gill (1979), and Rajaratnam and Chamani (1995). The basic study to the hydraulics of drops was made by Moore (1943) followed by the discussion of White (1943). These studies were mainly focused on the energy loss at the base of drop. White (1943) presented in his discussion a theoretical solution for energy loss at drop. Empirical equations for some of the characteristics of the flow over the over-fall were developed by Rand (1955).

Experimental and Numerical investigations of flow over a backward-facing step are widely available in the literature. For example, Denham and Patrick (1974) conducted experiments on laminar flow over a backward-facing step. Reattachment lengths and velocity profiles were measured in the study. Armaly et al. (1983)

provided data on separation and reattachment points, stream-wise velocity measurements are reported for several Reynolds numbers.

The hydraulic jump is a basic physical phenomenon in natural rivers or open channel flows (Zhou and Stansby, 1999). It is shaped whenever supercritical flow changes to subcritical flow. During this transition, water surface rises suddenly, turbulent mixing occurs, surface rollers are formed and energy is dissipated. Such characteristics are often used for energy dissipation in hydraulic engineering (Hager, 1992). To design a hydraulic structure in which a hydraulic jump is formed, it is necessary to know the location and the length of the hydraulic jump and the amount of energy dissipated (Gharangik and Chaudhry, 1991). To determine the jump location, Chow (1995) computed the water surface profiles for supercritical flows starting from upstream end and the subcritical flow starting from the downstream end, and the jump is formed at the location where the specific forces on both sides of the jump are equal (Gharangik and Chaudhry, 1991).

In this chapter, flow over multi backward-facing steps is studied experimentally and numerically by focusing especially on the formation of the hydraulic jumps downstream the steps. Such phenomenon occurs due to the sudden change of the flow from supercritical to subcritical flow. In addition to the hydraulic jump, the depth of the pool behind the free-fall “Y_P” is also studied in this chapter as illustrated in Figure 2.1. The values of Y_P measured in this study are compared with values predicted by previous literatures.

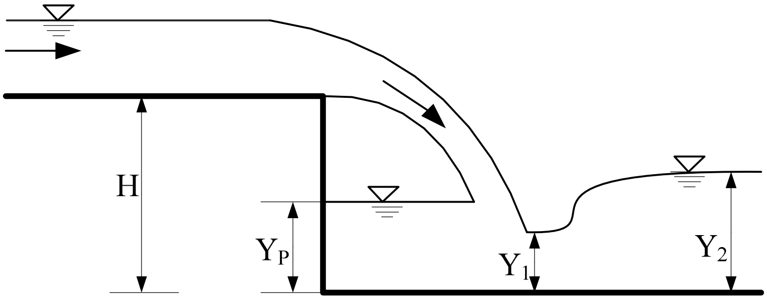

Figure 2.1 Definition sketch for flow over drop.

The one-dimensional unsteady differential equations for conservation of mass and momentum are solved numerically to analyze the formation of the hydraulic jump in a rectangular channel downstream the backward-facing steps. The effect of the grid size Δx in the area downstream the step is considered in order to represent the location of the hydraulic jumps clearly and to study the effect of the numerical oscillation on the water depth at the direct downstream of the step. Three values of Δx were used during the simulation processes are $0.05m$, $0.01m$ and $0.005m$. The experimental results are presented, and the computed results under different grid sizes are verified by comparing them with the observed data.

2.2 Laboratory Tests

The hydraulic experiments were conducted using a horizontal glass rectangular flume having two backward-facing steps. The flume is 300 cm long, 10 cm wide and 10 cm step height as shown in Figure 2.2. The flume is equipped with a gate to control the tailwater depth. A pump lift the water from underground sump to a tank connected with the flume inlet. Water runs through the flume then returns back to a sump tank. The hydraulic variables for the laboratory tests are illustrated in Table 2.1.

Table 2.1 Hydraulic parameters in the laboratory tests.

Run	**H (cm)**	**L (cm)**	**B (cm)**	**Q (cm^3/s)**	**$h_{u/s}$ (cm)**	**$h_{d/s}$ (cm)**	**T (℃)**	**GH (cm)**	**Remarks**	
									$Step_1$	**$Step_2$**
1	10	300	10	333.5	1.5	1.42	22.4	0	*FWF*	*FWF*
2	10	300	10	333.5	1.5	11.36	22.4	10	*FWF*	*FSS*
3	10	300	10	333.5	1.5	16.14	22.4	15	*PSS*	*FSS*

where H: step height; L: length of flow domain; B: channel width; Q: discharge; $h_{u/s}$: water depth at the upstream end of $step_1$; $h_{d/s}$: water depth at the downstream end of $step_2$; T: water temperature; GH: gate height; FWF: free-water-fall; PSS: partially-submerged step; FSS: fully-submerged step.

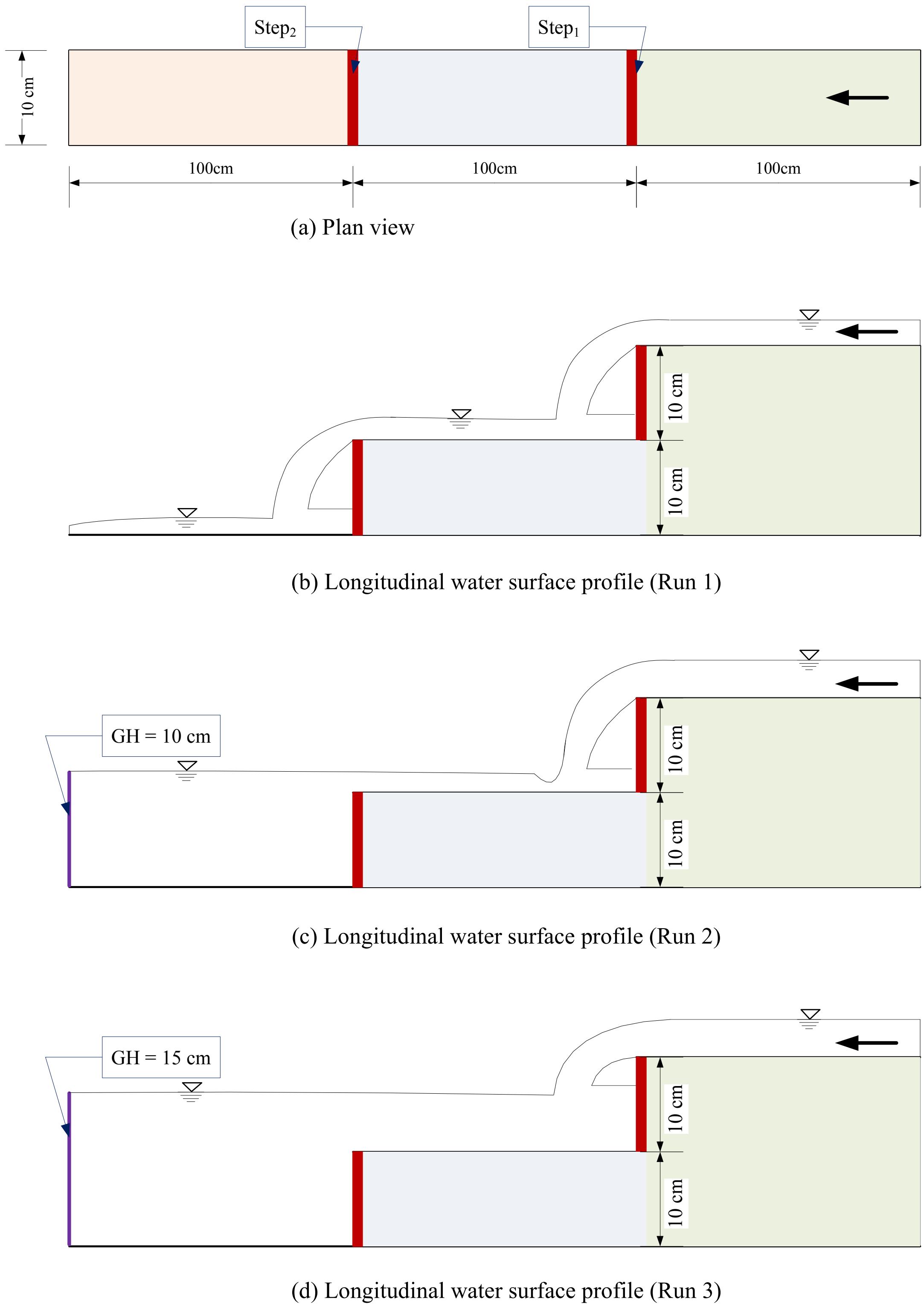

Figure 2.2 Schematic view of the experimental installation.

As shown from Table 2.1 and Figure 2.2, the flume contains two steps with a distance equal 100 cm in between them. The slope in the flume was set to be zero. Three cases are considered during the experiments depending on the water surface elevation around the step. In Run 1, the flow over the step is free-fall in $step_1$ and $step_2$. By increasing the gate height at the downstream end of $step_2$ in Run 2 and Run 3, $step_2$ in both Run 2 and Run 3 is fully-submerged of water, while the flow in $step_1$ is free-water-fall for Run 2 and partially-submerged for Run 3.

2.3 Experiment Results

2.3.1 Surface Water Variation

The laboratory experimental results are shown in Figure 2.3, while the surface water variations along the centerline of the flume are shown in Figure 2.4. Three types of flow over backward-facing steps are taken places depending on the downstream conditions.

The flow conditions in the three cases are almost same. The water depth at the downstream end is adjusted by a moveable gate. The first case (Run 1) was carried out under zero gate height. The gate height in the Run 2 is 10 cm which allowed backwater to take place, which make $step_2$ is fully-submerged with water, while there is free-water-fall over $step_1$. By increasing the gate height further as in Run 3, the backwater affected $step_1$ and become partially-submerged.

As was shown in Figure 2.3 and Figure 2.4, there is a hydraulic jump generated downstream $step_1$ for both Run 1 and Run 2, which occurred due to the sudden change in the flow condition from supercritical flow to subcritical flow. In Run 1, the hydraulic jump is formed at a distance faraway from the over-falling jet. However, in the case of Run 2, it is affected by the backwater and moved to the upstream direction close to the over-falling jet.

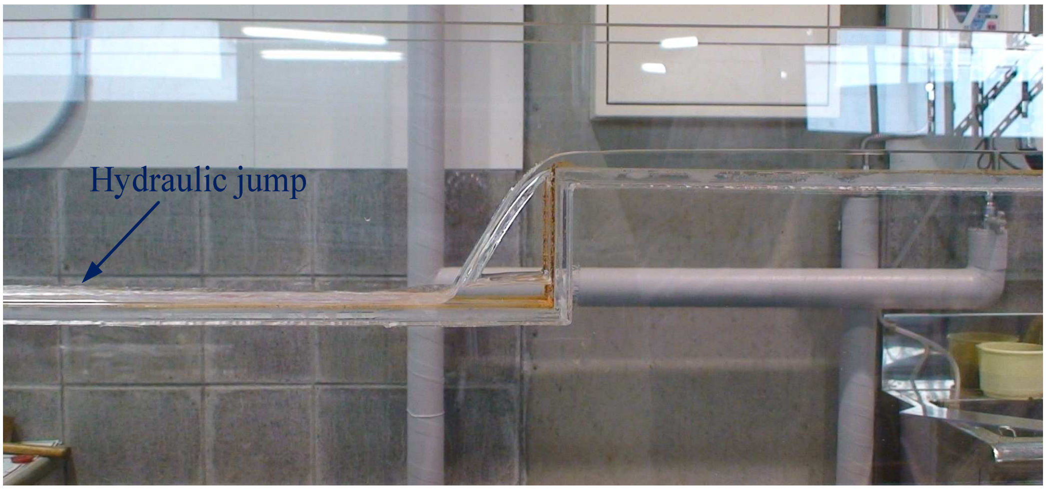

(a) Run 1

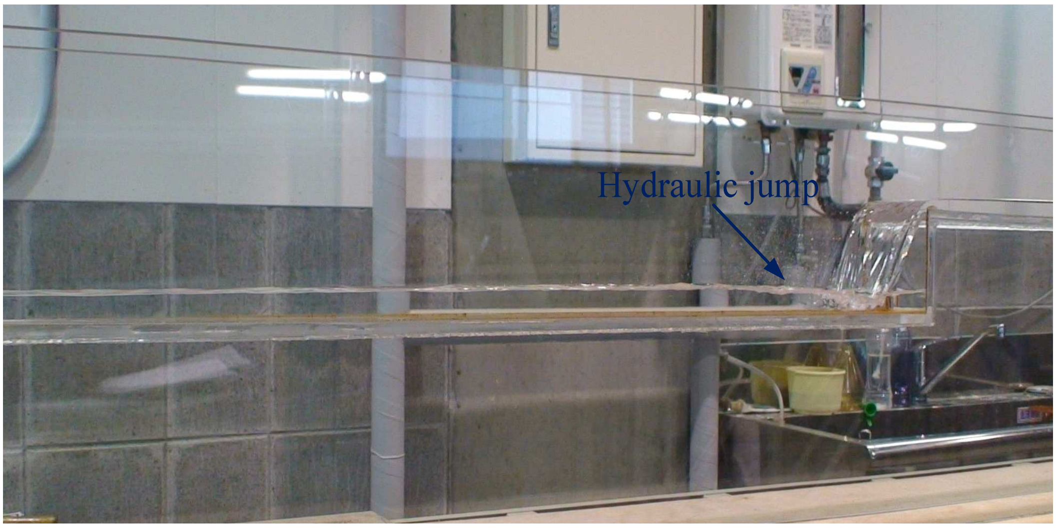

(b) Run 2

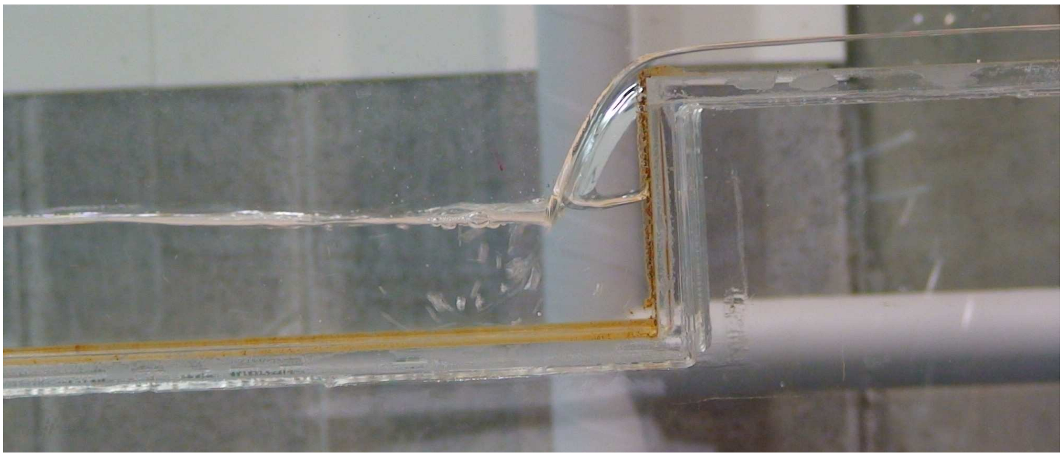

(c) Run 3

Figure 2.3 Laboratory experiment results.

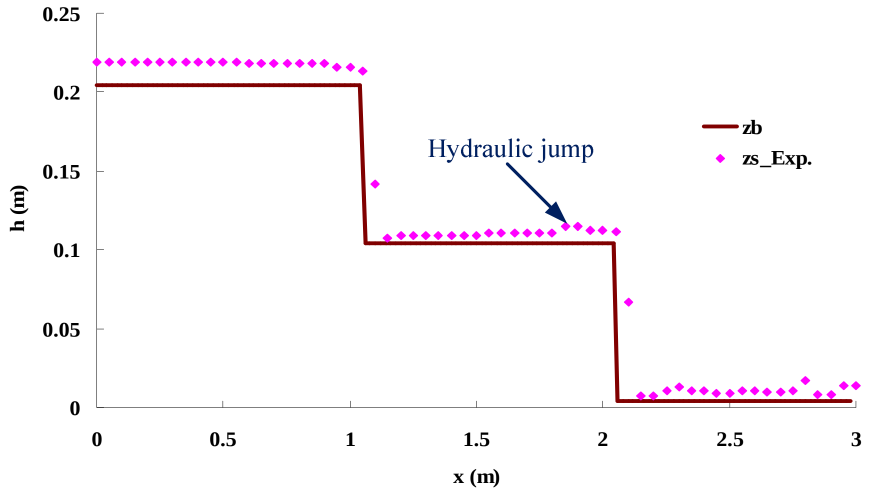

(a) Run 1

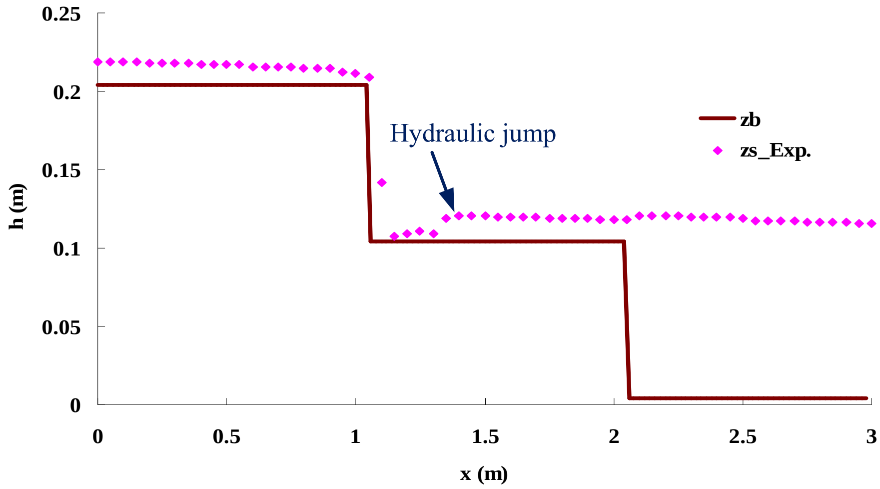

(b) Run 2

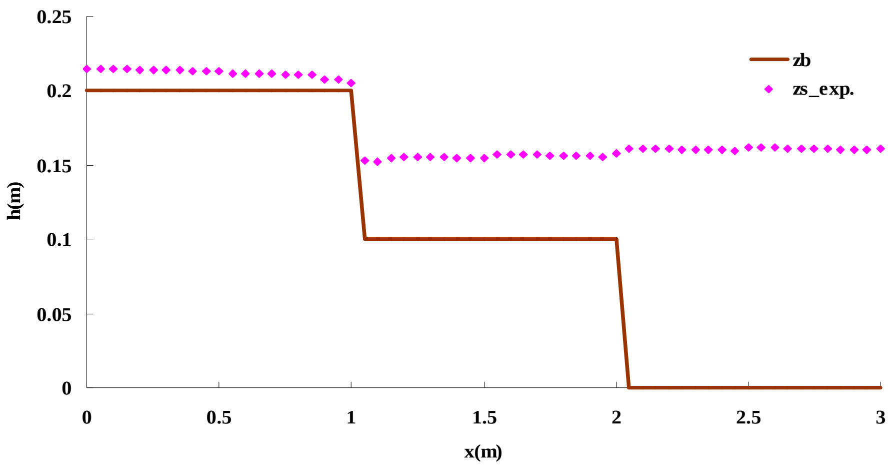

(c) Run 3

Figure 2.4 Surface water variations along centerline.

2.3.2 Flow Characteristics at Drop

Since we are dealing with a transparent glass flume, we found it is a good idea to consider the height of water in the pool behind the over-falling jet "Y_P" in order to analyze some flow characteristics at drop. The depth of the pool behind the over-falling jet can affect on the pressure of the pool, which can have some influence on the location of the hydraulic jump. The experimental value of "Y_P" measured in Run 1 is compared with the values predicted by another five authors. The equations used by these authors are shown as follow:

[Moore (1943): Analytical solution]

$$\frac{Y_P}{Y_c} = \sqrt{\left(\frac{Y_1}{Y_c}\right)^2 + 2\frac{Y_c}{Y_1} - 3} \tag{2.1}$$

[Rand (1955): Model data 0.045< Y_c/H <1]

$$\frac{Y_P}{H} = \left(\frac{Y_c}{H}\right)^{0.66} \tag{2.2}$$

[Gill (1979): Model data 0.075< Y_c/H <0.45]

$$\frac{Y_P}{H} = 1.067\left(\frac{Y_c}{H} - 0.0016\right)^{0.697} \tag{2.3}$$

[Rajaratnam and Chamani (1995): Solution of nonlinear equations]

$$\frac{Y_P}{H} = 1.107\left(\frac{Y_c}{H}\right)^{0.719} \tag{2.4}$$

[Chanson (1995): Analytical solution]

$$\frac{Y_P}{H} = 0.998\left(\frac{Y_c}{H}\right)^{0.675} \tag{2.5}$$

where H is the step height; Y_c is the critical depth and Y_1 is the water depth at the immediate downstream of the free-fall.

The results in Figure (2.5) show that the experimental value of Y_P matches with other measured and calculated values, and it is very close to the analytical value predicted by Moore (1943) and Chanson (1995).

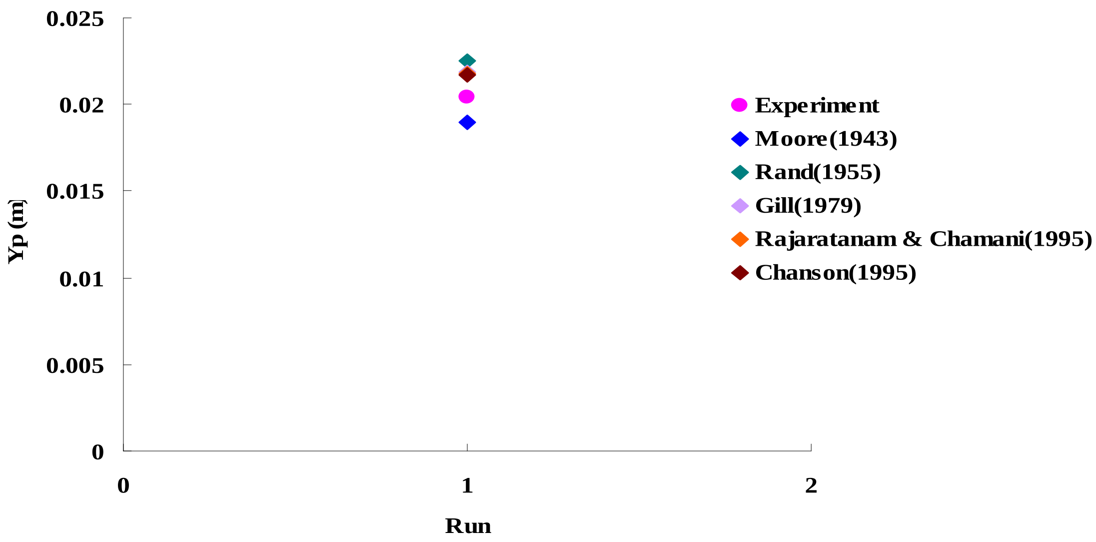

Figure 2.5 Comparison between predicted and experimental values of Y_P.

2.4 Numerical Model

2.4.1 Governing Equations

A one-dimensional numerical model in the Cartesian coordinate system is developed in for simulating unsteady open channel flow in order to represent the formation of the hydraulic jump (Figure 2.6). The model is based on the finite volume method. The governing equations used in the model are as follow:

[Continuity equation]

$$\frac{\partial A}{\partial t}+\frac{\partial Q}{\partial x}=0 \tag{2.6}$$

[Momentum equation]

$$\frac{\partial Q}{\partial t}+\frac{\partial uQ}{\partial x}+gA\frac{\partial z_s}{\partial x}=-gA\frac{\tau_{bx}}{\rho gR}+\frac{\partial -\overline{u'^2 A}}{\partial x} \tag{2.7}$$

where Q: discharge; A: cross sectional area; u: cross sectional average velocity; z_s: water surface elevation from the datum plane; g: gravity acceleration; R: hydraulic radius; τ_{bx}: x-components of bottom shear stress vectors; u': turbulent fluctuations; ρ: density of fluid; t: time; x: spatial coordinate.

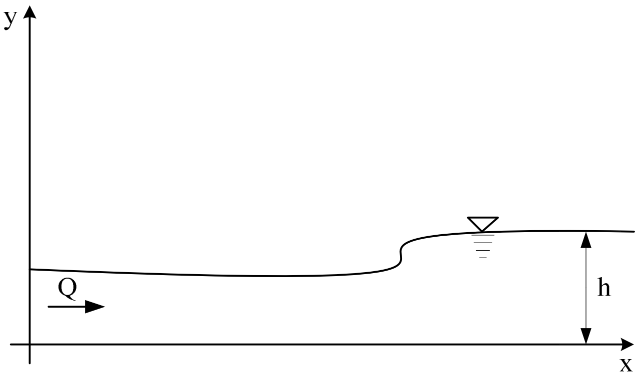

Figure 2.6 Explanation of symbols and coordinate system.

The last term in the right side of the momentum equation is the momentum transport term cause by turbulent velocities and is normally neglected. The bottom shear stress is evaluated by the Manning's formula.

$$\frac{\tau_{bx}}{\rho} = \frac{gn^2 u|u|}{R^{1/3}} \tag{2.8}$$

where n : Manning roughness coefficient.

2.4.2 Discretization of Governing Equations

The governing equations given in section 2.4.1 are discretized by the finite volume method. First upwind scheme is used for time integration. The definition of the location of the hydraulic variables used in the calculation is shown in Figure 2.7, in which velocity and discharge are defined at the cell boundaries and water depth is defined at the middle of the cell. The flow domain is divided into the grid cells by planes parallel to the coordinate axes.

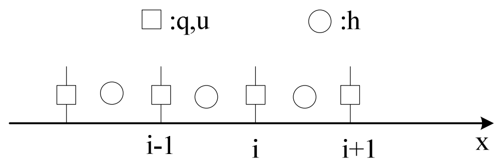

Figure 2.7 Location of hydraulic variables.

The typical discrete form for the continuity and momentum equation which satisfies the flux conservation and based on finite volume method is shown below:

$$\frac{A_{i+1/2}^{n+1} - A_{i+1/2}^{n}}{\Delta t} + \frac{Q_{i+1}^{n} - Q_{i}^{n}}{\Delta x} = 0 \tag{2.9}$$

$$\frac{Q_i^{n+1} - Q_i^n}{\Delta t} + \frac{u_{i+1/2}^n Q_{i+a}^n - u_{i-1/2}^n Q_{i-1+b}^n}{\Delta x} + gA_i^n \frac{z_{si+1/2}^{\,n} - z_{si-1/2}^{\,n}}{\Delta x} = -\left(gA\frac{\tau_{bx}}{\rho g R}\right)_i^n \tag{2.10}$$

$$a = \begin{cases} 0\,;\ u_{i+1/2}^n \geq 0 \\ 1\,;\ u_{i+1/2}^n < 0 \end{cases},\ b = \begin{cases} 0\,;\ u_{i-1/2}^n \geq 0 \\ 1\,;\ u_{i-1/2}^n < 0 \end{cases},\ u_{i+1/2}^n = \frac{u_{i+1}^n + u_i^n}{2},\ u_i^n = \frac{Q_i^n}{A_{i-1/2+c}^n},\ c = \begin{cases} 0\,;\ Q_i^n \geq 0 \\ 1\,;\ Q_i^n < 0 \end{cases}$$

where superscripts n and n+1 denote current and next time step, respectively.
A hydraulic jump can be simulated by solving Eq. (2.9) and (2.10) subjected to the appropriate boundary conditions. We assume the open channel flow in a uniform rectangular section, and discharge is given at the upstream end and water depth is given at the downstream end as boundary conditions. In this regard, the depth at the downstream h_n is given as the same value of depth h_{n-1}. By starting with the specific initial conditions, the solution of these equations is continued until a steady state is reached. When the flow reached to the steady state, water depth instantaneously increases to h_n. Therefore, the jump traveled from the downstream end toward the upstream end and then moved back until it was stabilized in one location.

2.5 Verification of Results

In the experimental investigations, it is almost impossible to precisely measure the water surface profile in the jump due to the high fluctuation. Therefore, comparing the observed shape of the jump with the calculated shape is not so accurate. In addition, uncertainty is introduced in the computed results by the oscillations downstream of the jump. It is known that numerical oscillation occurs around hydraulic bore in spite that the first upwind scheme is applied to the convective inertia term. These oscillations are introduced by the inherent limitations of the numerical schemes and are not a true representation of the physical phenomenon being simulated.

Figure 2.8 shows the variation of water depth at the centerline for both the observed and the calculated results under $\Delta x = 0.005\,m$. In Run 1, the calculated water surface almost fits with the measured one except on the location of the hydraulic jump. The jump obtained by the model is located slightly upstream of the location of the observed jump.

Although, the location of the hydraulic jump downstream $step_1$ in Run 2 is a slightly different than the observed one, the rest of the streamline upstream and downstream the jump has a good fitting with the measured flow patterns. In Run 3, due to the experimental fluctuation in the water surface downstream a partially-submerged step, rather than the numerical oscillation, there is slightly different between the flows patterns between calculated and measured water surface profile at the immediate downstream the step. However, faraway from the step, the matching is reasonably accepted.

One very important parameter in the simulation of a hydraulic jump is the size of the spatial grid, Δx (Gharangik and Chaudhry, 1991). In this study three values of Δx are tested, $0.05m$, $0.01m$ and $0.005m$. Figure 2.9 illustrate the results for simulating the three cases of flow under the three grid sizes. In Run 1, even there is no significant difference between the flow patterns using the three spatial grid sizes, using $\Delta x = 0.01\ m$ and $\Delta x = 0.005\ m$ gave a slightly clear representative of the jump downstream $step_1$.

When the values of $\Delta x = 0.05\ m$ and $\Delta x = 0.01\ m$ are used in simulating Run 2, the water surface is almost same. However, by reducing Δx to $0.005m$, the reproduction of the hydraulic jump is much clear and the location of the jump moved upstream the location of using larger grid sizes. This is because the difference between $\Delta x = 0.005m$ and the other two grid sizes is very big compare to the difference between the other values. Such difference in the spatial grid sizes affected on the location of the critical depth at the vertical drop, which as a result can effect on the location of the hydraulic jump.

Although numerical oscillation occurs during the simulation process of Run 3 for the three grid sizes, the results are improved and the hydraulic jump is obviously illustrative by decreasing the grid size to $\Delta x = 0.01m$ and $\Delta x = 0.005m$. Such oscillation can be smoothed by introducing artificial viscosity and using high order convection schemes.

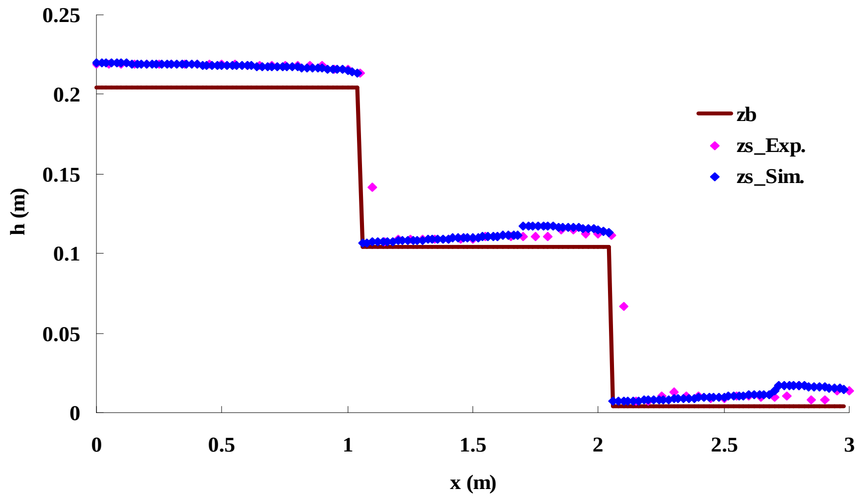

(a) Run 1

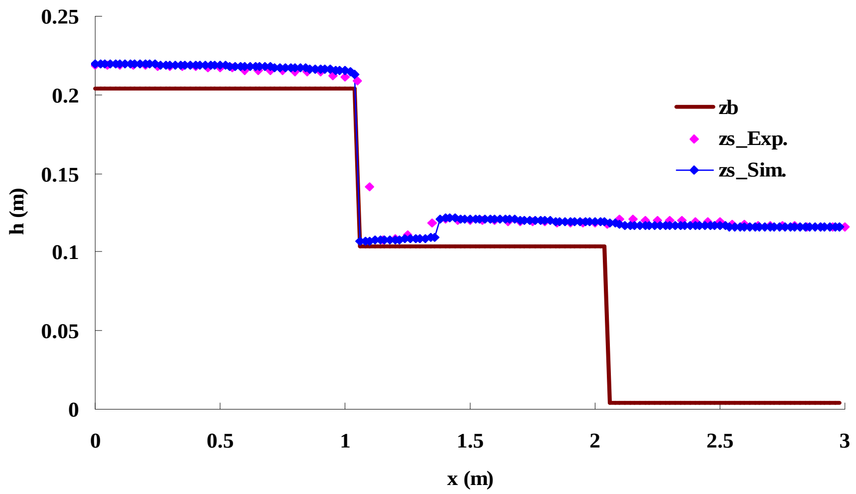

(b) Run 2

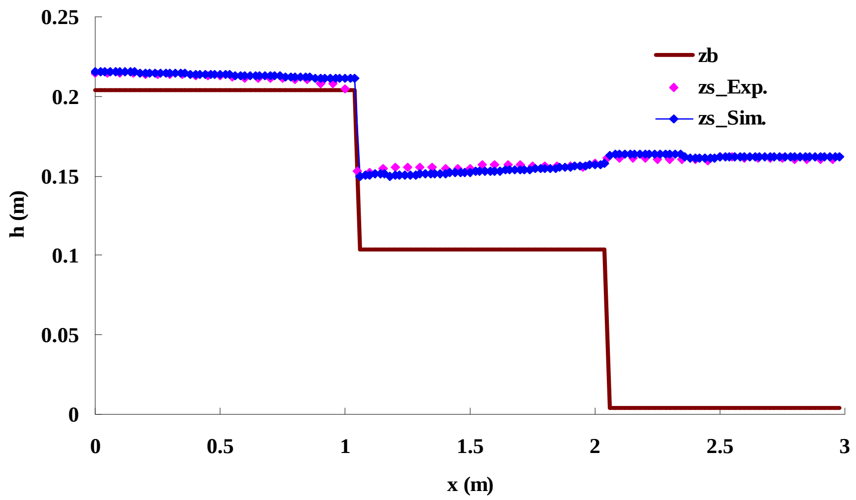

(c) Run 3

Figure 2.8 A verification of water depth at the centerline of both experimental and numerical results, $\Delta x = 0.005$ m.

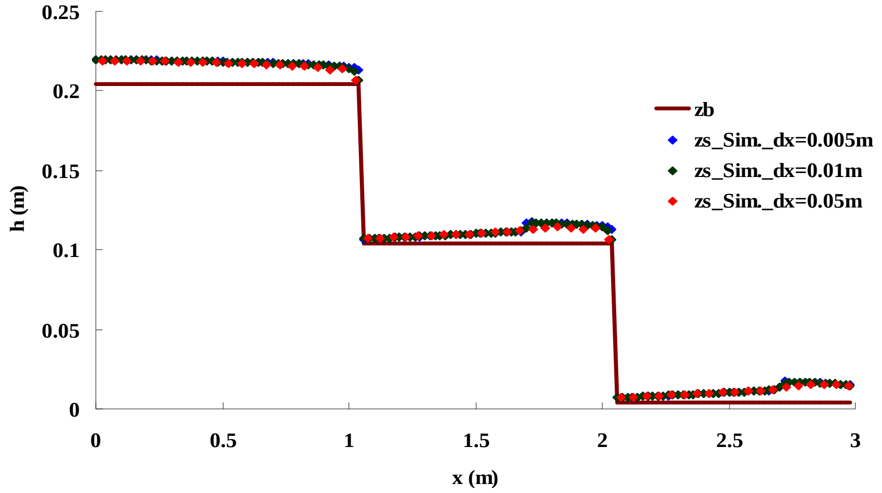

(a) Run 1

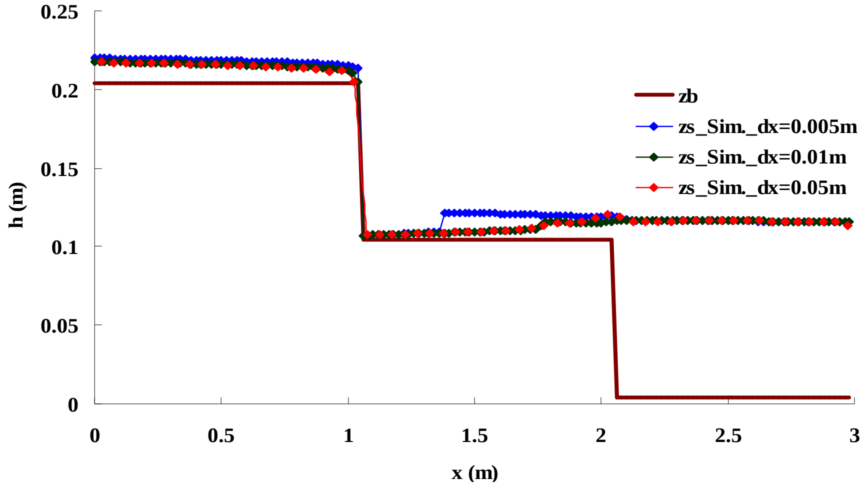

(b) Run 2

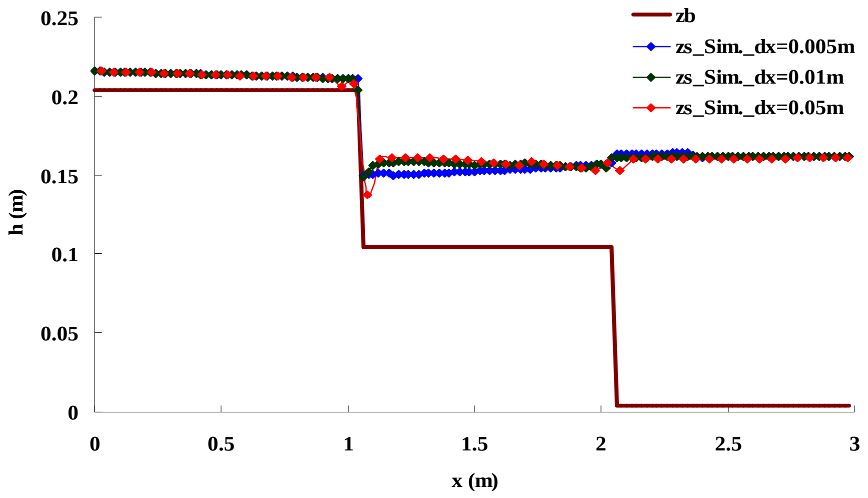

(c) Run 3

Figure 2.9 A verification of water depth at the centerline of numerical results for different grid sizes.

2.6 Summary

In this chapter, a one-dimensional numerical model is applied for a channel which contains two backward-facing steps under the experimental conditions. Three cases are considered with free-fall, partly-submerged and fully-submerged steps. The numerical analysis focused on the flow feature downstream the step especially the formation of the hydraulic jump. Such flow features occurred because of the sudden change in the geometry of the channel due to the existence of the backward-facing step. The model used has ability to reproduce such phenomenon. The effect of the grid size is considered in order to avoid the oscillation at the immediate downstream of the step and to reproduce the hydraulic jump in a proper way. The results were compared to the observed results and they were significantly improved when the grid size is reduced

In general, the experimental flow patterns including the hydraulic jump can be well simulated by using this model. Hydraulic jump can be represented much clear by using smaller grid sizes.

The height of water behind the over-falling jet Y_P is emphasized experimentally. The experimental value of Y_P match properly with values predicted by previous authors and has a very close value to the analytical value predicted by Moore (1943) and Chanson (1995).

Chapter 3

DEPTH-AVERAGED MODELING OF FLOW OVER A BACKWARD-FACING STEP

3.1 Preliminaries

In the previous chapter, a one-dimensional numerical model in Cartesian coordinate system is developed and applied under experimental conditions of flow over multi backward-facing steps. In this chapter, study of flow over backward-facing steps is extended with more emphasis on the flow features such as shockwaves and hydraulic jump downstream the step, which shaped due to the abrupt changes in the flow cross section. A depth-averaged two-dimensional numerical model for unsteady flow in open channel is established using the finite volume method on a curvilinear grid. The two-dimensional basic governing shallow water equations used in the generalized curvilinear coordinate system are solved. The numerical model is applied to experimental conditions for a wooden flume including a single backward-facing step with abrupt expansions at the immediate downstream of the step.

Separated flows produced by an abrupt change in geometry are of great importance in many engineering applications (Barkley et al. 2002). Among the various flow geometries, the two-dimensional backward-facing step has a simple geometry to present flow separation and reattachment phenomena. There are several investigations of flow over a backward-facing step available in the literature. For example, Denham and Patrick (1974) conducted experiments on laminar flow over a backward-facing step. Reattachment lengths and velocity profiles were measured in the study. Armaly et al. (1983) provided data on separation and reattachment points, stream-wise velocity measurements are reported for several Reynolds numbers. Ghia et al. (1989) computed two-dimensional solutions of the backward-facing step flow throughout the laminar regime and found a good agreement with the two-dimensional flows observed by Armaly et al. (1983).

Diffraction of Shockwave behind a backward-facing step is one of the fundamental topics in shockwave dynamics and studied extensively by many researchers (Ohyagi et al. 2002). Carling (1995) reported the direct observation of the development of a hydraulic jump during flood flow. He proved experimentally that the V-shaped wave can be generated by the sudden flow expansions. Ohyagi et al. (2002) studied the phenomenon of shockwaves behind a backward-facing step experimentally in a tube by using high-speed photography as well as pressure measurements on the sidewall of the channel. They studied the relation between the pressure and the location of the wave under different pressure magnitude. Talking about recent studies, Puay and Hosoda (2009) studied theoretically, experimentally and numerically the generation of the shockwaves due to the abrupt expansion of supercritical flow without existing of step.

When the flow is subjected to sudden transition due to sudden change in the geometry of the channel, abrupt expansion flow occurs. Such scenario is clearly observed in the Kamo River. Most of the backward-facing step structures have a sudden expansion as shown in Figure 3.1. This figure shows clearly the formation of the oblique shockwaves from both sides of the channel, and the hydraulic jump at the middle of the channel. In this chapter, abrupt expansion flow which occurs at the immediate downstream of the step is studied by giving focus to the development of the V-shaped oblique shockwaves downstream the step. The two-dimensional unsteady differential equations for conservation of mass and momentum are solved. Results are reported and compared with experiments for which the flow maintained its two-dimensionality in the experiments. Under these circumstances, a good agreement between experimental and numerical results is obtained. These results can represent the flow patterns downstream a backward-facing step in the Kamo River.

Figure 3.1 Abrupt expansion of flow downstream a step in the Kamo River.

The flow characteristics of the water free-fall drop are studied in the previous chapter by considering the water depth of the pool behind the free-fall "Y_P". In this chapter, the features of the flow at drops is continued to be considered by focusing on the depth of the supercritical stream immediately downstream the step "Y_1" as shown in Figure 3.2. The observed and calculated results are compared with values of "Y_1" predicted by previous authors.

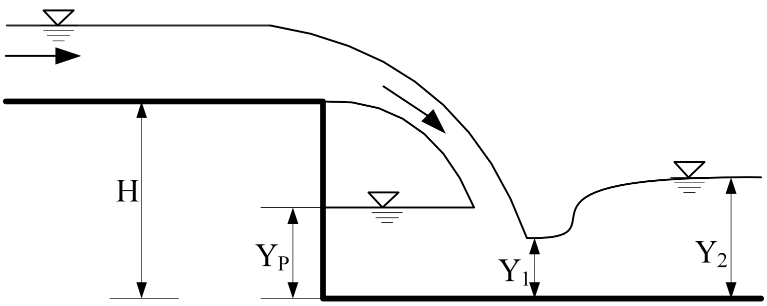

Figure 3.2 Definition sketch for Y_1.

3.2 Laboratory Tests

The laboratory tests were carried out in the River and Urban Hydraulic Laboratory at Kyoto University. A schematic view of the experimental setup is shown in Figure 3.3 and Figure 3.4.

Water levels were measured at different points in the flow domain using point-gauge instrument. The length of the flow domain, $L = 250\,cm$ and the channel width, $B = 91cm$. The grid size used in the flume is $(5cm\,x\,5cm)$. The hydraulic variables for the laboratory test are illustrated in Table 3.1. In these experiments the measurements were conducted for $20\,cm$ and $10\,cm$ step height.

As shown from Table 1, the experiments are carried out to analyze both free-water-fall and flow with submerged step in order to study the backwater effect on the upstream part of the step.

Table 3.1 Hydraulic variables in the experiments.

Run	H (cm)	L (cm)	B (cm)	Q (cm^3/s)	$h_{u/s}$ (cm)	$h_{d/s}$ (cm)	T (℃)	GH (cm)	Remarks
1	20	250	91	9470	2.55	2.67	16.5	0	FWF
2	20	250	91	9470	2.55	3.44	17.0	1.5	FWF
3	10	250	91	11150	3.05	1.88	20.6	0	FWF
4	10	250	91	9150	1.90	10.76	11.9	7	SS
5	10	250	91	9150	3.42	13.58	12	10	SS
6	10	250	91	9150	7.59	17.26	11.9	14	SS

where H = step height; L = length of flow domain; B = channel width upstream the step and after 60 cm faraway from the downstream of the step; Q = discharge; $h_{u/s}$ = upstream water depth; $h_{d/s}$ = downstream water depth; T = water temperature; GH = gate height located at the downstream end; FWF = free-water-fall; SS = submerged-step.

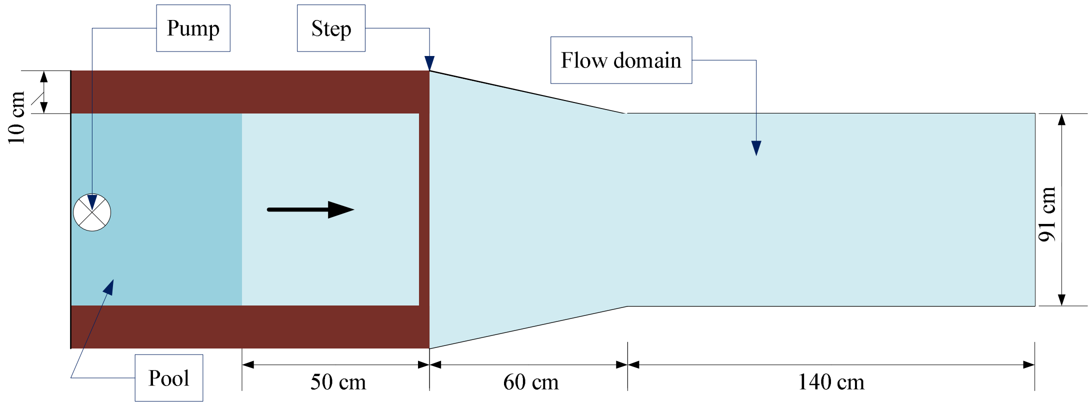

Figure 3.3 Schematic view of the experimental installation.

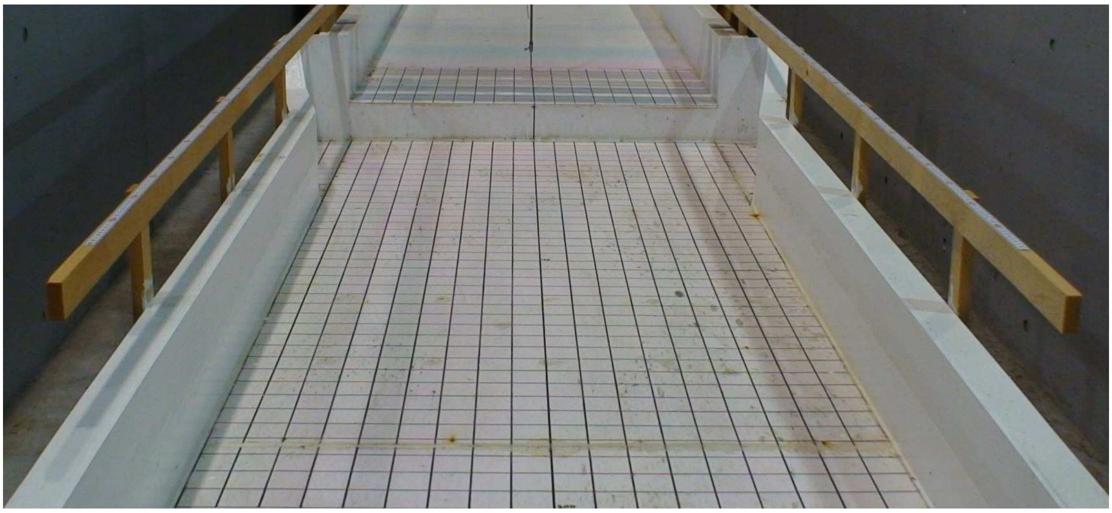

Figure 3.4 Laboratory experiment setup.

3.3 Experiment Results

The laboratory experimental results for free-water-fall condition and submerge-step condition are shown in Figure 3.5, while the surface-contours are plotted in Figure 3.6. From these two figures, the abrupt expansion of flow downstream the step is shown clearly with the formation of the shockwaves. The hydraulic jump is developed immediately after the meeting point of the shockwaves. Figure 3.7 presents the water depth variation along the centerline, where the hydraulic jump is clearly represented in the cases of free-fall conditions.

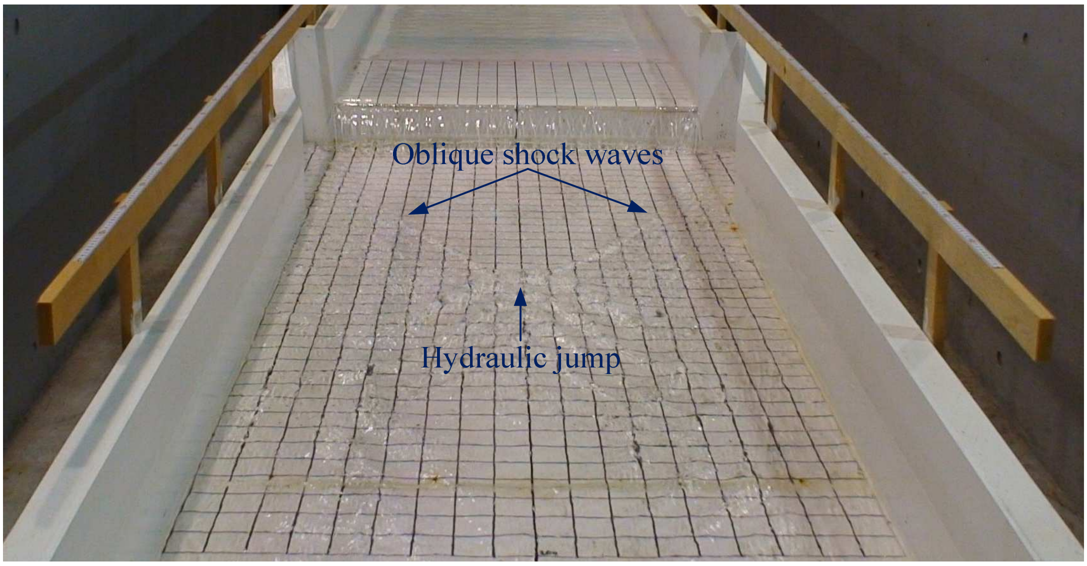

(a) Water-free-fall condition (Run 1).

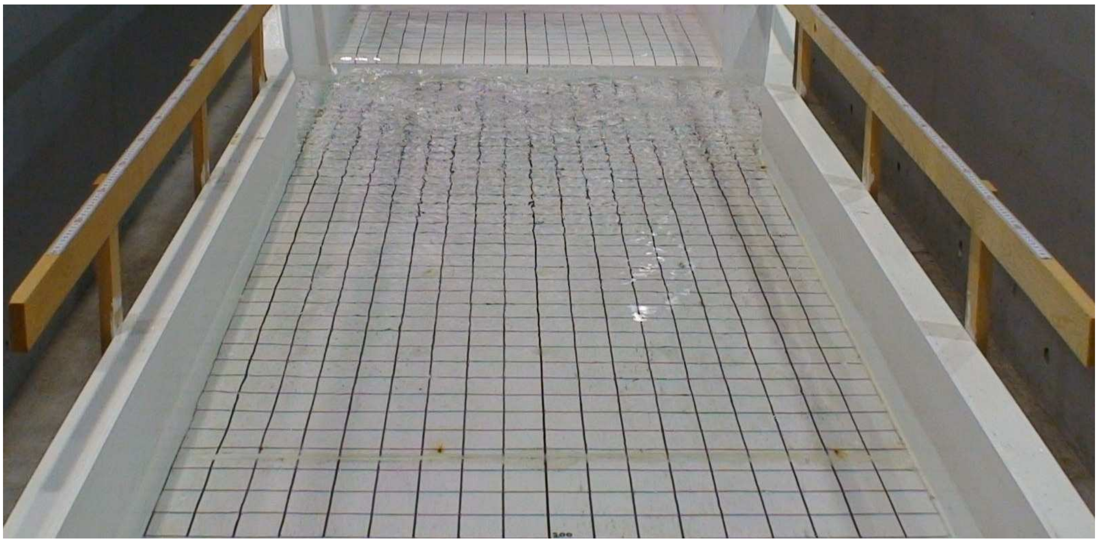

(b) Submerged step condition (Run 4).

Figure 3.5 Laboratory experiment results.

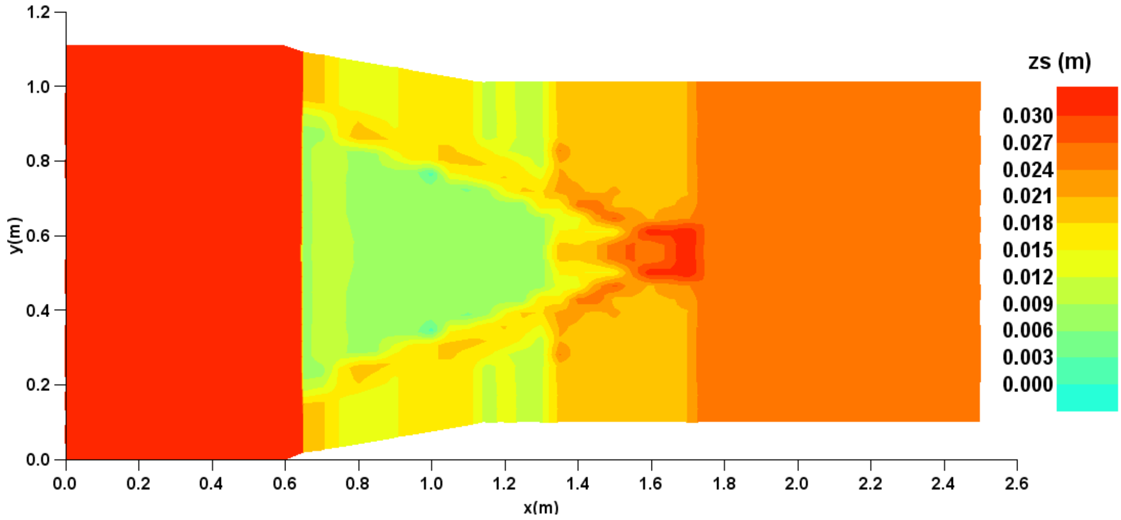

(a) Run 1

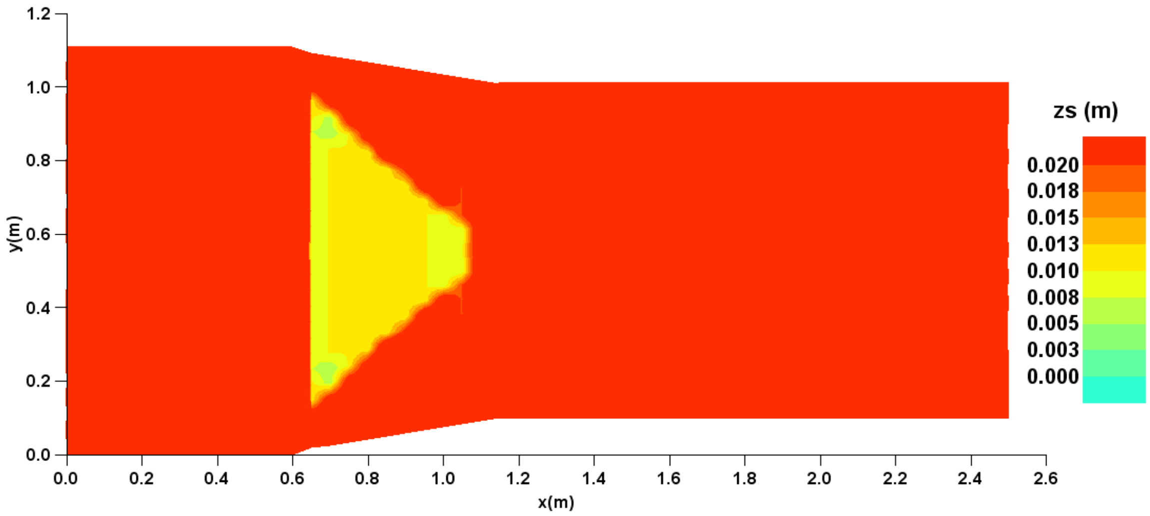

(b) Run 2

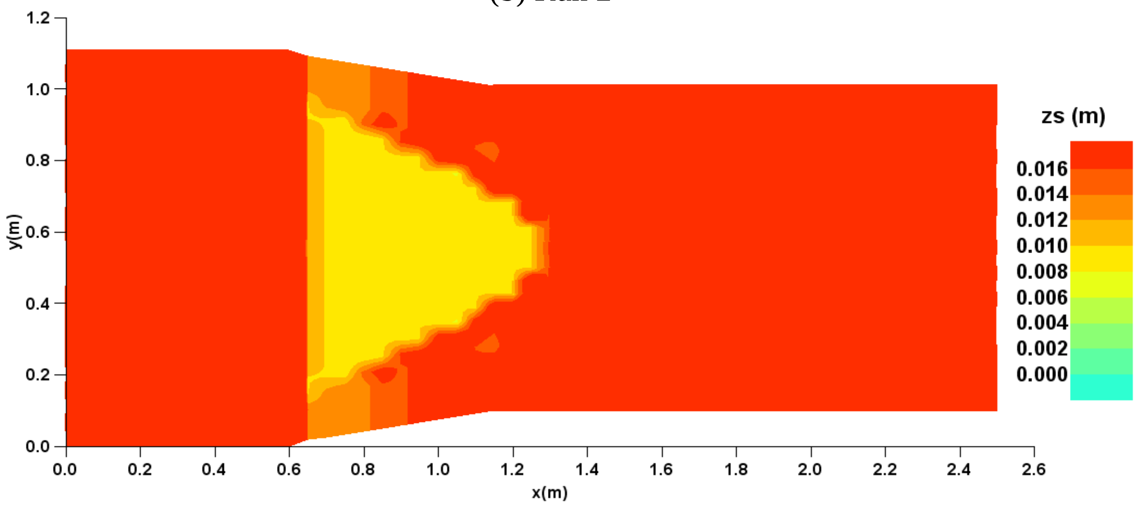

(c) Run 3

Figure 3.6 Surface contours of laboratory experiments results.

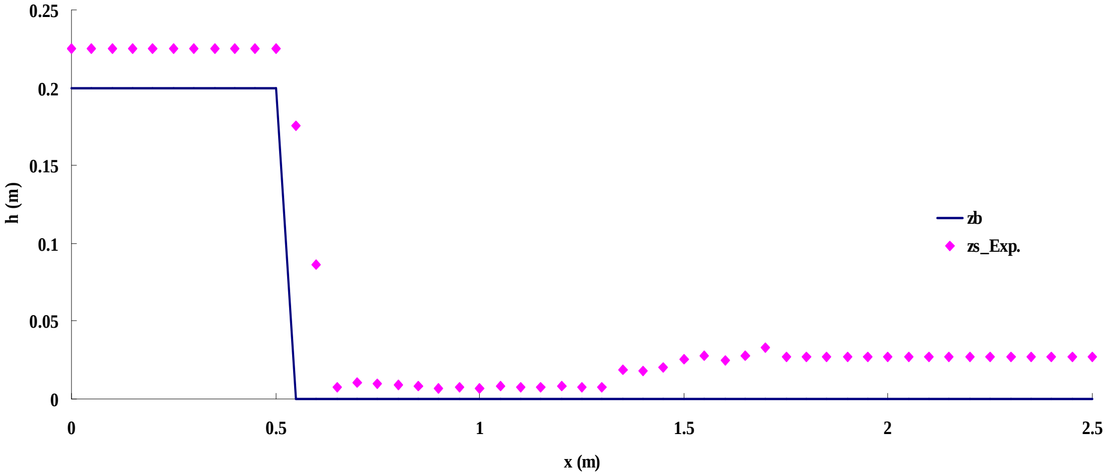

(a) Run 1

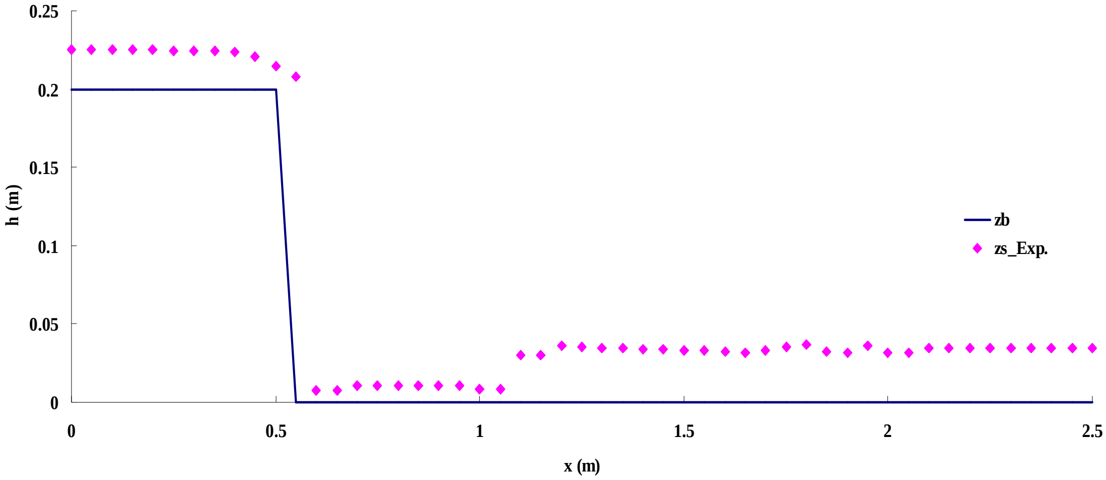

(b) Run 2

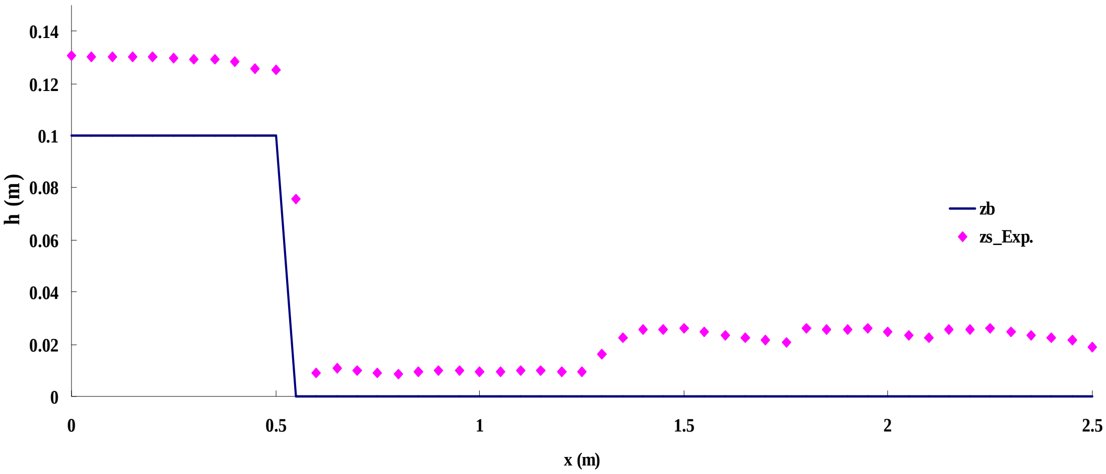

(c) Run 3

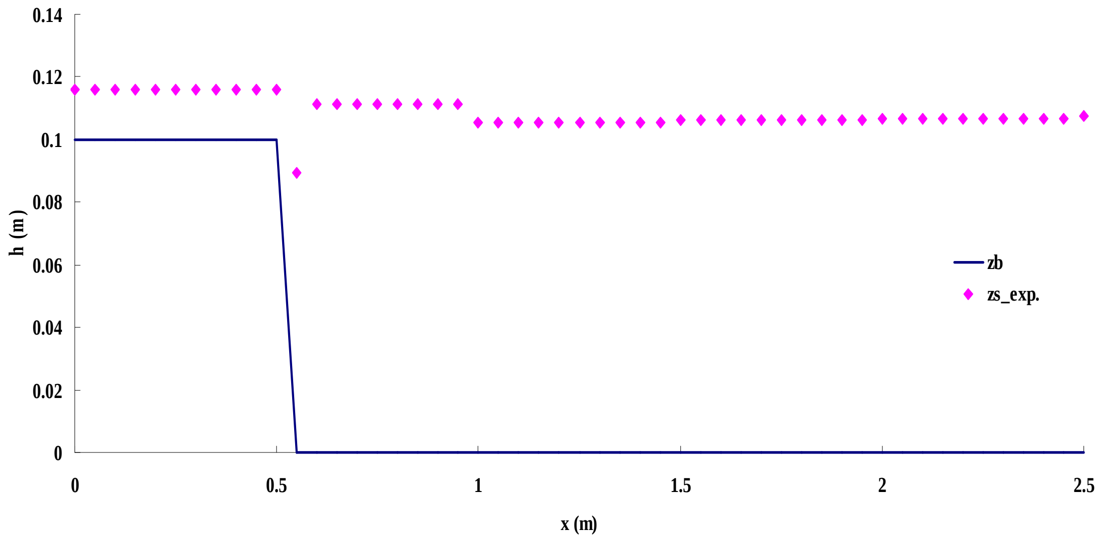

(d) Run 4

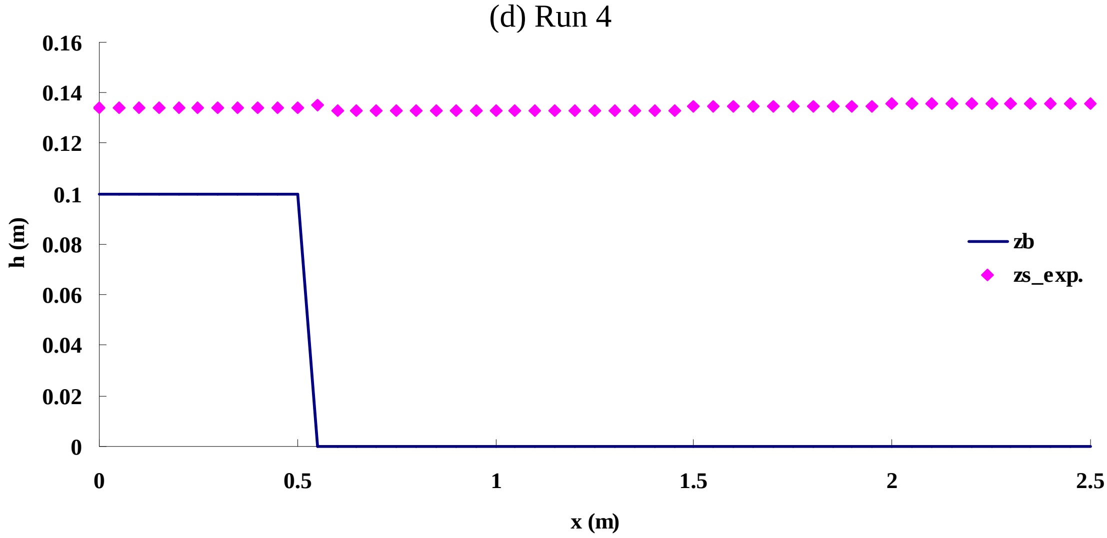

(e) Run 5

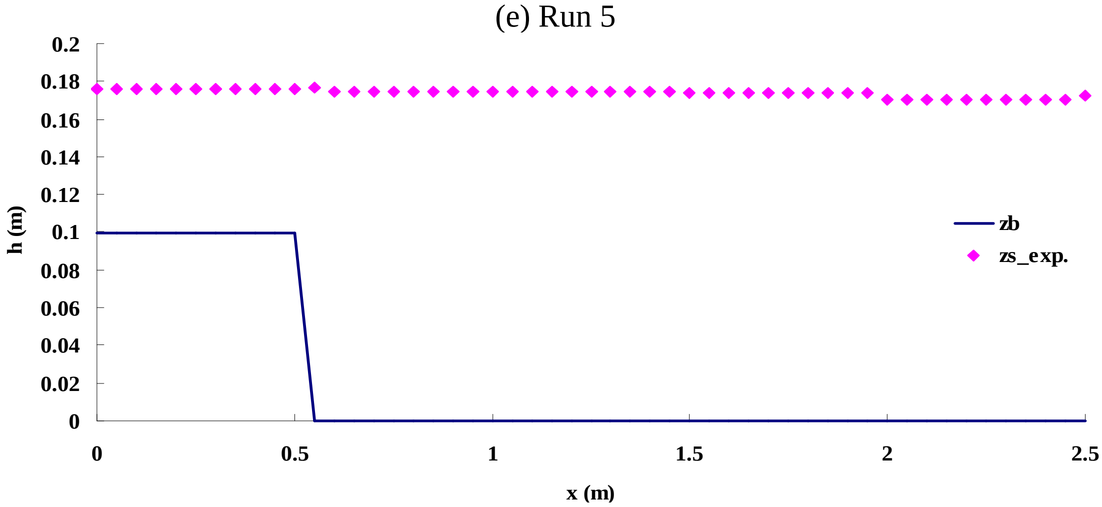

(f) Run 6

Figure 3.7 Surface water variations along centerline.

3.4 Numerical Model

Depth-averaged equations are used for the description of flow. Referring to the coordinate system shown in Figure 3.8, depth-averaged continuity and momentum equations in the Cartesian coordinate are described as follow:

[Continuity Equation]

$$\frac{\partial h}{\partial t}+\frac{\partial M}{\partial x}+\frac{\partial N}{\partial y}=0 \tag{3.1}$$

[Momentum Equations]

(In the x-direction)

$$\frac{\partial M}{\partial t}+\frac{\partial uM}{\partial x}+\frac{\partial vM}{\partial y}=-gh\frac{\partial z_s}{\partial x}-\frac{\tau_{bx}}{\rho}+\frac{\partial}{\partial x}\left(-\overline{u'^2}h\right)+\frac{\partial}{\partial y}\left(-\overline{u'v'}h\right) \tag{3.2}$$

(In the y-direction)

$$\frac{\partial N}{\partial t}+\frac{\partial uN}{\partial x}+\frac{\partial vN}{\partial y}=-gh\frac{\partial z_s}{\partial y}-\frac{\tau_{by}}{\rho}+\frac{\partial}{\partial x}\left(-\overline{u'v'}h\right)+\frac{\partial}{\partial y}\left(-\overline{v'^2}h\right) \tag{3.3}$$

where t: time; (x, y): Cartesian coordinates; (u, v): x, y components of depth-averaged velocity vectors; (M, N): x, y components of discharge flux vectors ($M \equiv uh, N \equiv vh$); g: gravity acceleration; h: depth; ρ: density of fluids; z_s: water surface elevation from the datum plane; (τ_{bx}, τ_{by}): x, y components of bottom shear stress vectors; $-\overline{u'^2}$, $-\overline{u'v'}$, $-\overline{v'^2}$: components of depth-averaged Reynolds stress tensors.

The depth-averaged Reynolds stress tensors can be evaluated by the empirical formulas.

$$-\overline{u'^2}=2D_h\left(\frac{\partial u}{\partial x}\right)-\frac{2}{3}k \tag{3.4}$$

$$-\overline{u'v'}=D_h\left(\frac{\partial u}{\partial y}+\frac{\partial v}{\partial x}\right) \tag{3.5}$$

$$-\overline{v'^2}=2D_h\left(\frac{\partial v}{\partial y}\right)-\frac{2}{3}k \tag{3.6}$$

$$D_h = \alpha h u_*^{\ 2}\text{, } (\alpha : \text{constant}) \tag{3.7}$$

where D_h : eddy viscosity; k : depth-average turbulent kinetic energy; u_* : friction velocity; ($u_* = \sqrt{\frac{\tau}{\rho}}$; τ : the magnitude of the bottom shear stresses).

The depth-averaged turbulent kinetic energy k is also evaluated by the following empirical formula.

$$k = 2.07 u_*^{\ 2} \tag{3.8}$$

The bottom shear stresses are evaluated by the Manning's formula.

$$\tau_{bx} = \frac{\rho g n^2 u \sqrt{u^2 + v^2}}{h^{1/3}}\text{, } \tau_{by} = \frac{\rho g n^2 v \sqrt{u^2 + v^2}}{h^{1/3}} \tag{3.9}$$

where n : Manning's roughness coefficient.

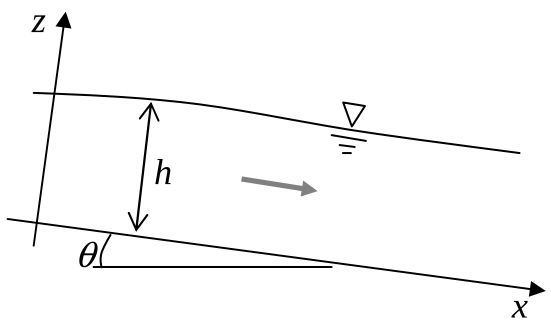

Figure 3.8 Coordinate system for depth-averaged flow.

Eqs. (3.1)-(3.3) are transformed in a generalized curvilinear coordinate (ξ, η) using the following formulas:

$$\frac{\partial}{\partial x} = \frac{\partial \xi}{\partial x}\frac{\partial}{\partial \xi} + \frac{\partial \eta}{\partial x}\frac{\partial}{\partial \eta}\text{, } \frac{\partial}{\partial y} = \frac{\partial \xi}{\partial y}\frac{\partial}{\partial \xi} + \frac{\partial \eta}{\partial y}\frac{\partial}{\partial \eta}$$

[Continuity Equation]

$$\frac{\partial}{\partial t}\left(\frac{h}{J}\right)+\frac{\partial}{\partial \xi}\left(\frac{Uh}{J}\right)+\frac{\partial}{\partial \eta}\left(\frac{Vh}{J}\right)=0 \tag{3.10}$$

[Momentum Equations]

$$\begin{aligned}\frac{\partial}{\partial t}\left(\frac{M}{J}\right)+\frac{\partial}{\partial \xi}\left(\frac{UM}{J}\right)+\frac{\partial}{\partial \eta}\left(\frac{VM}{J}\right)=-gh\left(\frac{\xi_x}{J}\frac{\partial z_s}{\partial \xi}+\frac{\eta_x}{J}\frac{\partial z_s}{\partial \eta}\right)-\frac{\tau_{bx}}{\rho J}\\ +\frac{\xi_x}{J}\frac{\partial}{\partial \xi}\left(-\overline{u'^2}h\right)+\frac{\xi_y}{J}\frac{\partial}{\partial \xi}\left(-\overline{u'v'}h\right)+\frac{\eta_x}{J}\frac{\partial}{\partial \eta}\left(-\overline{u'^2}h\right)+\frac{\eta_y}{J}\frac{\partial}{\partial \eta}\left(-\overline{u'v'}h\right)\end{aligned} \tag{3.11}$$

$$\begin{aligned}\frac{\partial}{\partial t}\left(\frac{N}{J}\right)+\frac{\partial}{\partial \xi}\left(\frac{UN}{J}\right)+\frac{\partial}{\partial \eta}\left(\frac{VN}{J}\right)=-gh\left(\frac{\xi_y}{J}\frac{\partial z_s}{\partial \xi}+\frac{\eta_y}{J}\frac{\partial z_s}{\partial \eta}\right)-\frac{\tau_{by}}{\rho J}\\ +\frac{\xi_x}{J}\frac{\partial}{\partial \xi}\left(-\overline{u'v'}h\right)+\frac{\xi_y}{J}\frac{\partial}{\partial \xi}\left(-\overline{v'^2}h\right)+\frac{\eta_x}{J}\frac{\partial}{\partial \eta}\left(-\overline{u'v'}h\right)+\frac{\eta_y}{J}\frac{\partial}{\partial \eta}\left(-\overline{v'^2}h\right)\end{aligned} \tag{3.12}$$

where (ξ_x , η_x , ξ_y , η_y): metrics coordinate transformation; J , Jacobian; (U , V): contravariant components of velocity vectors.

$$J=\frac{1}{x_\xi y_\eta - x_\eta y_\xi} \tag{3.13}$$

$$U=\xi_x u+\xi_y v,\ V=\eta_x u+\eta_y v \tag{3.14}$$

where (ξ_x , η_x , ξ_y , η_y) are related to (x_ξ , x_η , y_ξ , y_η) by eq.(3.15).

$$\xi_x = Jy_\eta\ ,\ \xi_y=-Jx_\eta\ ,\ \eta_x=-Jy_\xi\ ,\ ,\ \eta_y=Jx_\xi \tag{3.15}$$

The following formula is also used to derive Eqs.(3.10)-(3.12).

$$\frac{1}{J}\frac{\partial \phi}{\partial x}=\frac{1}{J}\left(\frac{\partial \phi}{\partial \xi}\xi_x+\frac{\partial \phi}{\partial \eta}\eta_x\right)=\frac{\partial}{\partial \xi}\left(\frac{\xi_x}{J}\phi\right)+\frac{\partial}{\partial \eta}\left(\frac{\eta_x}{J}\phi\right) \tag{3.16}$$

In order to make the basic equations for computation compatible with finite volume method or central volume method, Eq. (3.11) and Eq. (3.12) are transformed into the equations in which the contravariant components of velocity vectors are used as unknown variables by multiplying the two equations on ξ_x and η_x respectively. The momentum equations can be written as:

(In the ξ-direction)

$$\frac{\partial}{\partial t}\left(\frac{Q^{\xi}}{J}\right)+\frac{\partial}{\partial \xi}\left(\frac{UQ^{\xi}}{J}\right)+\frac{\partial}{\partial \eta}\left(\frac{VQ^{\xi}}{J}\right)$$
$$-\frac{M}{J}\left(U\frac{\partial \xi_x}{\partial \xi}+V\frac{\partial \xi_x}{\partial \eta}\right)-\frac{N}{J}\left(U\frac{\partial \xi_y}{\partial \xi}+V\frac{\partial \xi_y}{\partial \eta}\right)$$
$$=-gh\left(\frac{\xi_x^2+\xi_y^2}{J}\frac{\partial z_s}{\partial \xi}+\frac{\xi_x\eta_x+\xi_y\eta_y}{J}\frac{\partial z_s}{\partial \eta}\right)-\frac{\tau_b^{\xi}}{\rho J} \tag{3.17}$$
$$+\frac{\xi_x^2}{J}\frac{\partial}{\partial \xi}\left(-\overline{u'^2}h\right)+\frac{\xi_x\eta_x}{J}\frac{\partial}{\partial \eta}\left(-\overline{u'^2}h\right)+\frac{\xi_y^2}{J}\frac{\partial}{\partial \xi}\left(-\overline{v'^2}h\right)$$
$$+\frac{\eta_y}{J}\frac{\partial}{\partial \eta}\left(-\overline{v'^2}h\right)+\frac{\xi_x\eta_y+\xi_y\eta_x}{J}\frac{\partial}{\partial \eta}\left(-\overline{u'v'}h\right)+\frac{2\xi_x\xi_y}{J}\frac{\partial}{\partial \xi}\left(-\overline{u'v'}h\right)$$

(In the η-direction)

$$\frac{\partial}{\partial t}\left(\frac{Q^{\eta}}{J}\right)+\frac{\partial}{\partial \xi}\left(\frac{UQ^{\eta}}{J}\right)+\frac{\partial}{\partial \eta}\left(\frac{VQ^{\eta}}{J}\right)$$
$$-\frac{M}{J}\left(U\frac{\partial \eta_x}{\partial \xi}+V\frac{\partial \eta_x}{\partial \eta}\right)-\frac{N}{J}\left(U\frac{\partial \eta_y}{\partial \xi}+V\frac{\partial \eta_y}{\partial \eta}\right)$$
$$=-gh\left(\frac{\xi_x\eta_x+\xi_y\eta_y}{J}\frac{\partial z_s}{\partial \xi}+\frac{\eta_x^2+\eta_y^2}{J}\frac{\partial z_s}{\partial \eta}\right)-\frac{\tau_b^{\eta}}{\rho J} \tag{3.18}$$
$$+\frac{\xi_x\eta_x}{J}\frac{\partial}{\partial \xi}\left(-\overline{u'^2}h\right)+\frac{\eta_x^2}{J}\frac{\partial}{\partial \eta}\left(-\overline{u'^2}h\right)+\frac{\xi_y\eta_y}{J}\frac{\partial}{\partial \xi}\left(-\overline{v'^2}h\right)$$
$$+\frac{\eta_y^2}{J}\frac{\partial}{\partial \eta}\left(-\overline{v'^2}h\right)+\frac{\xi_x\eta_y+\xi_y\eta_x}{J}\frac{\partial}{\partial \xi}\left(-\overline{u'v'}h\right)+\frac{2\eta_x\eta_y}{J}\frac{\partial}{\partial \eta}\left(-\overline{u'v'}h\right)$$

where (Q^{ξ}, Q^{η}): contravariant components of discharge flux vectors, (τ_b^{ξ}, τ_b^{η}): contravariant components of bottom shear stress vectors.

$$Q^{\xi}=\xi_x M+\xi_y N,\quad Q^{\eta}=\eta_x M+\eta_y N \tag{3.19}$$

$$\tau_b^{\xi}=\xi_x\tau_{bx}+\xi_y\tau_{by},\quad \tau_b^{\eta}=\eta_x\tau_{bx}+\eta_y\tau_{by} \tag{3.20}$$

Eq. (3.10), Eq. (3.17) and Eq. (3.18) are the depth-averaged continuity and momentum equations in a generalized coordinate (ξ, η) were used as governing equations.

The basic equations are discretized into finite difference forms, using finite volume method. For the time integration of the equations, the Adams-Bashforth method with second-order accuracy is employed. For all the cases that are simulated using this model, $2.5cm$ mesh size is used in both ξ- direction and η- direction. The definition for the locations of the hydraulic variables used in the calculation is shown in Figure 3.9.

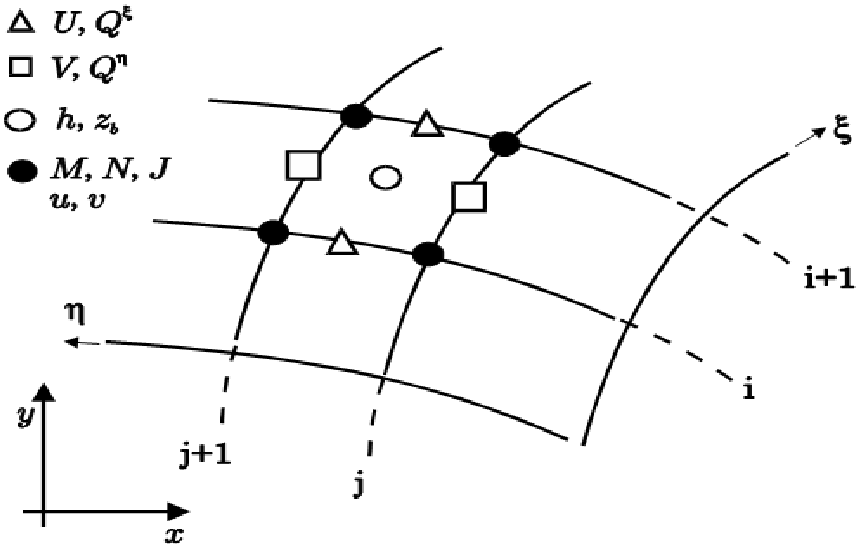

Figure 3.9 Defined locations of variables.

3.5 Verification of Results

3.5.1 Surface Water Variation

The numerical simulation results are plotted in the form of surface contour as shown in Figure 3.10. When the flow passes through the backward-facing step and due to the sudden expansion in the channel downstream the step, the flow direction is subjected to change. The direction of the flow represented clearly by the velocity vectors and the magnitude of the velocity. Figure 3.11 shows the variation of water depth along the centerline for both the observed and the calculated results. For the cases of water-free-fall, the numerical model is capable to reproduce the magnitude and the location of the hydraulic jump downstream the step as shown in Figure 3.11(a, b and c). The shockwaves observed in the experiments are characterized numerically for Run 1, 2 and 3. The results are compared closely with video records taken during the experiments.

In Run 4, high experimental fluctuation occurs which caused unstable water surface downstream the step. Since that the point-gauge instrument is used in the measurement of the water depth, the uncertainty is introduced in the experimental investigation with high experimental error. In addition to the numerical oscillation which occurred during the simulation processes. Therefore, this is believed that the comparison between the observed flow patterns and the calculated results has low accuracy. However, faraway from the step, the numerical water surface elevation can be verified with the measured one with a reasonable accepted matching.

For the fully-submerged step conditions (Run 5 and Run 6), the numerical results have a good agreement with the experimental results.

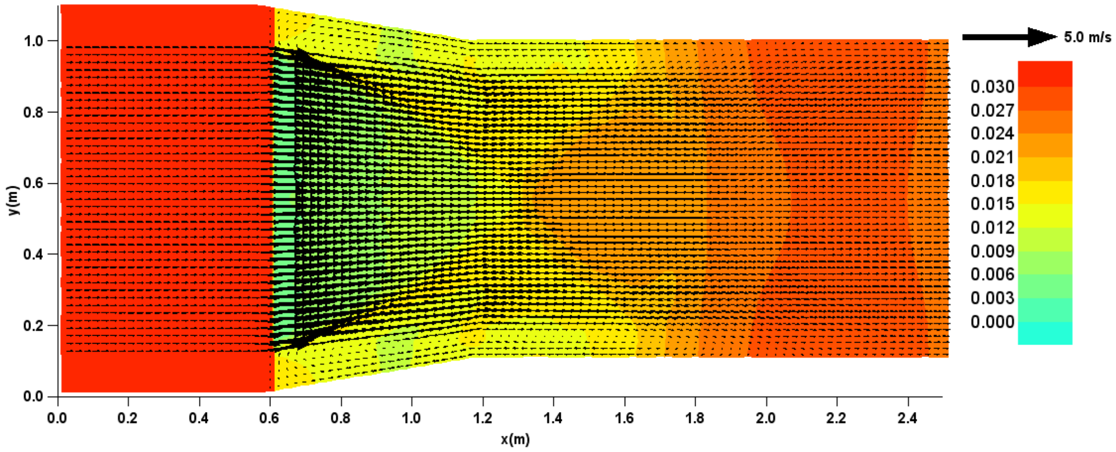

(a) Run 1

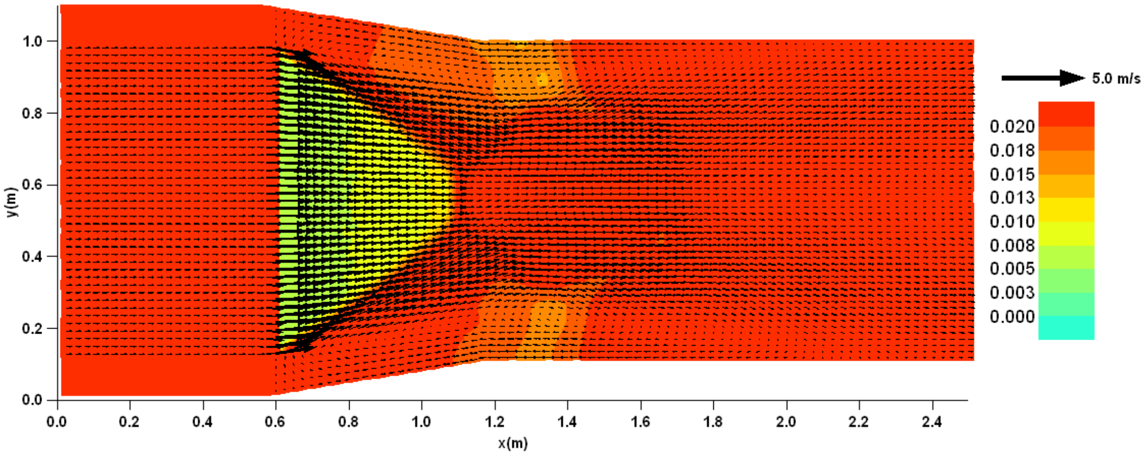

(b) Run 2

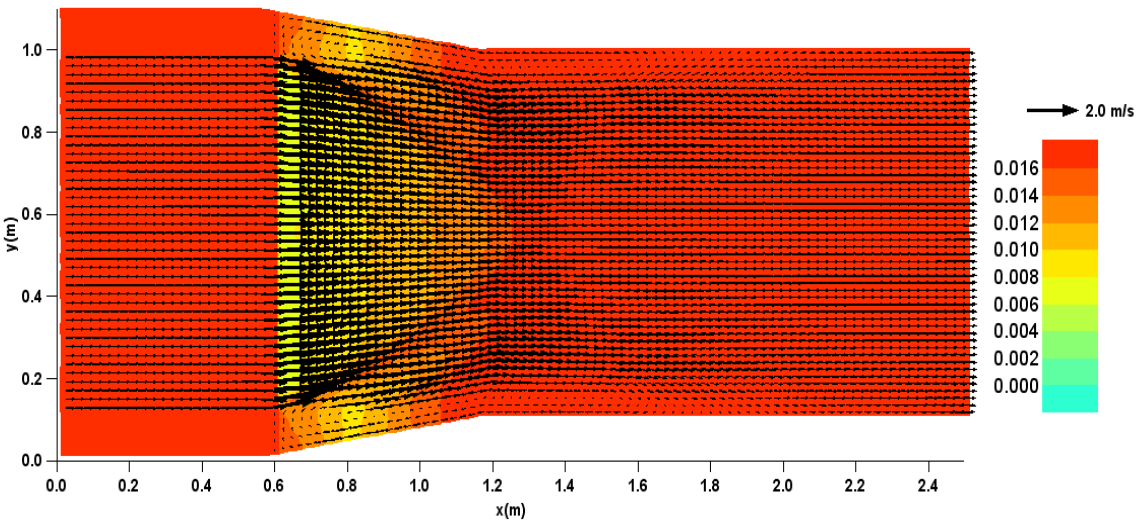

(c) Run 3

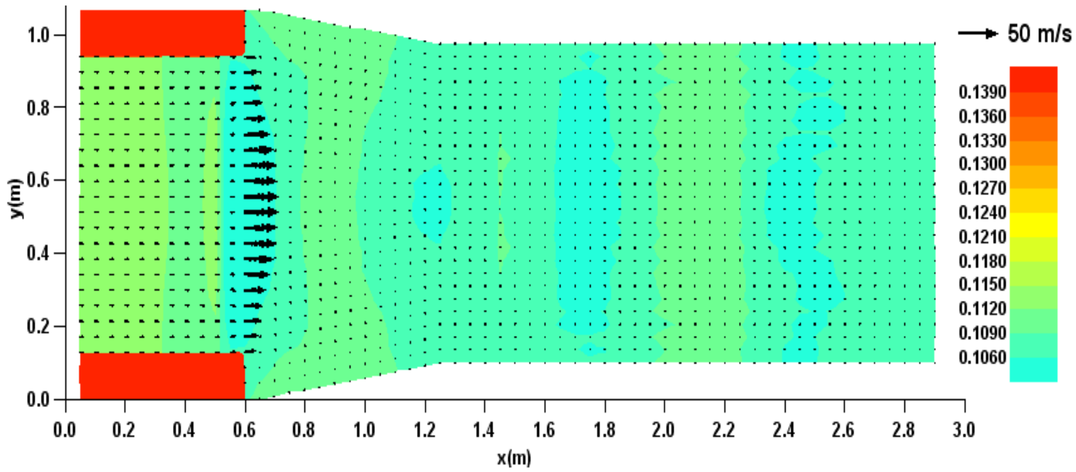

(d) Run 4

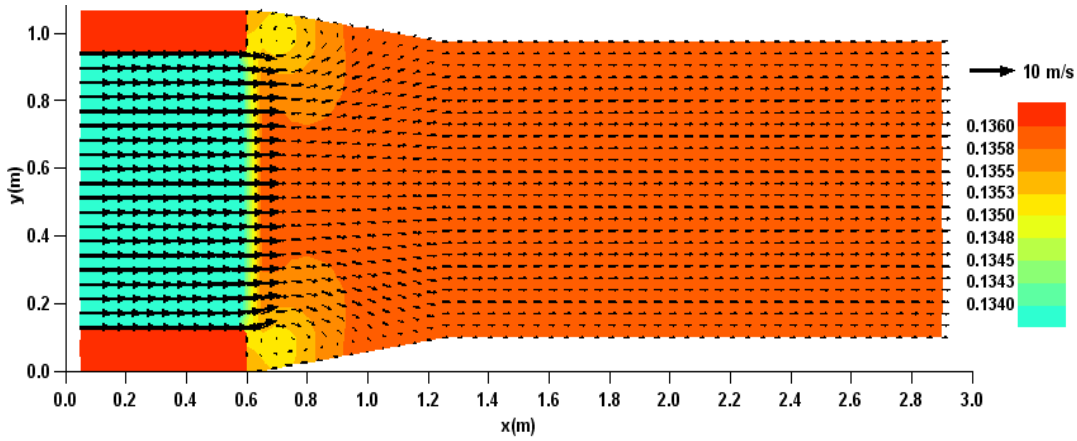

(e) Run 5

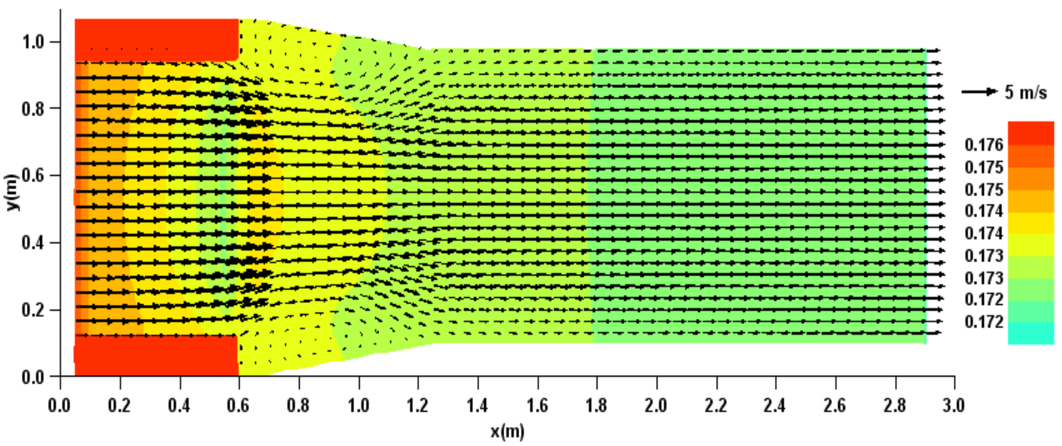

(f) Run 6

Figure 3.10 Surface contours of numerical results.

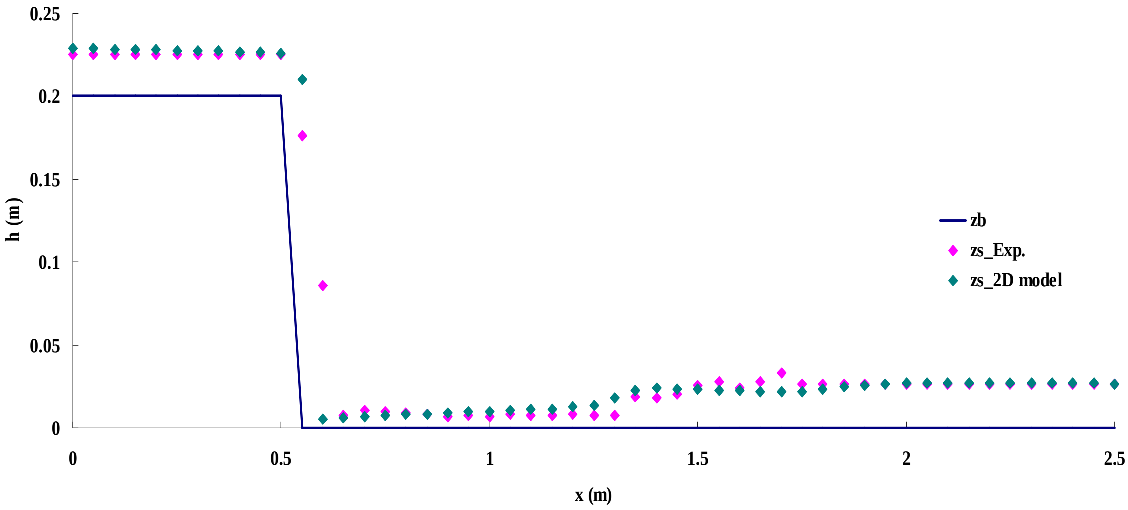

(a) Run 1

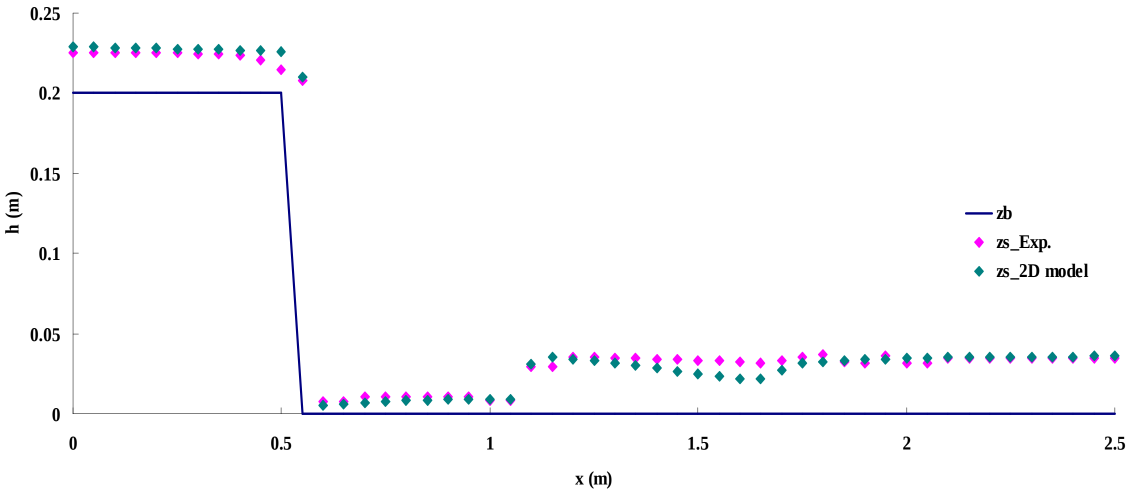

(b) Run 2

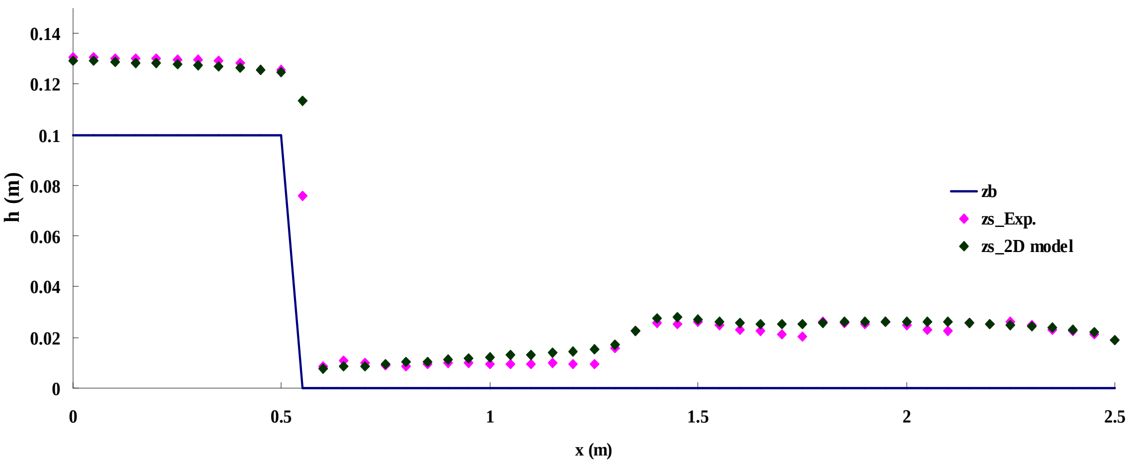

(c) Run 3

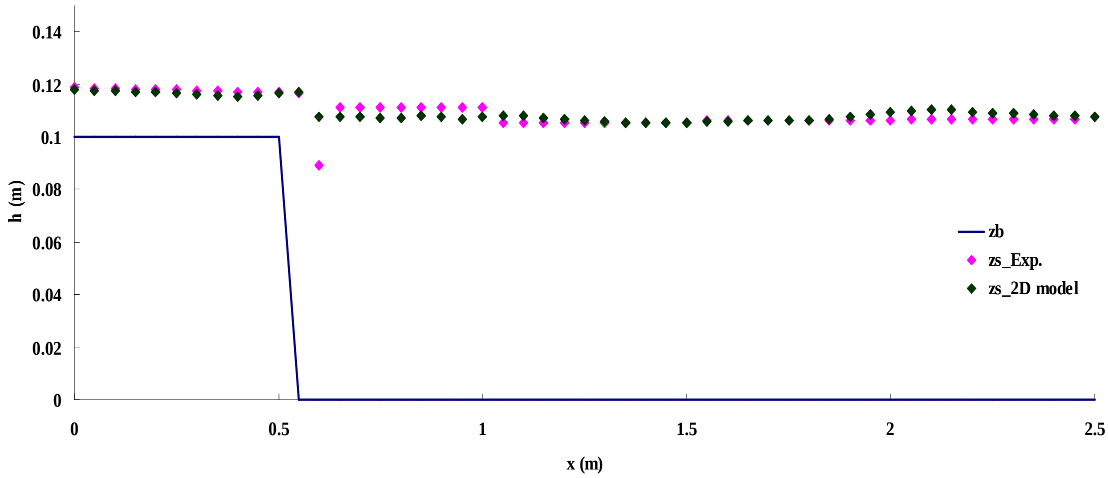

(d) Run 4

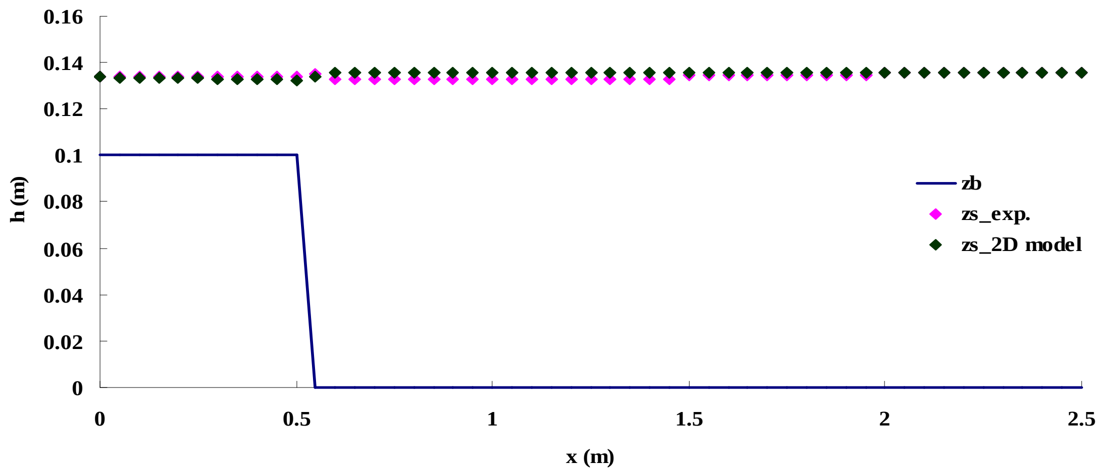

(e) Run 5

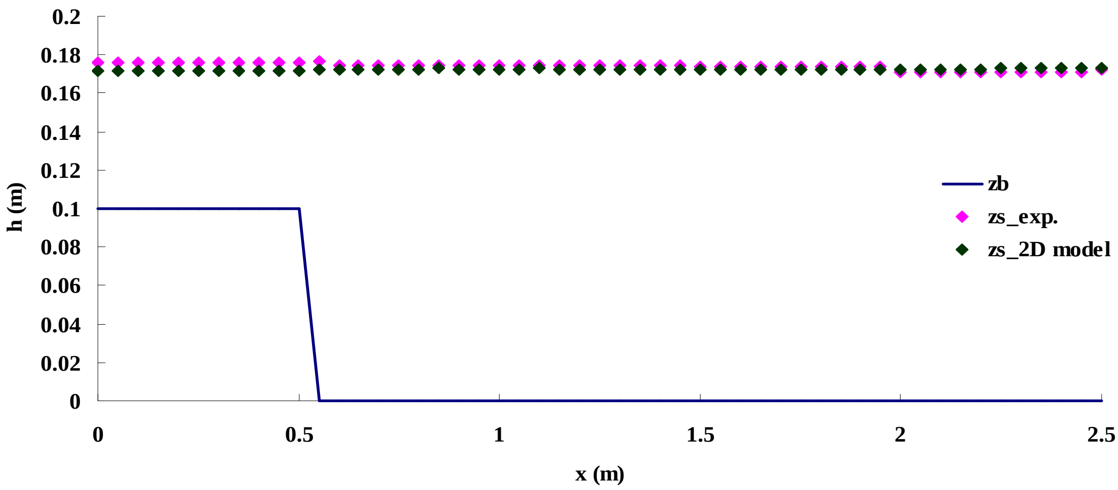

(f) Run 6

Figure 3.11 Verification of water depth at the centerline for both experimental and numerical results.

3.5.2 Flow Characteristics at Drops

The flow depth of the supercritical stream at the immediate downstream of the step "Y_1" (Figure 3.1) was measured and calculated for the cases with free-fall conditions in Run 1, Run 2 and Run 3. The obtained values are compared with values mentioned in the literature obtained by White (1943), Rand (1955) and Chanson (1995) using the below equation:

[White (1943): Analytical solution]

$$\frac{Y_1}{Y_c} = \frac{\sqrt{2}}{\frac{1.5}{\sqrt{2}} + \sqrt{\frac{H}{Y_c} + \frac{3}{2}}} \tag{3.21}$$

[Rand (1955): Model data 0.045< Y_c/H <1]

$$\frac{Y_1}{H} = 0.54\left(\frac{Y_c}{H}\right)^{1.275} \tag{3.22}$$

[Chanson (1995): Analytical solution]

$$\frac{Y_1}{H} = 0.625\left(\frac{Y_c}{H}\right)^{1.326} \tag{3.23}$$

where H is the step height and Y_c is the critical depth.

Figure 3.12 shows that the calculated value of "Y_1" in Run 1, 2 and 3, which appears in blue color, has a good fitting with values predicted by the other authors. However, the observed value (pink color) is mostly higher than predicted ones especially in Run 1 and Run 3. This is because pressure distribution in the pool behind the step was assumed to be hydrostatic, rather than the shear stress along the bed of the pool was neglected, and this might contribute to the difference between predicted and measured values.

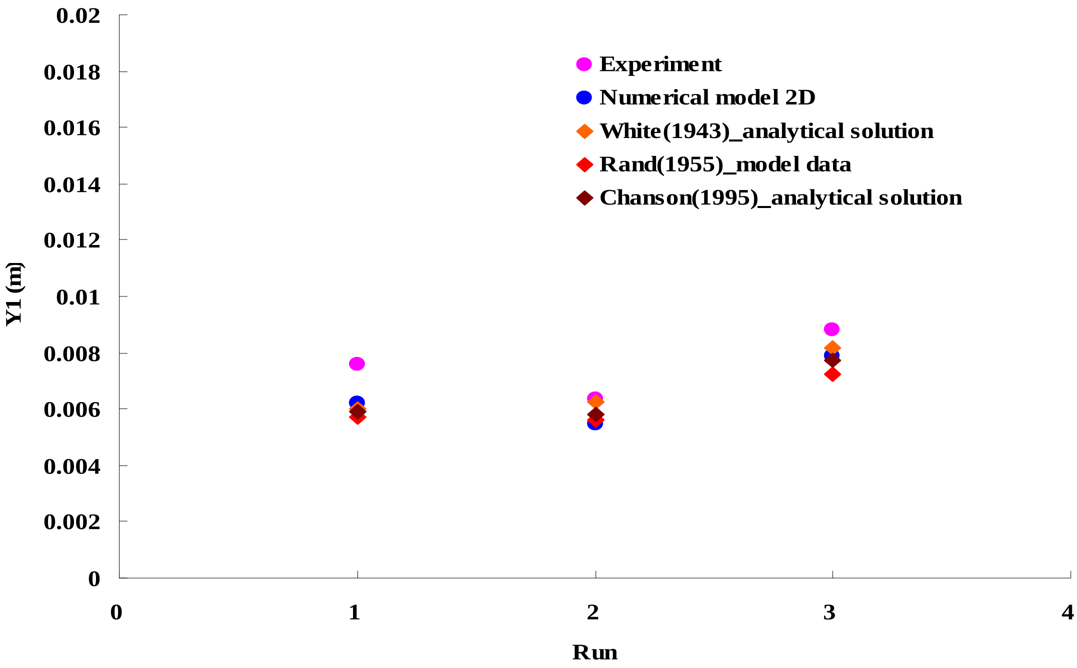

Figure 3.12 Comparison between predicted and experimental values of Y_1.

3.6 Summary

In this chapter, the fundamental study of the flow subjected to sudden change in the geometry of the channel due the existence of a single backward-facing step and the abrupt expansion immediately downstream the step, is analyzed experimentally and numerically. A depth-averaged two-dimensional numerical model for unsteady flow in open channel is applied in a curvilinear grid. The shockwaves generated downstream the step can be represented clearly by using this model.

The backwater effect due to the increase of the water depth downstream the step is also considered. Flows under partially-submerged and fully-submerged steps were also studied experimentally and numerically. The current model gave results which can fit with observed ones in case of fully-submerged steps. However, due to the oscillation that occur at the downstream of the step, the simulated results for the partially-submerged step can't represent properly the experimental results.

A part of the free-over-fall characteristics is considered in this chapter by giving some focus to the depth of the supercritical stream immediately downstream the free-over-fall. The two-dimensional numerical model used in this study presents good results which fit well with previous predicted results.

Chapter 4

SANDBAR FORMATION AND ITS ECOLOGICAL EFFECTS IN THE KAMO RIVER

4.1 Preliminaries

This chapter focuses on the global bar patterns in the Kamo River in addition to the deposition in the immediate downstream of backward-facing step structures. We spotlighted on the ecological changes on the ecosystem of the Kamo River by studying the relation between the habitat of an endangered bird called Kamogawa-Chidori (Charadrius placidus) and the sandbar formation in the immediate downstream of backward-facing step structures with small abrupt expansion at a few locations of the river course. The computational model with two-dimensional (2D) simulation of flow and sediment transport was applied to the bar formations in order to make clear the mechanism of the sand deposition in the immediate downstream of step. The finite volume method in a curvilinear grid was used in the calculations. The two-dimensional shallow water equations are solved with adoption to an equilibrium approach for bed-load sediment transport.

Sediment transport modeling started in the 1950s and has been extensively developed and widely applied to real life engineering since the 1970s (Wu, 2004). Several successful one-dimensional models (Han 1980; Chang 1982; Thomas 1982; Holly and Rahuel 1990; Wu and Vieiria 2002) have been established to calculate the long-term channel deposition and erosion under quasi-steady and unsteady flow conditions. Two-dimensional and three-dimensional sediment transport models have also been established to simulate sediment transport in open channel flow. Examples of these previous studies are: Shimizu et al. (1990); Spasojevic and Holly (1990); Nagata et al. (2000); Wu (2004) and others. These models simulate suspended load transport and bed-load transport.

The sediment transport model described in this chapter adopts the equilibrium transport approach for bed-load. Since that flow and sediment always interact with each other, the model is concern to simulate the flow and sediment transport equations simultaneously. It is applied to the flow properties of the Kamo River in order to predict river flow patterns, bed deformation and plan form variations including the creation of the sandbars at the downstream of the backward-facing steps and along the flow patterns. The model also applied under experimental conditions conducted in the River and Urban Hydraulic Laboratory at Kyoto University.

4.2 Numerical Model

4.2.1 Governing Equations

The depth-averaged continuity and momentum equations in a generalized curvilinear coordinate (ξ,η) were used as governing equations. The equations are described as follow:

[Continuity Equation]

$$\frac{\partial}{\partial t}\left(\frac{h}{J}\right)+\frac{\partial}{\partial \xi}\left(\frac{Uh}{J}\right)+\frac{\partial}{\partial \eta}\left(\frac{Vh}{J}\right)=0 \tag{4.1}$$

[Momentum Equations]

(In the ξ-direction)

$$
\begin{aligned}
&\frac{\partial}{\partial t}\left(\frac{Q^{\xi}}{J}\right)+\frac{\partial}{\partial \xi}\left(\frac{UQ^{\xi}}{J}\right)+\frac{\partial}{\partial \eta}\left(\frac{VQ^{\xi}}{J}\right)\\
&-\frac{M}{J}\left(U\frac{\partial \xi_x}{\partial \xi}+V\frac{\partial \xi_x}{\partial \eta}\right)-\frac{N}{J}\left(U\frac{\partial \xi_y}{\partial \xi}+V\frac{\partial \xi_y}{\partial \eta}\right)\\
&=-gh\left(\frac{\xi_x^2+\xi_y^2}{J}\frac{\partial z_s}{\partial \xi}+\frac{\xi_x\eta_x+\xi_y\eta_y}{J}\frac{\partial z_s}{\partial \eta}\right)-\frac{\tau_b^{\xi}}{\rho J}\\
&+\frac{\xi_x^2}{J}\frac{\partial}{\partial \xi}\left(-\overline{u'^2}h\right)+\frac{\xi_x\eta_x}{J}\frac{\partial}{\partial \eta}\left(-\overline{u'^2}h\right)+\frac{\xi_y^2}{J}\frac{\partial}{\partial \xi}\left(-\overline{v'^2}h\right)\\
&+\frac{\eta_y}{J}\frac{\partial}{\partial \eta}\left(-\overline{v'^2}h\right)+\frac{\xi_x\eta_y+\xi_y\eta_x}{J}\frac{\partial}{\partial \eta}\left(-\overline{u'v'}h\right)+\frac{2\xi_x\xi_y}{J}\frac{\partial}{\partial \xi}\left(-\overline{u'v'}h\right)
\end{aligned}
\tag{4.2}
$$

(In the η-direction)

$$
\begin{aligned}
&\frac{\partial}{\partial t}\left(\frac{Q^{\eta}}{J}\right)+\frac{\partial}{\partial \xi}\left(\frac{UQ^{\eta}}{J}\right)+\frac{\partial}{\partial \eta}\left(\frac{VQ^{\eta}}{J}\right)\\
&-\frac{M}{J}\left(U\frac{\partial \eta_x}{\partial \xi}+V\frac{\partial \eta_x}{\partial \eta}\right)-\frac{N}{J}\left(U\frac{\partial \eta_y}{\partial \xi}+V\frac{\partial \eta_y}{\partial \eta}\right)\\
&=-gh\left(\frac{\xi_x\eta_x+\xi_y\eta_y}{J}\frac{\partial z_s}{\partial \xi}+\frac{\eta_x^2+\eta_y^2}{J}\frac{\partial z_s}{\partial \eta}\right)-\frac{\tau_b^{\eta}}{\rho J}\\
&+\frac{\xi_x\eta_x}{J}\frac{\partial}{\partial \xi}\left(-\overline{u'^2}h\right)+\frac{\eta_x^2}{J}\frac{\partial}{\partial \eta}\left(-\overline{u'^2}h\right)+\frac{\xi_y\eta_y}{J}\frac{\partial}{\partial \xi}\left(-\overline{v'^2}h\right)\\
&+\frac{\eta_y^2}{J}\frac{\partial}{\partial \eta}\left(-\overline{v'^2}h\right)+\frac{\xi_x\eta_y+\xi_y\eta_x}{J}\frac{\partial}{\partial \xi}\left(-\overline{u'v'}h\right)+\frac{2\eta_x\eta_y}{J}\frac{\partial}{\partial \eta}\left(-\overline{u'v'}h\right)
\end{aligned}
\tag{4.3}
$$

where t: time; (x, y): Cartesian coordinates; (ξ, η): boundary fitted-coordinate; h: flow depth; (M, N): x, y components of discharge flux vectors ($M \equiv uh, N \equiv vh$); g: gravity acceleration; ρ: density of fluids; z_s: water surface elevation from the datum plane; $(\tau_b{}^{\xi}, \tau_b{}^{\eta})$: contravariant components of bottom shear stress vectors; ($-\overline{u'^2}$, $-\overline{u'v'}$, $-\overline{v'^2}$): components of depth-averaged Reynolds stress tensors; (ξ_x, η_x, ξ_y, η_y): metrics coordinate transformation; J: Jacobian; (U, V): contravariant components of velocity vectors.

In the sediment motion model, only bed-load transport is considered and it is assumed that grain sorting effects are negligible. The bed-load flux in the stream-wise and transversal direction is evaluated by the following formulae by Meyer-Peter and Mullar (1948) and Hasegawa (1981), respectively.

$$q_{bs} = 8\tau_*^{\frac{3}{2}}\left(1 - \frac{\tau_{*c}}{\tau_*}\right)^{\frac{3}{2}} \tag{4.4}$$

$$q_{bn} = q_{bs}\left(\frac{u_{nb}}{u_{sb}} - \sqrt{\frac{\tau_{*c}}{\mu_s \mu_n \tau_*}}\frac{\partial z_b}{\partial n}\right) \tag{4.5}$$

where τ_*: non-dimensional tractive force acting on the bed; τ_{*c}: non-dimensional critical tractive force acting on the bed; u_{sb} and u_{nb} : s (stream-wise) and n (transversal) components of velocity near the bed; and μ_s and μ_n: coefficients of static and kinematic friction of riverbed.

The velocity u_{nb} near the bed due to the secondary currents is calculated in the following equation.

$$u_{nb} = -N_* \frac{h}{r} u_{sb} \tag{4.6}$$

where r: radius of curvature of the streamline and N_*: coefficient of the strength of the secondary flow (constant).

The non-dimensional tractive force, τ_* in Eq. (4.4) and Eq. (4.5) is given by

$$\tau_* = \frac{C_f (u^2 + v^2)}{((\rho_s / \rho) - 1) g d_m} \tag{4.7}$$

where C_f : bed friction coefficient; ρ_s: density of the bed material and d_m: mean diameter of bed material.

The temporal variation of bed elevation is calculated by Eq. (4.8), after the bed load fluxes (Eq. (4.4) and Eq. (4.5)) are transformed to the ones in the generalized curvilinear coordinates.

[Sediment Continuity Equation]

$$\frac{\partial}{\partial t}\left(\frac{z_b}{J}\right) + \frac{1}{1-\delta}\left\{\frac{\partial}{\partial \xi}\left(\frac{q_b^\xi}{J}\right) + \frac{\partial}{\partial \eta}\left(\frac{q_b^\eta}{J}\right)\right\} = 0 \tag{4.8}$$

where $q_b{}^\xi, q_b{}^\eta$: bed-load transport rate components in (ξ, η) directions respectively; δ : porosity of the bed material

4.2.2 Computational Conditions

The water flow and bed deformation are computed using the above governing equations which are Eq. (4.1), (4.2), (4.3) and (4.8). The first three equations are used to calculate the water flow, while the fourth one is to study the sediment transport in both (ξ,η) directions. Time dependent channel bed deformation is calculated by iteration method by using continuity equation of bed-load sediment transport. The computation procedure is used to calculate the change in flow fields and the channel configuration with time at infinitesimal intervals up to the stability conditions. Firstly, the water flow field in the channel is calculated. Then, the sediment transport rate and riverbed deformation are computed. After that, erosion and sediment deposition are determined. When the erosion and deposition process occurred, the shape of the channel is computed. The calculation is repeated for the next computational time step.

The numerical model is applied to the flow properties of the Kamo River and laboratory experimental conditions. It is used to predict river flow patterns, bed deformation and plan form variations including the creation of the sandbars at the downstream of the backward-facing steps and along the flow patterns. Numerical simulation with the basic equations in a generalized curvilinear coordinate mentioned above is done under the hydraulic conditions listed in Table 4.1.

The length of the computational domain of Run 1 is divided into two parts:

1. 1000 m upstream the joint between the Kamo River and the Takano River;
2. 3000 m downstream the intersection point between the two rivers along the Kamo River.

In Run 2, the length of the computational domain is 300 m along the Kamo River, while the numerical simulation in Run 3 is conducted under hydraulic experiment with a length of the flow domain is equal 4 m.

Table 4.1 Hydraulic computational conditions.

Run	Q (m^3/s)	h_d (m)	Δt (s)
1	120 & 160	1.8	0.005
2	300	1.8	0.00005
3	0.0085	0.022	0.0001

where Q: flow rate; h_d : water depth at downstream end; Δt : time increment.

4.3 Alternate Sandbar Formation

Under suitable conditions of slope flow and sediment discharge, a straight channel evolves into pattern of alternate bars, where the flow is alternately deflected from one bank towards the opposite one (Carrasco-Milian et al. 2009). This process leads to the accumulation of sediment of one bank and the erosion on the other bank due to the flow direction caused by the point-bars erosion and deposition, which can cause flood damage in floodplain and urbanized area. Until recently, alternate bar formation was indeed deemed the inherent mechanism for the meandering of alluvial rivers (Leopolod and Wolman 1957; Callander 1969; Jaeggi 1984; Carrasco-Milian et al. 2009).

Many researches were studied on the alternate bars in a channel with fixed banks. Parker (1976) conducted alternate bars theoretically, while Shimizu and Itakura (1989); Nagata et al. (2000); Wongsa and Shimizu (2006) studied this phenomenon using numerical models. Nagata et al. (2000) studied the relation between alternate bar and bank erosion associated with channel meandering. They proved that bank erosion occurs at the opposite side of each alternate bar.

The Kamo River is one of the main urban rivers, which runs in Kyoto City. The source of this river is Sajikigatake Mountain in the northern ward of Kyoto City. The Kamo River joins the Takano River at an area called “Demachiyanagi” as shown in Figure 4.1.

As reported in (Matsushima et al. 2007), a severe flooding disaster occurred in this river in 1935. A series of river works were implemented in the river. These works include straightening and deepening of the river channel, laying of concrete banking, laying of artificial river beds and a serious of weirs (Matsushima et al. 2007), widening of the channel and the construction of backward-facing step structures. Such like these improvement works decreased the tractive force to transport the sediments of riverbed, which leads to sandbar formation in many places on the river, as shown in Figure 4.2.

In order to simulate the alternate sandbar patterns in the Kamo River, the numerical model mentioned above is applied to the hydraulic computational conditions (Run 1, Table 4.1). The two values of discharge ($Q = 120\,\mathrm{m}^3/\mathrm{s}$ & $Q = 160$ m^3/s) represent the flow rates of the Takano River and the Kamo River respectively. These values of discharges are predicted by bank-full discharge, which is considered as one of the main factors to affect riverbed topography based on Yamamoto (1994).

Figure 4.3 illustrates temporal changes in the bed of the channel at several times for a length of about 4000 m at the join between the Kamo River and the Takano River. An enlargement of the area in between $x = 1000$ m and $x = 4000$ m is shown in Figure 4.4. Due to the changes in the cross sectional forms, the meandering of the channel and the temporal changes in the distribution of tractive forces, alternate point-bars existed at the meander bends of the channel were developed. Alternate bars also appeared downstream the lower channels and complicated bars developed due to the flow direction around the bars. As can be seen from the results (Figure 4.4), the proposed model reasonably succeeded to reproduce a part of the alternate sandbar deposition in the Kamo River.

Figure 4.1 The Kamo River joins the Takano River at Demachiyanagi Area.

Figure 4.2 Existing of alternate sandbars in the Kamo River.

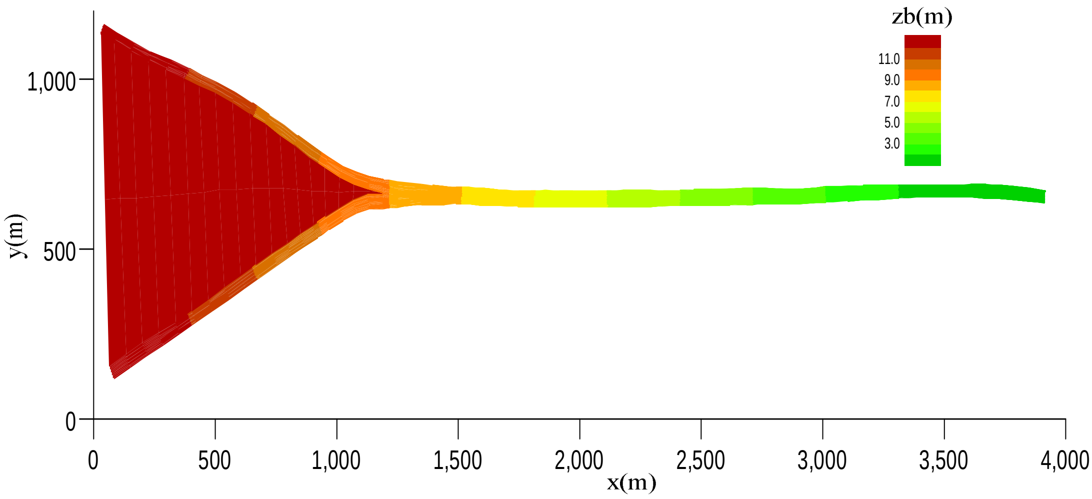

(a) $t = 0hr$

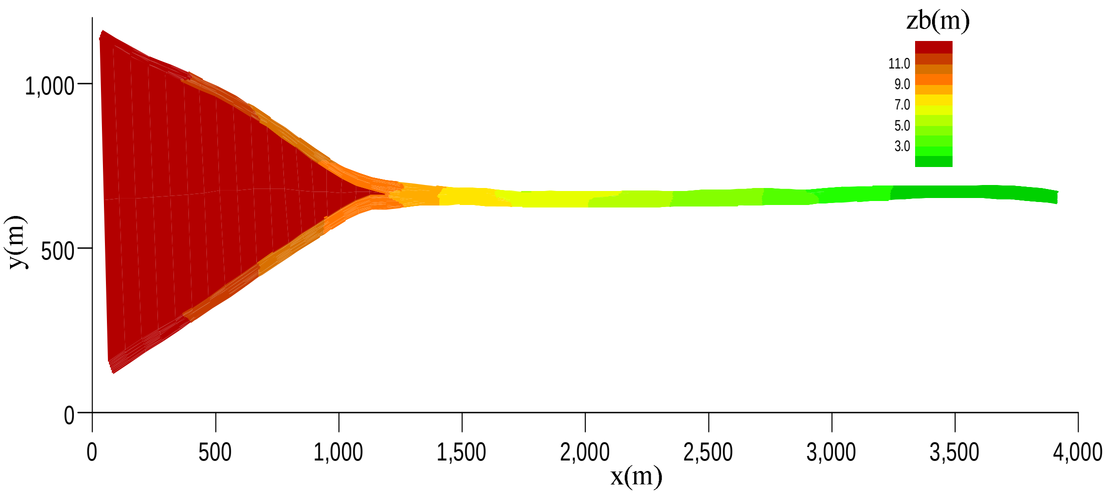

(b) $t = 48hr$

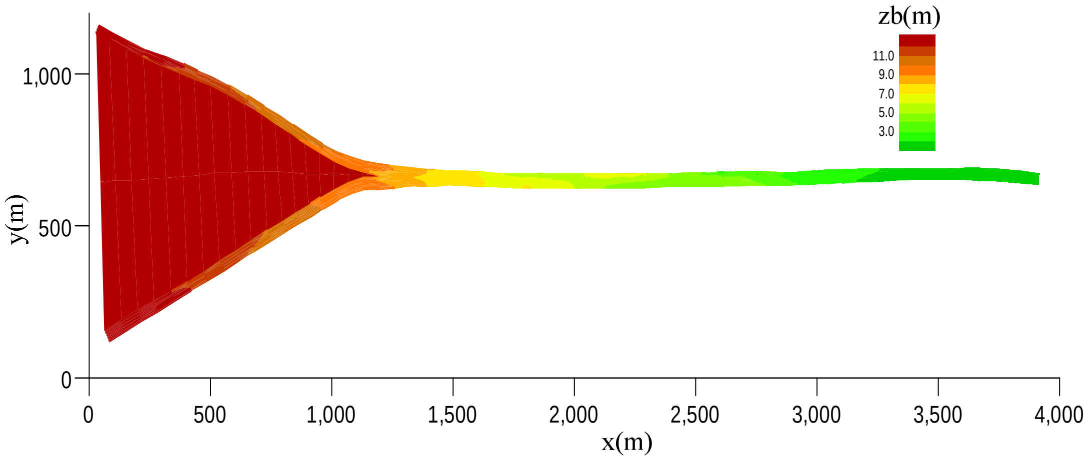

(c) $t = 96hr$

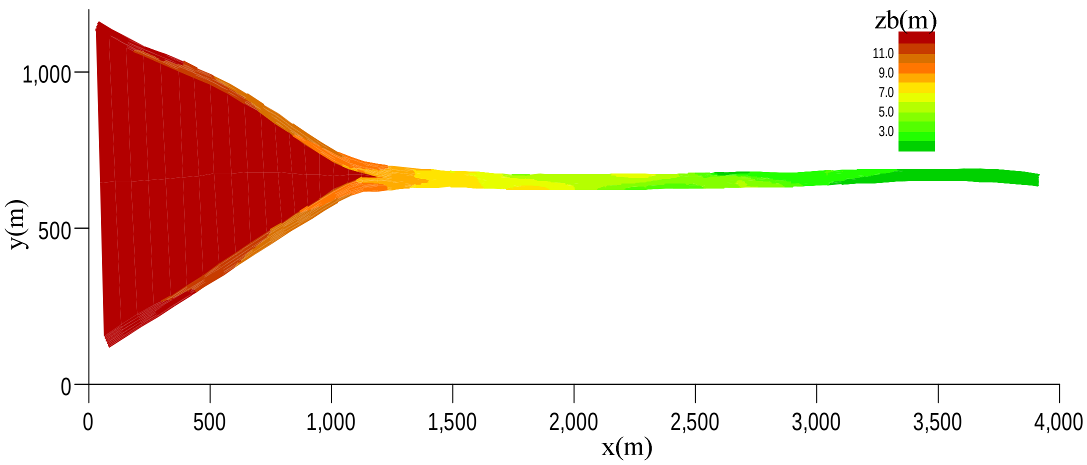

(d) $t = 144hr$

Figure 4.3 Bed deformations at various times in Run 1.

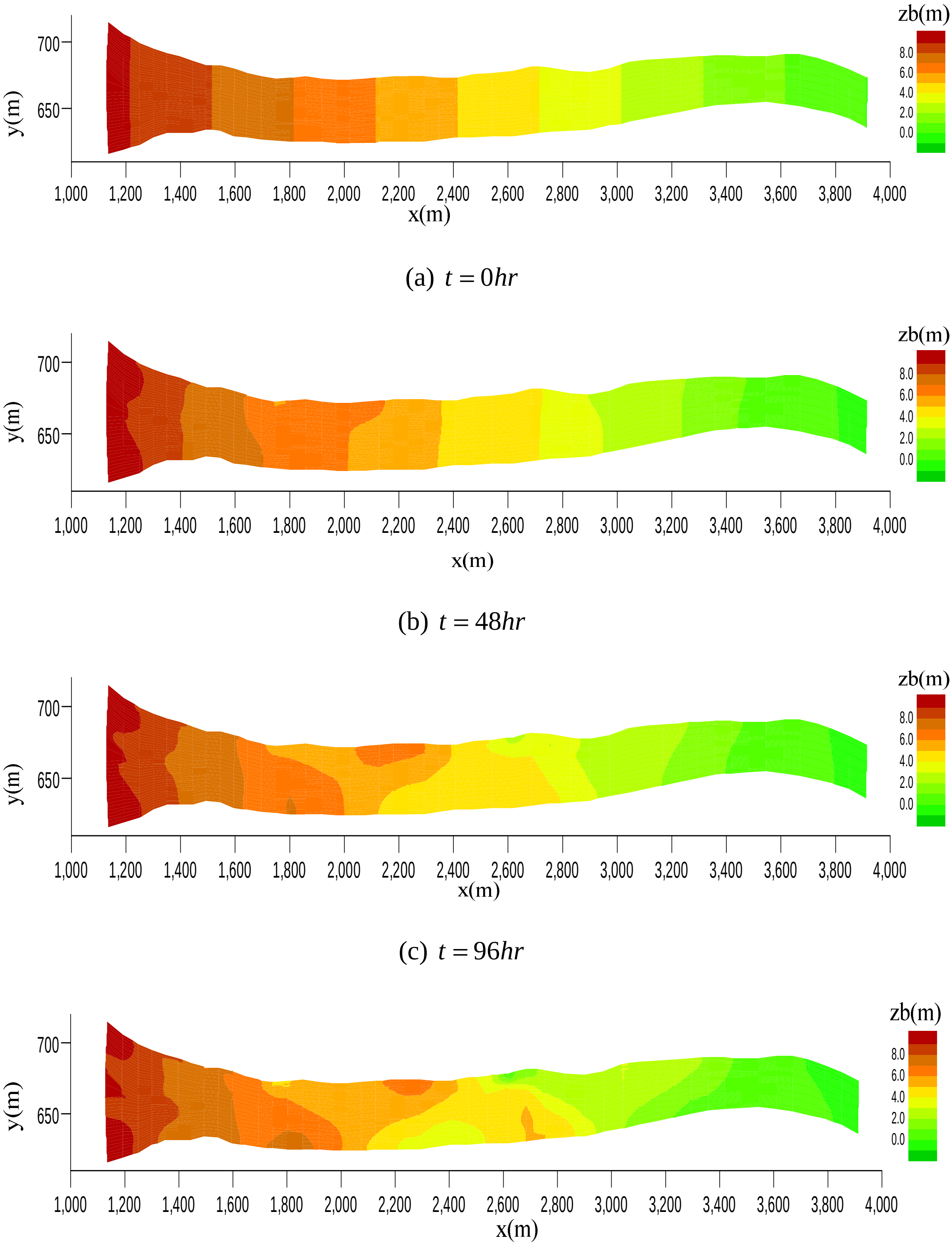

(a) $t = 0hr$

(b) $t = 48hr$

(c) $t = 96hr$

(d) $t = 144hr$

Figure 4.4 Alternate bar patterns in the flow domain of the Kamo River.

4.4 Sandbar Formation in the Immediate Downstream A Step

4.4.1 Experimental Results

A physical experiment is carried out in the same flume described in chapter 3. The hydraulic condition of the experiment is illustrated in Table 4.2.

Table 4.2 Hydraulic conditions of the experiment.

L (cm)	B (cm)	Q (cm^3/s)	h_u (cm)	h_d (cm)	T (℃)
250	91	4051	3.4	1.8	16.5

where L: length of flow domain; B: channel width; Q: discharge; h_u, h_d: upstream and downstream water level respectively; T: water temperature.

In order to study the sediment transport over a backward-facing step, a volume of dimensions (92.5cm x 91cm x 1cm) was filled with sand into the upstream end of the channel (Figure 4.5). The particle size of sand ranged from 0.36 to 0.74 mm (mean diameter is 0.5274 mm). A schematic view of the experimental setup is shown in Figure 4.6.

In the laboratory test, both flow and sediment measurements were carried out. The sediment measurements were conducted for 10cm step height. Temporal variation in sand deposit was measured by taking photographs, and the depth of sand was measured using point gauge instrument.

During the experiment, the sediments are eroded by the accelerated flow at the upstream of the channel and transported over the step. At the downstream of the step, the sediment tends to deposit due to reduce velocity and shear stress, forming as so-called point-bar. This sediment is found to be deposited near about middle of the channel and along the way of shockwaves which generated due the sudden abrupt expansion in the downstream of the step, as shown in Figure 4.7 and Figure 4.8.

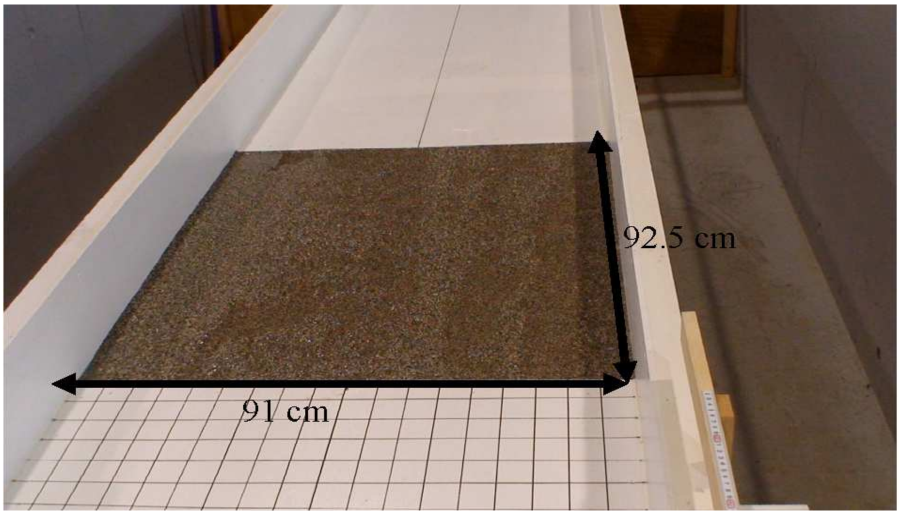

Figure 4.5 Setting of sand transport experiment at the upstream of the step.

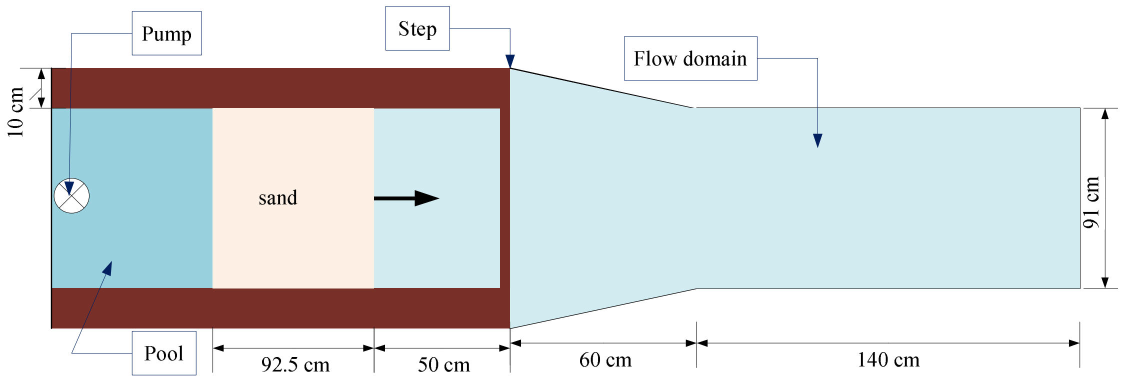

Figure 4.6 Schematic view of the experimental installation of sediment transport over a backward-facing step.

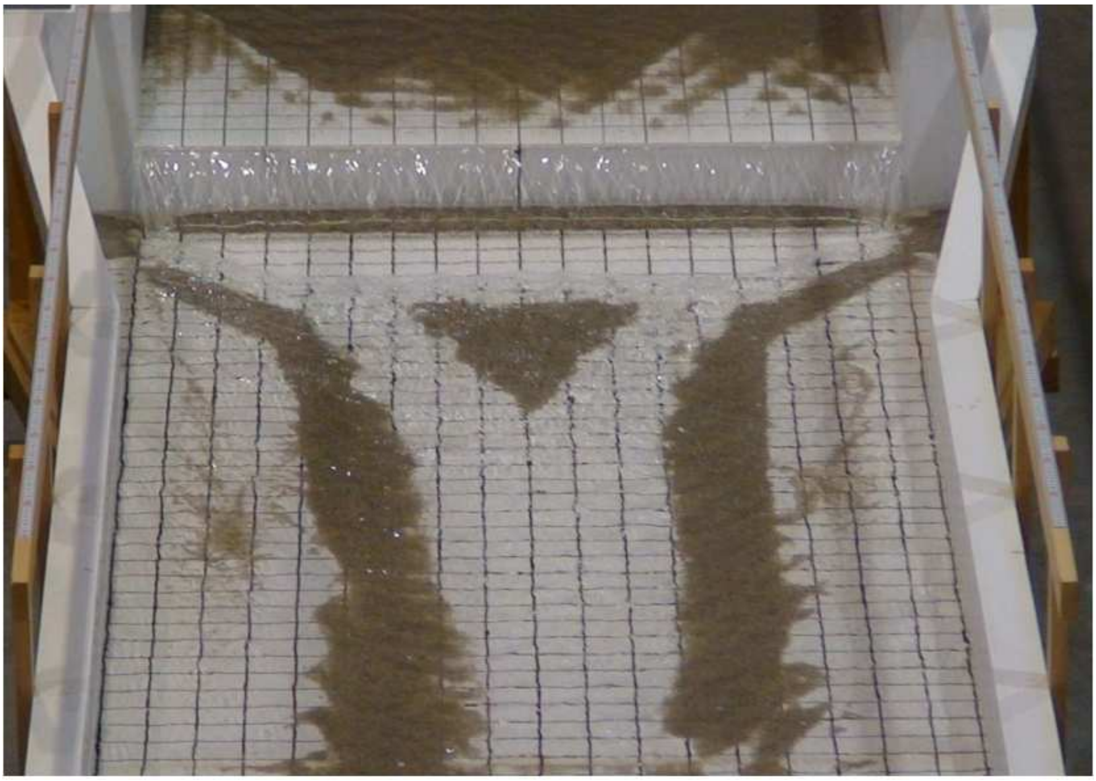

Figure 4.7 Deposition of sand downstream the step.

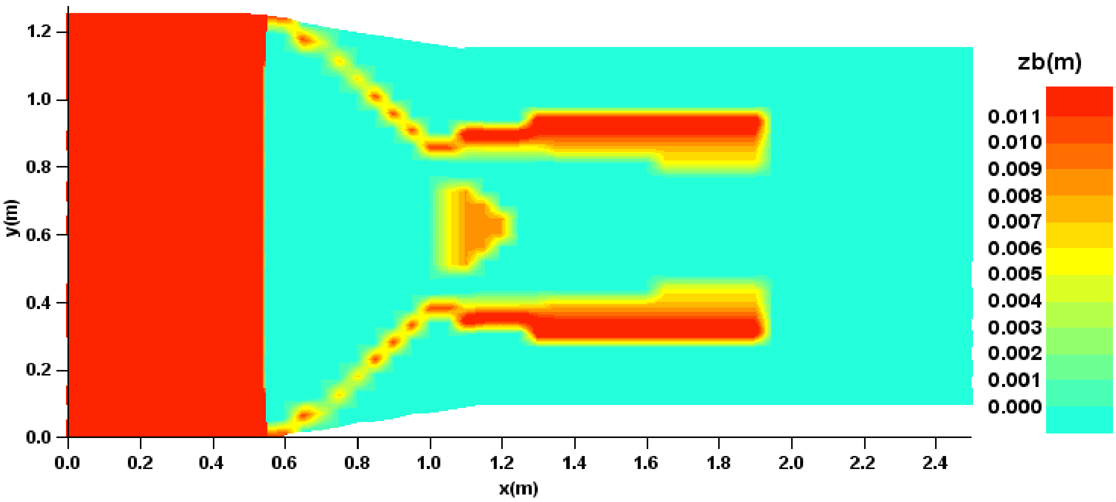

Figure 4.8 Sand deposition downstream the step of laboratory experiment results.

4.4.2 Numerical Results

The depth-averaged two-dimensional (2D) numerical model is also applied to simulate the sediment transport over a backward-facing step by giving an attention to the deposition of sand downstream the step. The model is carried out under actual flow condition of the Kamo River (Run 2, Table 4.1), and under laboratory experiment condition (Run 3, Table 4.1). In both cases, sudden expansion occurs immediately downstream the step. The experiment bed is fixed in Run 3, where bed erosion couldn't be occurred, while bed erosion was occurred while simulating the Kamo River flow conditions.

Numerical simulation results for both cases are shown in Figure 4.9 and 4.10. In the figures, sands tend to be deposited at the immediate downstream of the step as a result of the reduction of the tractive force caused by the location of the backward-facing step. The results in Figure 4.9 illustrate that the major deposition occurred along the shockwave flow patterns with some minor deposition at the middle of the channels. Erosion occurred at the far downstream of the step as well as upstream the step. This results can give a roughly reproduction of the deposition downstream the backward-facing step structure in the Kamo River. On the other hand, the numerical simulation which conducted under experimental conditions (Run 3) failed to reproduce the phenomenon of sand deposition along shockwaves flow patterns downstream the step. However, the model can reproduce clearly the triangular sandbar at the middle of the channel downstream the step. It has a quite good agreement with the observed results.

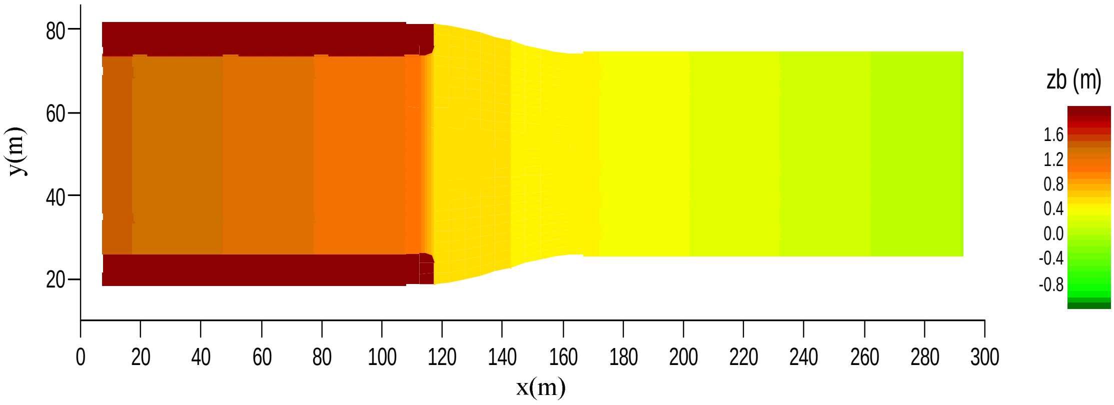

(a) $t = 0hr$

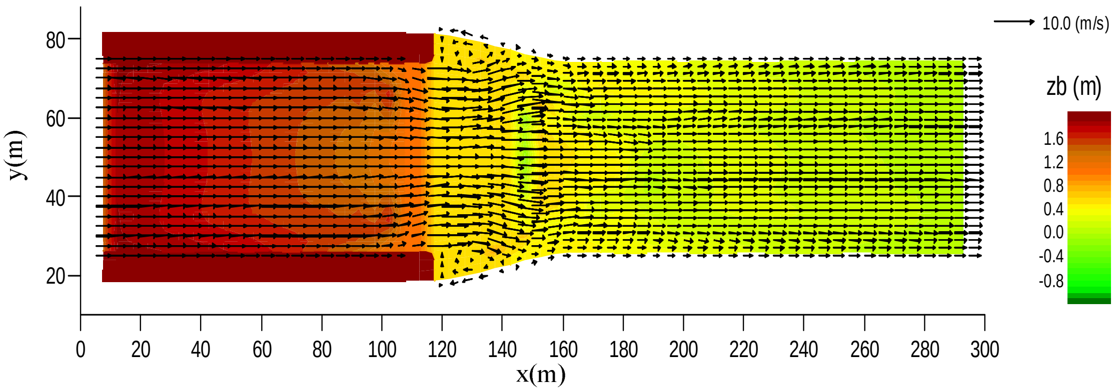

(b) $t = 2.5hr$

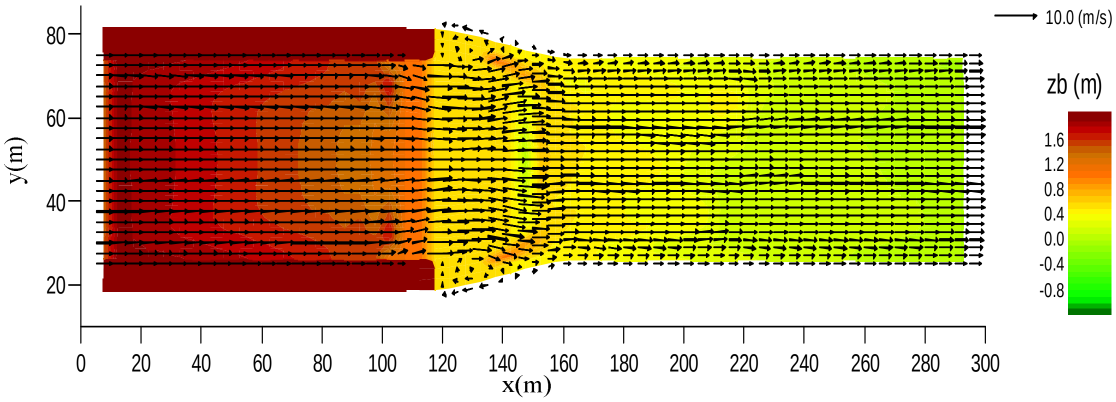

(c) $t = 3hr$

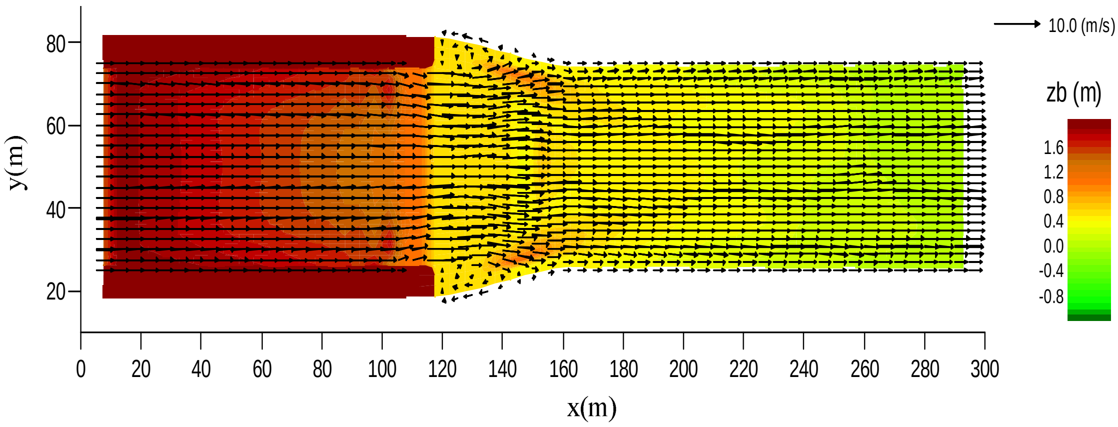

(d) $t = 3.5hr$

Figure 4.9 Sediment depositions along the channel in Run 2.

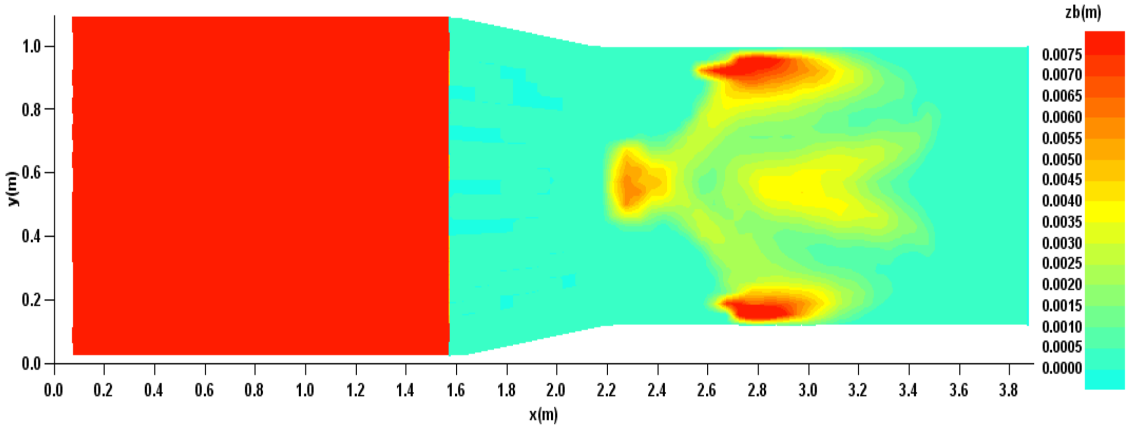

(a) $\Delta x = 0.05m$

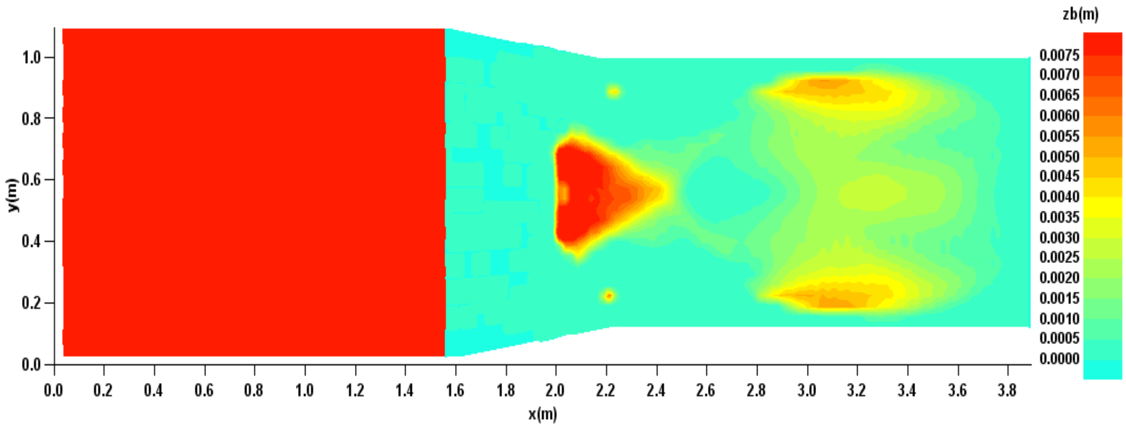

(b) $\Delta x = 0.025m$

Figure 4.10 Sediment depositions downstream the step in Run 3.

4.5 The Ecological Changes on the Ecosystem of the Kamo River

The rapid environmental changes due to river improvement works for the mitigation of flood disasters have occurred in almost all the Japanese Rivers with severe damage on rich river nature. The Kamo River is one of these rivers where some of flood mitigation projects such as backward-facing steps, as mentioned before, were constructed. These works, beside their advantages in flood protection, they affected destructively in the ecosystem of the Kamo River. These effects are reflected in the decrease of the number of endangered plants and birds.

In this chapter, we are dealing with the habitat of an endangered bird called Kamogawa-Chidori (Charadrius placidus). This bird is categorized as "Vulnerable" and its number has been decreased rapidly for several decades. The widening of the main channel and the installation of the series of backward-facing step structures decreased the tractive force to transport the sediments of riverbed. The reduction in tractive force has decreased the area of the favorable habitat (i.e. bare sandbar without vegetation) of this Chidori. Firstly, frequent visits were made to the Kamo River in order to assess the recent situation of the life of Kamogawa-chidori through a year. We revealed that only a few birds live on small area on the bare bars due to the latest deposition in the immediate downstream of backward-facing step structures with small abrupt expansion at a few locations of the river course.

As we focusing on Kamogawa Chidori, its number has been decreased rapidly for several decades. In an observation made by Matsushima et al. (2007) in the period of 10th June 2006 to 27th May 2007, for the area between Kamo Bridge and Sanjo Bridge. The total number of Chidori bird is around 7.

The habitat of the Chidori birds is the bare bar surfaces (Figure 4.11). However, some temporal changes occur in the bed of the river. Examples of these changes are the creation of the alternate bars along the river course. Additionally, there are some sandbars that have triangular shapes existed at the downstream of the backward-facing step structures, as mentioned above. Such of these sandbars allowed the vegetation to grow which decreased the bare surfaces areas where the Chidori likes to live in.

(a) Competitive between birds for staying in a bare surface.

(b) A chidori-bird staying in a bare surface.

Figure 4.11 The bare surfaces are the favorite habitat of chidori.

4.6 Summary

In this chapter, the ecological effects of sandbar formation in the Kamo River are studied. The study focuses on studying the relation between the habitat of Kamogawa Chidori and the existence of the sandbars at the immediate downstream of backward-facing steps structures with small abrupt expansion at a few locations of the river course. Due to the widening of the main channel and the installation of series of backward-facing steps, the tractive force to transport sediment of riverbed has decreased. As a result, the bare bar without vegetation has also decreased. Therefore, the number of chidori birds has been decreased rapidly in the Kamo River.

A two-dimensional numerical model for unsteady open channel flow is applied in curvilinear coordinates to simulate both of water flow and sediment transport. The model is used to simulate the alternate sandbar patterns in the Kamo River. From the results, it can be concluded that, due to the meandering of the channel and the temporal changes in the distribution of tractive forces, alternate point-bars existed at the meander bends of the channel. The model also carried out to study the sediment transport over a backward-facing step by focusing on the deposition of sand downstream the step. The results can give an approximate reproduction of the sand deposition downstream the backward-facing step structures in the Kamo River.

Chapter 5

FREE SURFACE OPEN CHANNEL FLOW DOWNSTREAM OF SIDE DISTURBANCE

5.1 Preliminaries

In this chapter, we deal with the spatial variations of steady open channel flows downstream of an obstacle attached on the sidewall of a flume. It is shown theoretically that using the linearlized equations of two-dimensional (2-D) shallow flows, periodic wavy patterns exist for supercritical flows (Froude number >1), but the amplitude of periodic wavy patterns always attenuates in the downstream direction. Standing waves can exist only in the case the friction coefficient is zero. It is also pointed out that the attenuation rate increases with the increase of Froude number. These results are verified by means of hydraulic experiments carried out in this study. Using shallow flow equations, the numerical analysis is also carried out under the hydraulic conditions of experiments to consider the theoretical and experimental results.

The spatial amplification of the sandbars generated downstream of a point-bar along a river bend is well known as the over-deepening phenomenon of sandbars. As a comprehensive definition of over-deepening phenomenon, Zolezzi et al. (2005) define it as “spatial transient whereby the scour associated with the point-bar configuration establishes in a bend of constant curvature downstream of a straight reach". The point-bar mentioned in the above definition is found usually in a crescent shape on the inside of a stream bend of a meandering stream. Struiksma et al. (1985) formulated over-deepening phenomenon mathematically, and derived the critical conditions for the spatial amplification of sandbars. Blondeaux and Seminara (1985) derived the analytical solutions on the temporal change of point-bars in a sinuous meandering channel. The resonance relation between sinuous channel and bars is included in the solutions. It is well known nowadays that the condition of the spatial amplification of bars by Struiksma et al. (1985) is coincident with the resonance relation by Blondeaux and Seminara (1985).

Hosoda and Nishihama (2006) studied the response of water surface to a sinuous open channel and the flow behavior near the resonance condition. Although there is no resonance condition in the case studied in this paper, it is pointed out that if the bottom variations with the standing wave condition are given, the flow resonates to the bottom variations.

Based on these results, this study doesn't deal with the spatial amplification of sandbars, but it examines the response of the spatial variations of water surface in steady open channel flows downstream of an obstacle attached on the sidewall of a flume.

It is firstly shown theoretically that using the linearlized equations of 2-D shallow flows, the periodic wavy patterns can exist for the supercritical flows condition, but the amplitude of periodic wavy patterns always attenuate downstream direction. The standing waves without attenuation can exist only for the case of zero friction factors. It is also shown that the attenuation rates of periodic wavy patterns increase with the increase of Froude number.

Hydraulic experiments and numerical simulations are carried out to verify the theoretical findings, by changing the hydraulic conditions such as depth, bottom slope, etc.

5.2 Theoretical Considerations

Referring to the coordinate system shown in Figure 5.1, common plane 2-D shallow flow equations are given by Eqs. (5.1), (5.2) and (5.3).

$$\frac{\partial uh}{\partial x}+\frac{\partial vh}{\partial y}=0 \tag{5.1}$$

$$u\frac{\partial u}{\partial x}+v\frac{\partial u}{\partial y}+g\frac{\partial h}{\partial x}=g\sin\theta-\frac{\tau_{bx}}{\rho h} \tag{5.2}$$

$$u\frac{\partial v}{\partial x}+v\frac{\partial v}{\partial y}+g\frac{\partial h}{\partial y}=\qquad -\frac{\tau_{by}}{\rho h} \tag{5.3}$$

where (x,y) : Cartesian coordinates; (u,v) : (x,y) components of depth-averaged velocity vectors; h : depth; θ : bottom slope; and (τ_{bx},τ_{by}) : (x,y) components of bottom shear stress vectors.

For simplicity, the following formula with friction factor c_f is applied to evaluate bottom shear stress vectors.

$$\frac{\tau_{bx}}{\rho}=c_f\sqrt{u^2+v^2}\,u,\ \frac{\tau_{by}}{\rho}=c_f\sqrt{u^2+v^2}\,v \tag{5.4}$$

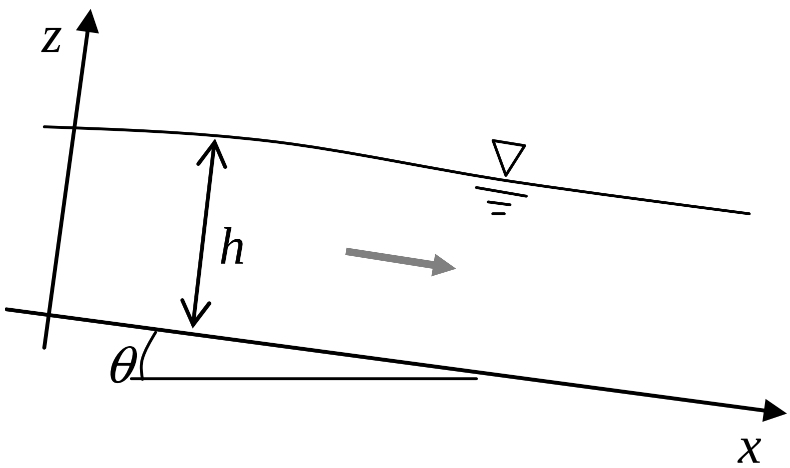

Figure 5.1 Coordinate system and explanation of symbols.

Considering the deviation of depth and velocity from the uniform depth and uniform velocity, we can derive the common linearlized equations. The uniform depth and uniform velocity in the x-direction are given by the following equations:

$$gh_0 \sin\theta = c_f U_0{}^2,\ h_0 U_0 = q \tag{5.5}$$

where h_0 : uniform depth; U_0 : uniform velocity; and q : unit width discharge.

Using the following non-dimensional variables with prime, Eqs.(5.1), (5.2) and (5.3) can be transformed into the linearlized equations, Eqs.(5.6), (5.7) and (5.8).

$$x = Lx',\ y = (B/2)y'$$

$$h = h_0(1+\delta h'),\ u = U_0(1+\delta u'),\ v = U_0 \delta v'$$

$$\frac{\partial \delta u'}{\partial x'} + \frac{\partial \delta h'}{\partial x'} + \beta \frac{\partial \delta v'}{\partial y'} = 0 \tag{5.6}$$

$$\frac{\partial \delta u'}{\partial x'} + \frac{1}{Fr_0{}^2}\frac{\partial \delta h'}{\partial x'} = -\frac{c_f}{\lambda}(2\delta u' - \delta h') \tag{5.7}$$

$$\frac{\partial \delta v'}{\partial x'} + \frac{\beta}{Fr_0{}^2}\frac{\partial \delta h'}{\partial y'} = -\frac{c_f}{\lambda}\delta v' \tag{5.8}$$

where the non-dimensional parameters, $\beta,\ \lambda, Fr_0$ are defined as follow:

$$\beta = \frac{L}{B/2},\ \lambda = \frac{h_0}{L}, Fr_0 = \frac{U_0}{\sqrt{gh_0}}$$

where B : width of channel; L : wave length

From here, primes indicating non-dimensional variables are omitted for simplicity. Periodic standing wave solutions for small disturbances of depth and velocity components $\delta h, \delta u, \delta v$ can be written as:

$$\delta h = a_h \sin\left(\frac{\pi}{2}y\right)\cos(2\pi x) \tag{5.9}$$

$$\delta u = a_u \sin\left(\frac{\pi}{2}y\right)\cos(2\pi x + \phi_u) \tag{5.10}$$

$$\delta v = a_v \cos\left(\frac{\pi}{2}y\right)\cos(2\pi x + \phi_v) \tag{5.11}$$

Where δh , δu , δv are small increment in h , u , v .

Substituting equations (5.9)-(5.11) into (5.6)-(5.8) yields:

$$2\pi a_u \sin\phi_u + \beta(\pi/2)a_v \cos\phi_v = 0 \tag{5.12a}$$

$$-2\pi a_u \cos\phi_u - 2\pi a_h + \beta(\pi/2)a_v \sin\phi_v = 0 \tag{5.12b}$$

$$-2\pi a_u \sin\phi_u = -2(c_f/\lambda)a_u \cos\phi_u + (c_f/\lambda)a_h \tag{5.13a}$$

$$-2\pi a_u \cos\phi_u - (1/Fr_0{}^2)2\pi a_h = 2(c_f/\lambda)a_u \sin\phi_u \tag{5.13b}$$

$$-2\pi a_v \sin\phi_v + (\beta/Fr_0{}^2)(\pi/2)a_h = -(c_f/\lambda)a_v \cos\phi_v \tag{5.14a}$$

$$-2\pi a_v \cos\phi_v = (c_f/\lambda)a_v \sin\phi_v \tag{5.14b}$$

It can be shown easily that Eqs.(5.12)-(5.14) have solutions with physical meaning only in the case of $c_f = 0$. The solutions are given by Eqs.(5.15), (5.16) and (5.17).

$$a_u \sin\phi_u = 0,\ a_u \cos\phi_u = -\frac{a_h}{Fr_0{}^2} \tag{5.15}$$

$$a_v \sin\phi_v = \frac{\beta a_h}{4Fr_0{}^2},\ a_v \cos\phi_v = 0 \tag{5.16}$$

$$Fr_0{}^2 = 1 + \frac{\beta^2}{16} \tag{5.17}$$

Eq.(5.17) shows the relation between Froude number of flow and wave length of standing waves. Eq.(5.17) indicates that the standing waves exist under the condition of supercritical flow.

Introducing the spatial functions of amplitudes, $a_h(x), a_u(x), a_v(x)$ in Eqs.(5.18), (5.19) and (5.20), the equations on $a_h(x), a_u(x), a_v(x)$ can be derived as Eqs.(5.21a,b), (5.22a,b) and (5.23a,b).

$$\delta h = a_h(x)\sin\left(\frac{\pi}{2}y\right)\cos(2\pi x) \tag{5.18}$$

$$\delta u = a_u(x)\sin\left(\frac{\pi}{2}y\right)\cos(2\pi x + \phi_u) \tag{5.19}$$

$$\delta v = a_v(x)\cos\left(\frac{\pi}{2}y\right)\cos(2\pi x + \phi_v) \tag{5.20}$$

$$\frac{da_u}{dx}\cos\phi_u - 2\pi a_u \sin\phi_u + \frac{da_h}{dx} - \beta\frac{\pi}{2}a_v \cos\phi_v = 0 \tag{5.21a}$$

$$-\frac{da_u}{dx}\sin\phi_u - 2\pi a_u \cos\phi_u - 2\pi a_h + \beta\frac{\pi}{2}a_v \sin\phi_v = 0 \tag{5.21b}$$

$$\frac{da_u}{dx}\cos\phi_u - 2\pi a_u \sin\phi_u + \frac{1}{Fr_0^{\,2}}\frac{da_h}{dx} = -2\frac{c_f}{\lambda}a_u\cos\phi_u + \frac{c_f}{\lambda}a_h \tag{5.22a}$$

$$-\frac{da_u}{dx}\sin\phi_u - 2\pi a_u \cos\phi_u + \frac{1}{Fr_0^{\,2}}2\pi a_h = -2\frac{c_f}{\lambda}a_u\sin\phi_u \tag{5.22b}$$

$$\frac{da_v}{dx}\cos\phi_v - 2\pi a_v \sin\phi_v + \frac{\beta}{Fr_0^{\,2}}a_h\frac{\pi}{2} = -\frac{c_f}{\lambda}a_v\cos\phi_v \tag{5.23a}$$

$$-\frac{da_v}{dx}\sin\phi_v - 2\pi a_v \cos\phi_v = \frac{c_f}{\lambda}a_v\sin\phi_v \tag{5.23b}$$

Substituting the following functions given by Eq.(5.24) as $a_h(x)$, $a_u(x)$ and $a_v(x)$ into Eqs. (5.21), (5.22) and (5.23), the relation on the spatial amplification/attenuation rate of disturbances, α and phase lag between depth variations and velocities can be derived as Eqs.(5.25), (5.26), (5.27) and (5.28).

$$a_h(x) = A_h\exp(\alpha x), a_u(x) = A_u\exp(\alpha x), a_v(x) = A_v\exp(\alpha x) \tag{5.24}$$

$$\cos\phi_u = \frac{P_{\cos\phi u}}{Q_{\cos\phi u}},\ \sin\phi_u = \frac{P_{\sin\phi u}}{Q_{\sin\phi u}}, \tag{5.25}$$

$$\cos\phi_v = \frac{P_{\cos\phi v}}{Q_{\cos\phi v}},\ \sin\phi_v = \frac{P_{\sin\phi v}}{Q_{\sin\phi v}} \tag{5.26}$$

$$P_{\cos\phi u} = \left(\alpha A_u + 2\frac{c_f}{\lambda}A_u\right)\left(-\frac{1}{Fr_0^{\,2}}\alpha A_h + \frac{c_f}{\lambda}A_h\right) - \frac{4\pi^2}{Fr_0^{\,2}}A_uA_h$$

$$Q_{\cos\phi u} = \left(\alpha A_u + 2\frac{c_f}{\lambda}A_u\right)^2 + 4\pi^2A_u^{\,2}$$

$$P_{\sin\phi u} = -2\pi A_u\left(-\frac{1}{Fr_0^{\,2}}\alpha A_h + \frac{c_f}{\lambda}A_h\right) - \frac{2\pi}{Fr_0^{\,2}}A_h\left(\alpha A_u + 2\frac{c_f}{\lambda}A_u\right)$$

$$Q_{\cos\phi u} = Q_{\sin\phi u}$$

$$P_{\cos\phi v} = -\frac{\beta}{Fr_0^{\,2}}\frac{\pi}{2}A_h\left(\alpha A_v + \frac{c_f}{\lambda}A_v\right)$$

$$P_{\sin\phi v} = \frac{\beta}{Fr_0^{\,2}}\pi^2A_hA_v$$

$$Q_{\cos\phi v} = Q_{\sin\phi v} = \left(\alpha A_v + \frac{c_f}{\lambda}A_v\right)^2 + 4\pi^2A_v^{\,2}$$

$$\alpha \frac{\left(\alpha + 2\frac{c_f}{\lambda}\right)\left(-\frac{\alpha}{Fr_0^{\ 2}} + \frac{c_f}{\lambda}\right) - \frac{4\pi^2}{Fr_0^{\ 2}}}{\left(\alpha + 2\frac{c_f}{\lambda}\right)^2 + 4\pi^2} + 2\pi \frac{2\pi \frac{c_f}{\lambda} + 2\pi \frac{2}{Fr_0^{\ 2}} \frac{c_f}{\lambda}}{\left(\alpha + 2\frac{c_f}{\lambda}\right)^2 + 4\pi^2}$$
$$+ \alpha + \beta^2 \left(\frac{\pi}{2}\right)^2 \frac{\frac{1}{Fr_0^{\ 2}}\left(\alpha + \frac{c_f}{\lambda}\right)}{\left(\alpha + \frac{c_f}{\lambda}\right)^2 + 4\pi^2} = 0 \tag{5.27}$$

$$\alpha \frac{\left(-\frac{\alpha}{Fr_0^{\ 2}} + \frac{c_f}{\lambda}\right) + \frac{1}{Fr_0^{\ 2}}\left(\alpha + 2\frac{c_f}{\lambda}\right)}{\left(\alpha + 2\frac{c_f}{\lambda}\right)^2 + 4\pi^2} - \alpha \frac{\left(\alpha + 2\frac{c_f}{\lambda}\right)\left(-\frac{\alpha}{Fr_0^{\ 2}} + \frac{c_f}{\lambda}\right) + \frac{4\pi^2}{Fr_0^{\ 2}}}{\left(\alpha + 2\frac{c_f}{\lambda}\right)^2 + 4\pi^2} - 1$$
$$- \frac{\beta^2}{Fr_0^{\ 2}} \left(\frac{\pi}{2}\right)^2 \frac{1}{\left(\alpha + \frac{c_f}{\lambda}\right)^2 + 4\pi^2} = 0 \tag{5.28}$$

Substituting the following functional form, Eqs.(5.29) and (5.30) with c_f / λ to derive the approximate solution, the coefficients in these equations can be determined as Eqs.(5.31) and (5.32).

$$\alpha = a_0 + a_1 \left(\frac{c_f}{\lambda}\right) \tag{5.29}$$

$$\beta^2 = 16\left(Fr_0^{\ 2} - 1\right) + b_1 \left(\frac{c_f}{\lambda}\right) \tag{5.30}$$

$$a_0 = 0, \ \ a_1 = -\frac{1}{2} \frac{Fr_0^{\ 2} + 1}{Fr_0^{\ 2} - 1} \tag{5.31}$$

$$b_1 = 0 \tag{5.32}$$

Eq. (5.31) indicates that the spatial disturbances always attenuate in the downstream direction of supercritical flows, and the attenuation rate decreases with the increase of Froude number. Eq. (5.32) indicates that periodic disturbances can not exist in subcritical flows.

The propagation of space variations in supercritical flows can be considered as the propagation of skew shockwave or cross-wave which appears on side in alternate shifts by the transverse variations of water depth which occur at upstream.

The angle of the propagation of skew shockwave is variable and is changed by extent of discontinuity. So we consider the propagation of the characteristic line which is obtained by liner equations in order to make it simple.

Characteristic lines are defined as lines on which transverse derivative of the value can not be established. The discontinuity of derivative of the value is transmitted up to these lines. It indicates that the discontinuity of derivative of the water depth with respect to space is transmitted and reflected at right side as shown in Figure 5.2, when the disturbance is given at left side. The oblique line in the figure presents the flow streamline.

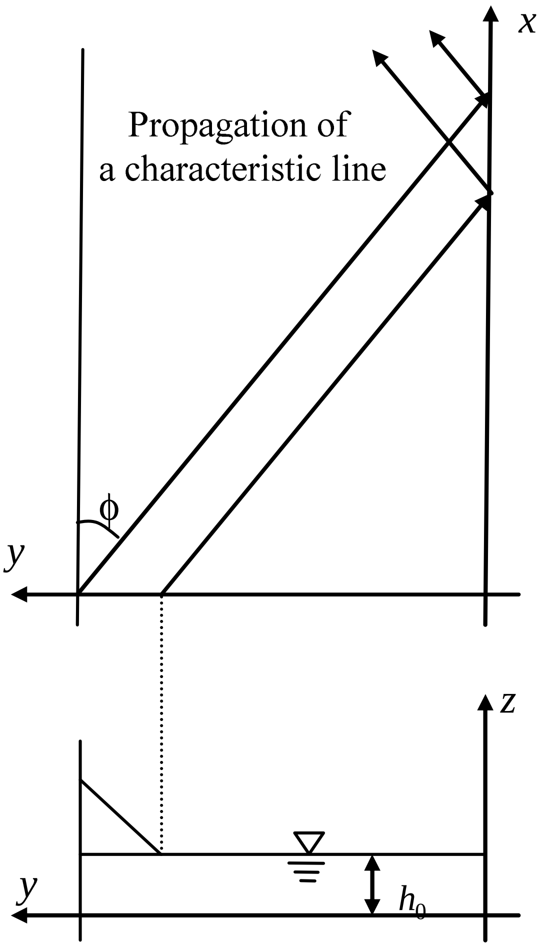

Figure 5.2 Propagation of cross-waves along a characteristic line.

The angel ϕ of propagation is derived as Eq. (5.33). It indicates that wavelength to the direction of flow in the periodic space variation which is given by Eqs. (5.9), (5.10), (5.11) equals to wavelength of cross-wave.

$$\tan\phi = \frac{1}{\sqrt{Fr_0^{\ 2} - 1}} \tag{5.33}$$

This analysis of the periodic space variation by using Eqs. (5.9), (5.10), (5.11) has the relation to the analysis in which the only main terms given by Fourier transform of the cross-wave formation are considered. We can explain that basic features of cross-wave to some extend by the analytical method as it is indicated above. Moreover, this analysis of the periodic space variation is easy and useful in the phenomena which it is difficult to deal with as cross-wave.

5.3 Hydraulic Experiments

The laboratory tests were carried out to verify the results obtained by theoretical considerations. A schematic illustration of the experimental setup is shown in Figure 5.3.

As shown in the figure, an obstacle with the Gaussian shape of the function, $y = A\exp(-Bx^2)$, is attached at 350 cm from the upstream end at the left sidewall of the flume. A plot of the obstacle shape is shown in Figure 5.4. The shape of the obstacle is chosen in this shape to represent approximately the flow around bridge piers in a river with a steep slope. The obstacle attached at the sidewall with a curved shape in the flume can act as a half of the bridge pier, and the flow patterns can be a symbol of the flow around one side of the pier.

The hydraulic experiments were conducted to examine the amplification or attenuation of water surface variations in the downstream of the obstacle. Measurement of water depths was carried out by using point-gauge instrument.

Ten cases were performed under different hydraulic conditions. Nine cases were carried out under supercritical flow condition and one case under subcritical flow condition. The hydraulic variables for the laboratory tests are listed in Table 5.1.

Figure 5.5 shows photographs of flows in Run 1 and 4, while the contour maps of depth are shown in Figure 5.6.

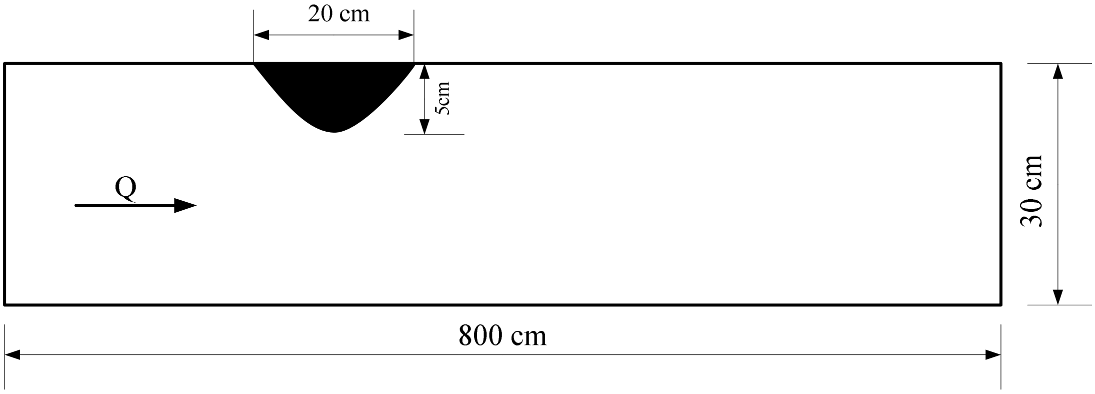

Figure 5.3 Schematic illustration of the flume.

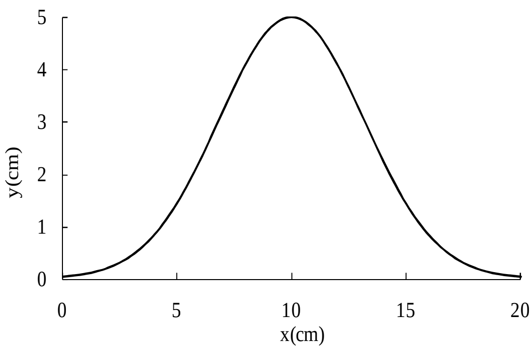

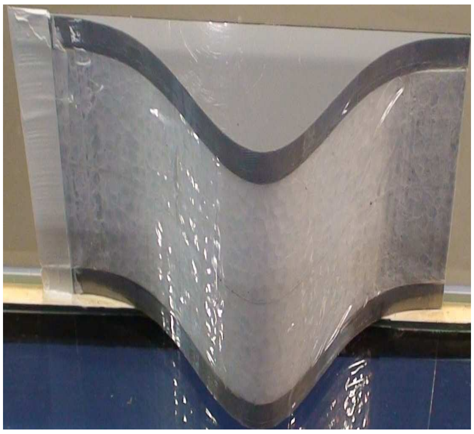

Figure 5.4 Shape function of an obstacle.

Table 5.1 Hydraulic variables in the laboratory tests.

Run number	Discharge (cm^3/s)	Initial water depth (cm)	Initial average velocity (cm/s)	Froude number at upstream	Bed slope	Water Temperature (℃)
1	6,400	1.74	122.6	2.97	1/34	19.0
2	10,900	2.73	133.1	2.57	1/34	13.5
3	5,950	1.45	136.8	3.63	1/13	19.2
4	7,230	3.15	76.5	1.38	1/156	18.6
5	11,410	3.88	98.0	1.59	1/156	13.2
6	6,620	2.08	106.1	2.35	1/49	13.6
7	11,110	2.96	125.1	2.32	1/49	13.6
8	6,200	2.33	88.7	1.89	1/67	13.2
9	11,200	3.28	113.8	2.01	1/67	13.2
10	7,200	4.46	53.8	0.814	1/326	12.9

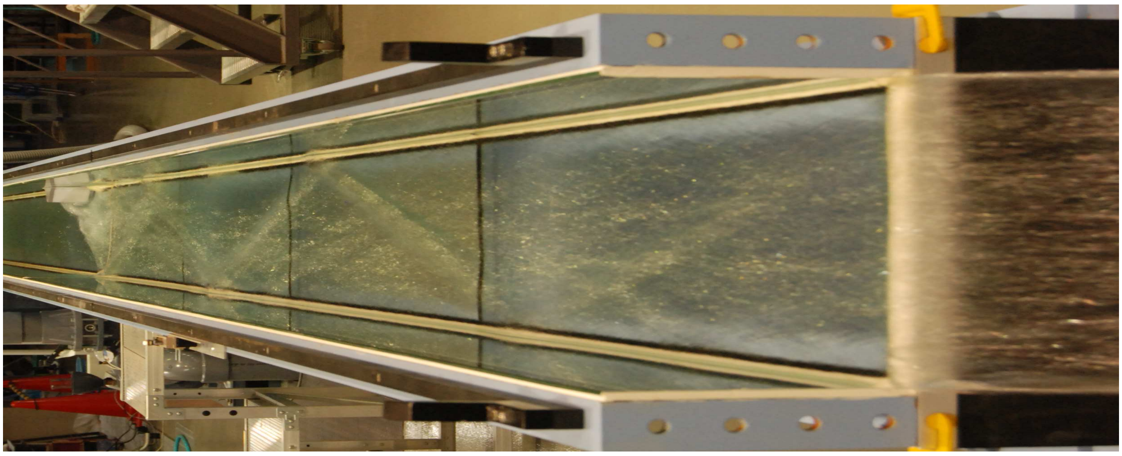

(a) Run 1

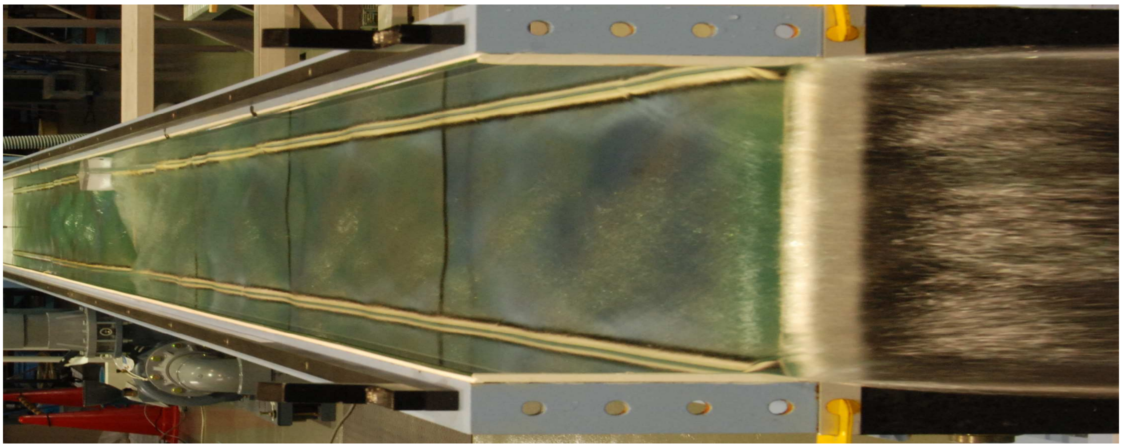

(b) Run 4

Figure 5.5 Water surface variation downstream the obstacle.

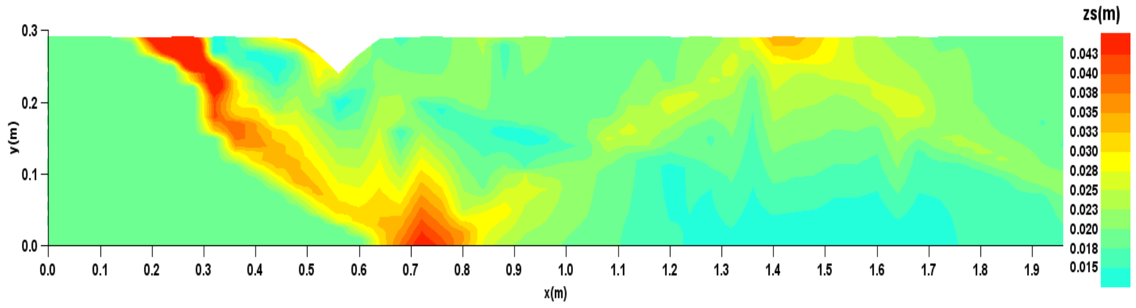

(a) Run 1

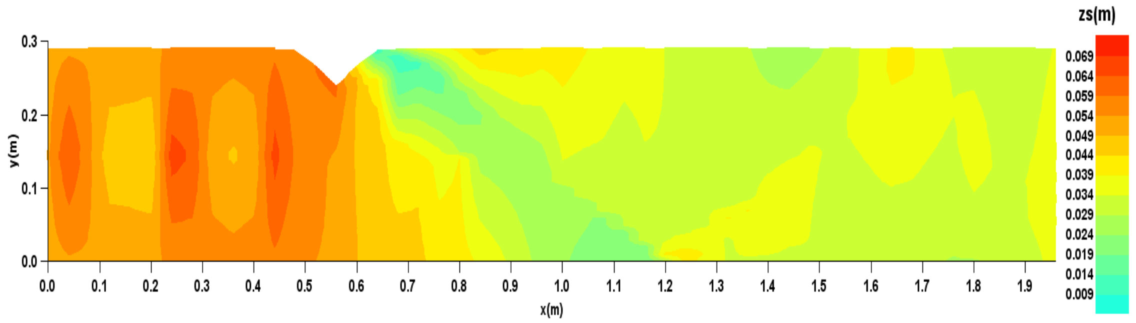

(b) Run 4

Figure 5.6 Contour maps of water depth.

The water surface variations along the both sidewalls are shown in Figure 5.7. It is pointed out that the amplitudes of depth variations attenuate downstream direction for both cases as predicted theoretically in the former section, while we can not identify the magnitude of attenuation rates. It should be noted that since the depth distribution is anti-symmetric, it is necessary to consider the nonlinear effects in the theoretical analysis.

Figure 5.8 shows the relation between wavelength and Froude number for all cases. The solid line in Figure 5.8 is the linear theory given by Eq. (5.17). Experimental data are in a good agreement with the theoretical curve based on linear analysis, although the nonlinear effect seems to be dominant.

5.4 Numerical Results

The numerical calculations are executed under the laboratory conditions of Run 1 and Run 4 and compared with the experimental results. Finite volume method with generalized coordinate is used in the calculations. However, TVD-MUSCL method was applied for discretizing the convection term. The numerical grid of the numerical calculations is illustrated in Figure 5.9. The grid size used is 1 cm in each direction carried in around 2.5 m of the waterway included in the calculation domain.

The calculated results of Run 1 and Run 4 are illustrated in surface-contour forms as shown in Figure 5.10. From the results, it can be seen that the numerical model is capable to reproduce water surface variation around disturbance without numerical oscillation.

A comparison of the depth of water distribution in the right and left bank of the channel is shown in Figure 5.11. Run 1 is carried out under high Froude number, while Run 4 is performed under low Froude number. The calculated results almost fit with experiments especially in terms of the wavelength and the amplitude of water surface variation. The depth of water distribution that studied experimentally can be reproduced numerically by using this model.

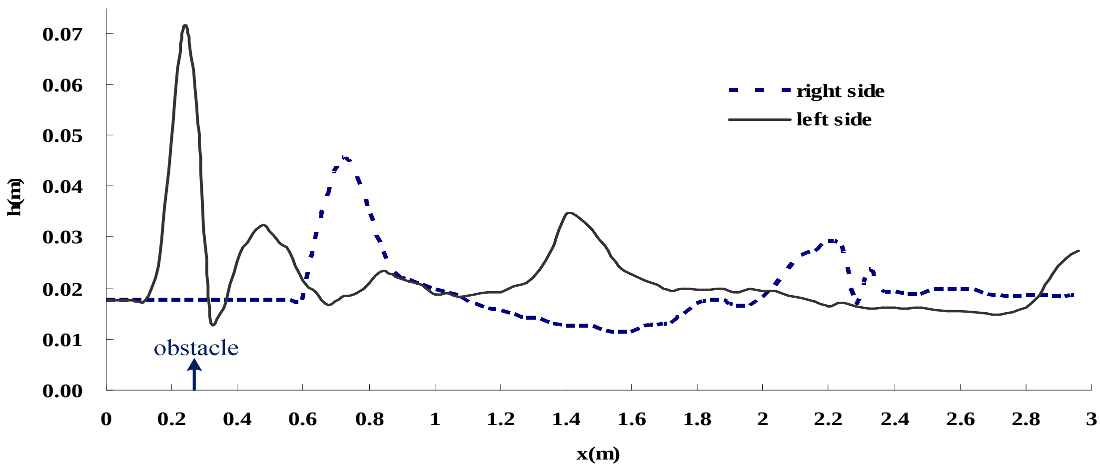

(a) Run 1

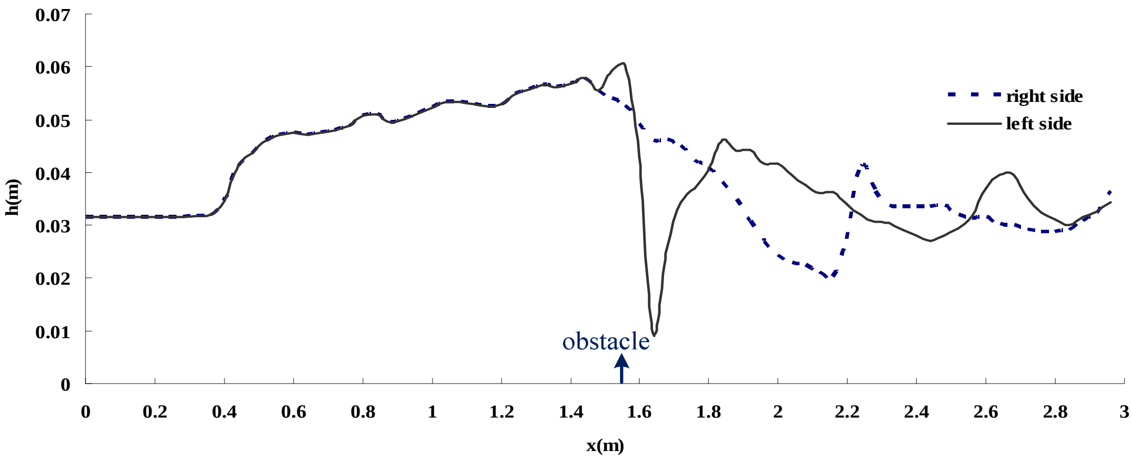

(b) Run 4

Figure 5.7 Water surface variations along sidewalls.

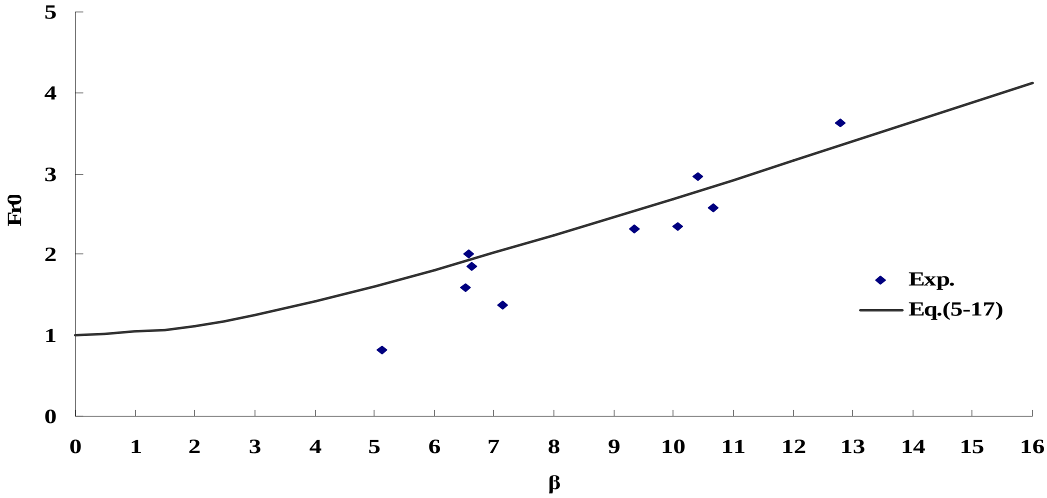

Figure 5.8 Relation between wavelength and Froude number.

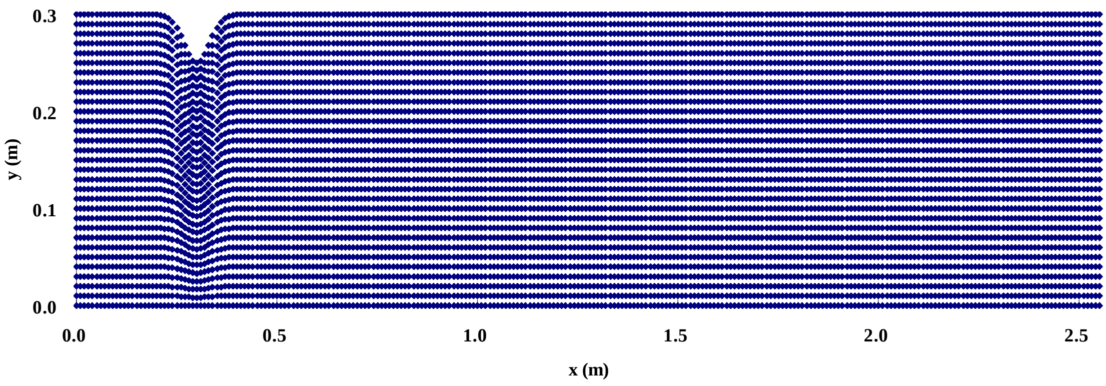

Figure 5.9 Numerical grid used for simulation.

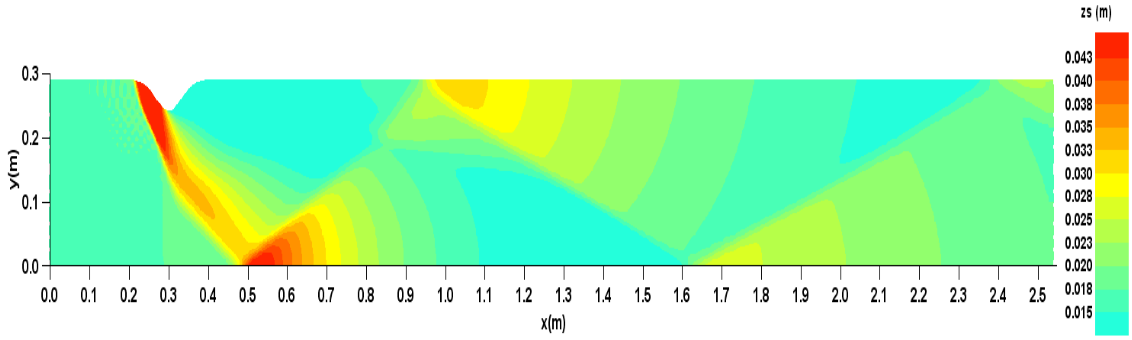

(a) Run 1

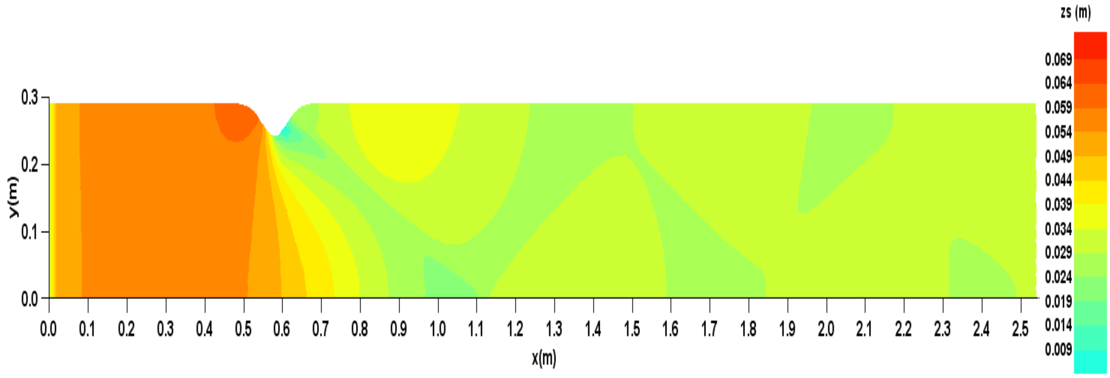

(b) Run 4

Figure 5.10 Contour map of depth for numerical simulation.

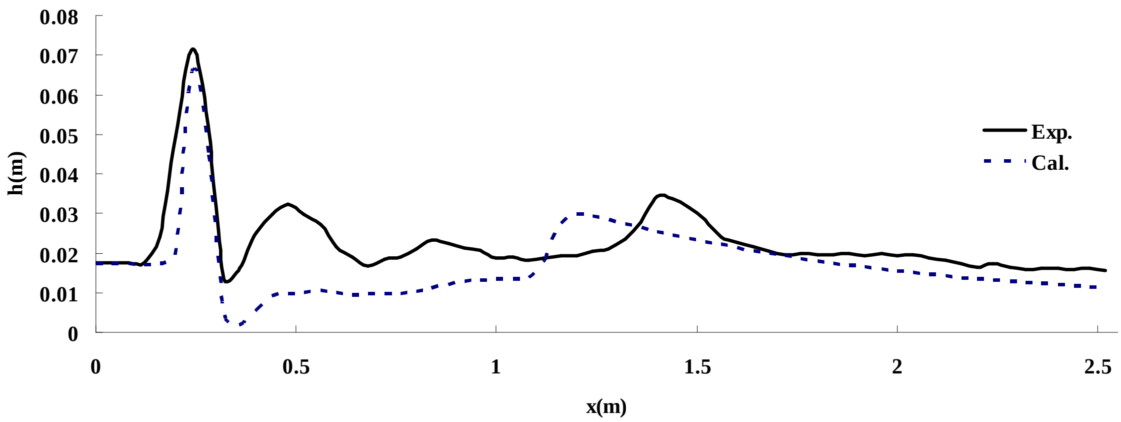

(a) Run 1 (left side)

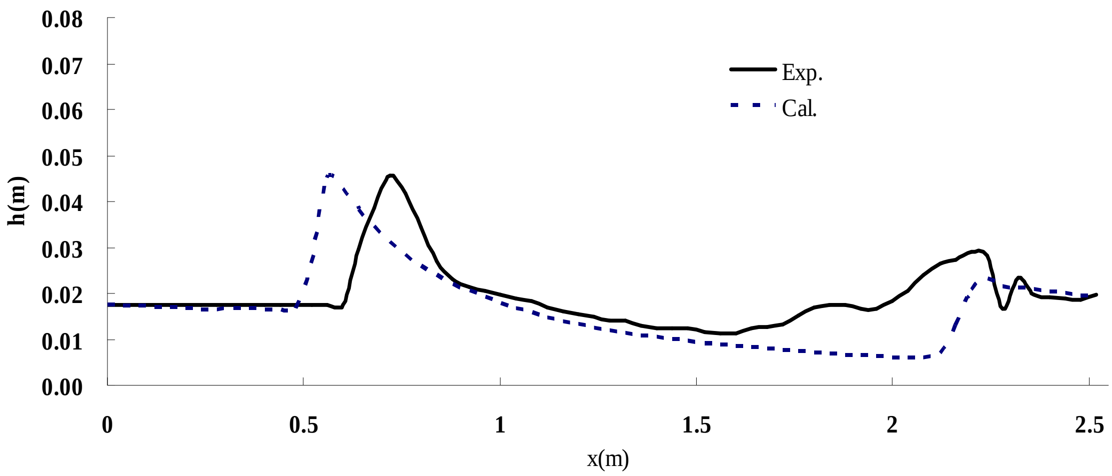

(b) Run 1 (right side)

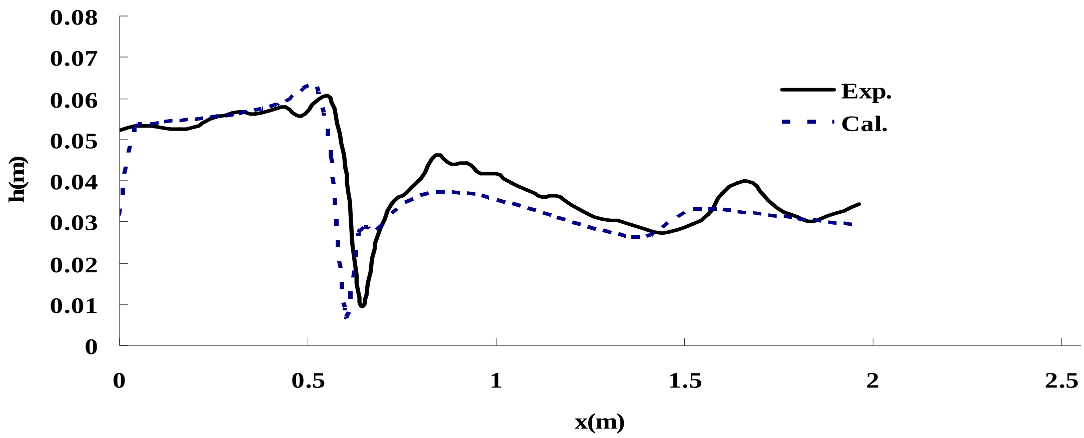

(c) Run 4 (left side)

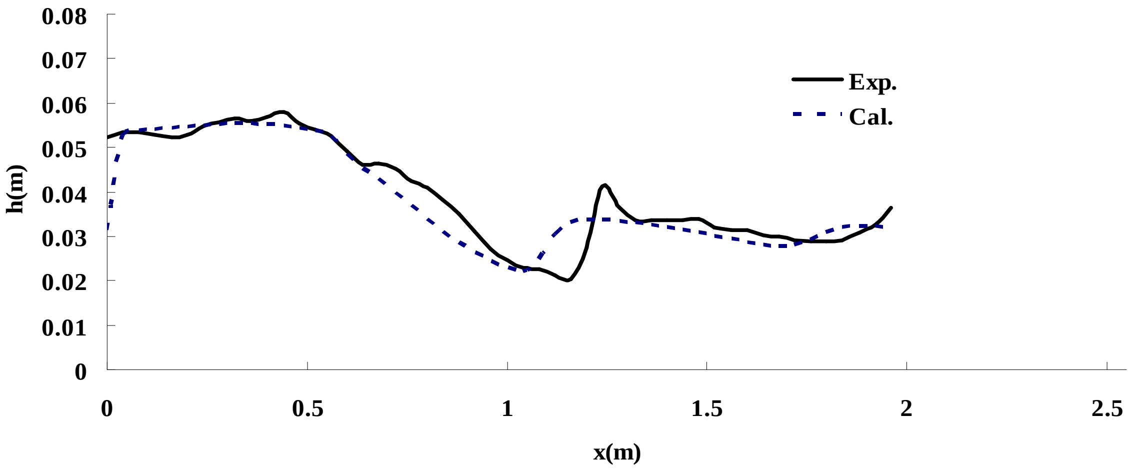

(d) Run 4 (right side)

Figure 5.11 Comparisons of depth distributions between numerical results and experiments.

5.5 Summary

This chapter describes the spatial variations of flow depth in steady open channel flows downstream of an obstacle attached on the sidewall of a flume. It is shown theoretically that using the linearized equations of 2-D shallow flows, periodic wavy patterns exist for supercritical flows (Froude number >1), but the amplitude of periodic wavy patterns always attenuates downstream direction. The attenuation rate increases with the increase of Froude number.

These results are verified by hydraulic experiments carried out in this study. Since the measured depth distributions show very anti-symmetric feature, the further investigation including the non-linear effects is necessary to clarify the generation mechanism of anti-symmetric depth distributions.

The two-dimensional numerical model is executed under the conditions of hydraulic experiments. The numerical calculated results almost fit with the observed one in terms of amplitude of hydraulic wavelength.

Based on results of this study, further researches can be carried to study further the amplification of continuous water surface variations (over-deepening phenomena) by concerning the attenuation processes. Furthermore, we would like to expand the theoretical analysis by studying the non-linear theory. Also, we would improve the numerical model further by considering the vertical acceleration.

Chapter 6

POSSIBILITY OF REPRODUCING FLASH FLOODS USING ONE WATER HYDROGRAPH AT ONE SITE

6.1 Preliminaries

This study is concerned with the reproduction of flash floods with a high Froude number. In order to reproduce unsteady supercritical flows, it is common to give two hydrographs of depth and discharge based on the method of characteristics. Since we pointed out recently the possibility and the computational method to reproduce flood flows for subcritical flows using one depth hydrograph, the theory and method are extended to unsteady supercritical flows in this chapter. Nonlinear analytical solutions with boundary hydrographs at the upstream end are firstly derived. Then, it is proved that the boundary hydrographs at the upstream end can be reproduced inversely, using the solution of one depth hydrograph at one site.

Flash floods are usually caused by heavy or excessive rainfall in a short period of time. They are extremely dangerous because of their sudden nature. They are considered as one of the most dangerous weather-related natural disasters in the world, and can create hazardous situations for people and cause extensive damage to property. Flash flood waters move at very fast speeds and can kill people, roll boulders, tear out trees, destroy buildings, obliterate bridges and increase the potential of landslides and mudslides (Lin, 1999).

Measures to mitigate and prepare for flash floods are therefore of primary importance for urban planning and agricultural land development projects within the flash flood prone areas. Low infiltration capacity is the most important factor for overland flow development (Smith and Ward, 1998), which makes Overland flow, tends to play the dominant role in flash flood formation.

Flash floods in arid environments are in fact common, but their occurrence is also poorly understood. Rainfall-runoff modeling is a primary tool used in flash flood studies; however, the literature has shown that these models are inadequate for prediction, mitigation or management.

Physical and numerical models are useful in analyzing floods especially in catchments where data is not available for simulating extreme storms. The use of these models is necessary in the urban watershed with high variability of land surface parameters, and absence of calibration data. On the other hand, uncertainty should be taken in account in analyzing the results in such cases.

6.2 Theoretical Considerations

In order to reproduce unsteady supercritical flows, it is common to give two hydrographs of depth and discharge based on the method of characteristics. This study is concerned with the reproduction of flash floods with a high Froude number. And we prove that such flows can be reproduced, using one depth hydrograph at one site.

Hosoda et al. (2010) pointed out the possibility to reproduce flood flows for subcritical flows using one depth hydrograph at one middle site between upstream and downstream boundaries and proposed the computational method to reproduce flood flows, considering only one depth hydrograph at one middle site.

This method is extended to unsteady supercritical flows in this chapter. Nonlinear analytical solutions with boundary hydrographs at the upstream end are firstly derived. Then, it is proved that the boundary hydrographs at the upstream end can be reproduced inversely, using the solution of one depth hydrograph at one site.

Referring to the coordinate system shown in Figure 6.1, we assume the flow for supercritical flows in the section measures L in length, h_0 in depth and u_0 in velocity.

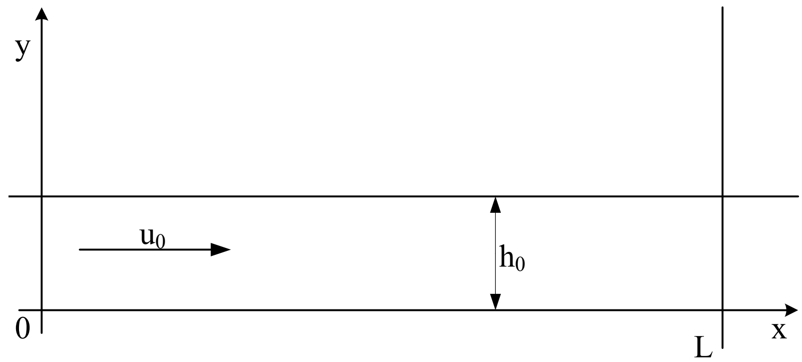

Figure 6.1 Coordinate system and explanation of symbols.

Firstly, the perturbation method is applied to shallow water equations and we develop the expression for the first order and second order perturbation solutions of depth and velocity, when two hydrographs of depth and discharge at upstream end are given.

In the case that both hydrographs of depth and velocity are linear functions of time, it is shown that the hydrograph of depth and velocity at upstream can be reproduced by using the obtained first order perturbation solution of depth, if the hydrograph of depth and the derivative of depth with respect to time at one site are given.

Furthermore, we suggest the possibility that the boundary conditions at upstream can be reproduced by taking nonlinearity in account, i.e. by using second order perturbation solution of depth, when they are quadratic functions of time.

One-dimensional (1-D) shallow flow equations given by Eq. (6.1) and Eq. (6.2) are used as basic equations, which are described below.

$$\frac{\partial h}{\partial t}+\frac{\partial hu}{\partial x}=0 \tag{6.1}$$

$$\frac{\partial u}{\partial t}+u\frac{\partial u}{\partial x}+g\frac{\partial h}{\partial x}=0 \tag{6.2}$$

where x : Cartesian coordinates; u : depth-averaged velocity; h : water depth; t : time; g : gravity acceleration.

By using the following non-dimensional variables with prime, Eqs. (6.1) and (6.2) can be transformed into the linearlized equations, Eqs. (6.3) and (6.4).

$x' = x/h_0$, $u' = u/u_0$, $t' = tu_0/h_0$, $h' = h/h_0$

$$\frac{\partial h'}{\partial t'}+\frac{\partial h'u'}{\partial x'}=0 \tag{6.3}$$

$$\frac{\partial u'}{\partial t'}+u'\frac{\partial u'}{\partial x'}+\frac{1}{Fr_0^2}\frac{\partial h'}{\partial x'}=0 \tag{6.4}$$

where the non-dimensional parameter, Fr_0 are defined as follow:

$$Fr_0=\frac{u_0}{\sqrt{gh_0}}$$

From here, primes indicating non-dimensional variables are omitted for simplicity.

Non-dimensionalized depth and depth-averaged velocity are expanded below by using perturbation method.

$$h=1+\varepsilon h_1+\varepsilon^2 h_2 \tag{6.5}$$

$$u=1+\varepsilon u_1+\varepsilon^2 u_2 \tag{6.6}$$

where the parameter for perturbation ε can be defined as:

$$\varepsilon \equiv \frac{h_0}{L}$$

Substituting Eq. (6.5) and Eq. (6.6) in Eq. (6.3) and Eq. (6.4), we obtained the respective relational expression of ε and ε^2 below.

$$\varepsilon : \quad \frac{\partial h_1}{\partial t}+\frac{\partial h_1}{\partial x}+\frac{\partial u_1}{\partial x}=0 \tag{6.7a}$$

$$\frac{\partial u_1}{\partial t}+\frac{\partial u_1}{\partial x}+\frac{1}{Fr_0{}^2}\frac{\partial h_1}{\partial x}=0 \tag{6.7b}$$

$$\varepsilon^2: \quad \frac{\partial h_2}{\partial t} + \frac{\partial h_2}{\partial x} + \frac{\partial u_2}{\partial x} = -\frac{\partial h_1 u_1}{\partial x} \tag{6.8a}$$

$$\frac{\partial u_2}{\partial t} + \frac{\partial u_2}{\partial x} + u_1 \frac{\partial u_1}{\partial x} + \frac{1}{Fr_0^{\ 2}} \frac{\partial h_2}{\partial x} = 0 \tag{6.8b}$$

By applying the theory of the method of characteristics to Eq. (6. 7), the relational expression on the characteristics line can be obtained.

$$\frac{dx}{dt} = 1 \pm \frac{1}{Fr_0} : \ h_1 \pm Fr_0 u_1 = const. \tag{6.9}$$

There are two areas; Area Ⅰ ～ Ⅱ and Area Ⅱ ～ as shown in Figure 6.2. Area Ⅰ ～ Ⅱ is the area which is influenced by initial condition as represented by M. Area Ⅱ ～ is the area which is influenced only by boundary condition at upstream as represented by N. So we consider respective points of M and N.

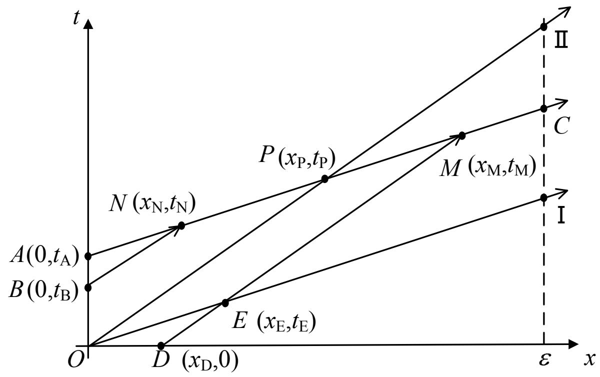

Figure 6.2 Derivation of the perturbation solution based on the method of characteristics.

The first order perturbation solutions of depth and velocity are derived by assuming the boundary conditions as below.

$$h_1 = \alpha_1 t + \alpha_2 t^2 \tag{6.10a}$$

$$u_1 = \beta_1 t + \beta_2 t^2 \tag{6.10b}$$

where, α_1, α_2, β_1, β_2 : coefficients.

Then, using the relations on the characteristics lines of A→M and D→M, u_{1M} and h_{1M} are derived as follow.

$$u_{1M} = \frac{1}{2Fr_0}(\alpha_1 + Fr_0\beta_1)\left(t_M - \frac{x_M}{1+(1/Fr_0)}\right) + \frac{1}{2Fr_0}(\alpha_2 + Fr_0\beta_2)\left(t_M - \frac{x_M}{1+(1/Fr_0)}\right)^2 \tag{6.11a}$$

$$h_{1M} = \frac{1}{2}(\alpha_1 + Fr_0\beta_1)\left(t_M - \frac{x_M}{1+(1/Fr_0)}\right) + \frac{1}{2}(\alpha_2 + Fr_0\beta_2)\left(t_M - \frac{x_M}{1+(1/Fr_0)}\right)^2 \tag{6.11b}$$

Similarly using the relations on the characteristics lines of A→N and B→N, u_{1N} and h_{1N} are derived as below.

$$\begin{aligned} u_{1N} = {} & \frac{1}{2Fr_0}(\alpha_1 + Fr_0\beta_1)\left(t_N - \frac{x_N}{1+(1/Fr_0)}\right) - \frac{1}{2Fr_0}(\alpha_1 - Fr_0\beta_1)\left(t_N - \frac{x_N}{1-(1/Fr_0)}\right) \\ & + \frac{1}{2Fr_0}(\alpha_2 + Fr_0\beta_2)\left(t_M - \frac{x_N}{1+(1/Fr_0)}\right)^2 - \frac{1}{2Fr_0}(\alpha_2 - Fr_0\beta_2)\left(t_M - \frac{x_N}{1-(1/Fr_0)}\right)^2 \end{aligned} \tag{6.12a}$$

$$\begin{aligned} h_{1N} = {} & \frac{1}{2}(\alpha_1 + Fr_0\beta_1)\left(t_N - \frac{x_N}{1+(1/Fr_0)}\right) + \frac{1}{2}(\alpha_1 - Fr_0\beta_1)\left(t_N - \frac{x_N}{1-(1/Fr_0)}\right) \\ & + \frac{1}{2}(\alpha_2 + Fr_0\beta_2)\left(t_N - \frac{x_N}{1+(1/Fr_0)}\right)^2 + \frac{1}{2}(\alpha_2 - Fr_0\beta_2)\left(t_N - \frac{x_N}{1-(1/Fr_0)}\right)^2 \end{aligned} \tag{6.12b}$$

When the boundary conditions are linear functions of time, i.e. $\alpha_2 = 0$ and $\beta_2 = 0$. By substituting respectively Eq. (6.11b) and Eq. (6.12b) in Eq. (6.5), the depth and the derivative of depth with respect to time at M and N are expressed in the following equations.

$$h\big|_M = 1 + \frac{1}{2}\varepsilon(\alpha_1 + Fr_0\beta_1)\left(t_M - \frac{x_M}{1+(1/Fr_0)}\right) \tag{6.13a}$$

$$\left.\frac{\partial h}{\partial t}\right|_M = \frac{1}{2}\varepsilon(\alpha_1 + Fr_0\beta_1) \tag{6.13b}$$

$$h\big|_N = 1 + \frac{1}{2}\varepsilon\left\{(\alpha_1 + Fr_0\beta_1)\left(t_N - \frac{x_N}{1+(1/Fr_0)}\right) + (\alpha_1 - Fr_0\beta_1)\left(t_N - \frac{x_N}{1-(1/Fr_0)}\right)\right\} \tag{6.14a}$$

$$\left.\frac{\partial h}{\partial t}\right|_N = \varepsilon\alpha_1 \tag{6.14b}$$

Eq. (6.13) indicates that even the left hand side is known, α_1 and β_1 can not be obtained. However, Eq. (6.14) indicates that left hand side is known, α_1 and β_1 can be solved. That is to say, two hydrographs can be reproduced, when the hydrograph of depth at one site is given.

But when the boundary conditions are quadratic function of time, both M and N can not be solved as shown by Eq. (6.11) and Eq. (6.12).

Next, we solve Eq. (6.8) and develop the expression for second order perturbation solution of depth and velocity. Each relation of h_2 and of u_2 on the characteristics lines are expressed as below.

$$\begin{aligned}&\frac{D}{Dt}\left(h_2 \pm Fr_0 u_2\right)\\&=\frac{\partial h_2}{\partial t}+\left(1\pm\frac{1}{Fr_0}\right)\frac{\partial h_2}{\partial x}\pm Fr_0\left\{\frac{\partial u_2}{\partial t}+\left(1\pm\frac{1}{Fr_0}\right)\frac{\partial u_2}{\partial x}\right\}=-\frac{\partial h_1 u_1}{\partial x}\mp Fr_0 u_1\frac{\partial u_1}{\partial x}\end{aligned} \tag{6.15}$$

Then, as shown in Figure 6.3, by using the relation expressions on the characteristic lines which are A→M, A’→M’, D→M and D’→M’ and the relation of Δt and Δx.

$$\Delta x_M = \{1+(1/Fr_0)\}\Delta t_A$$

The right hand side of Eq. (6.15) is expressed by u_1 and h_1 at M.

In similar way, as shown by the Figure 6.4, by using the relation expressions on the characteristic lines which are A→N, A’→N’, B→N and B’→N’ and the relation of Δt and Δx.

$$\Delta x_N = \{1+(1/Fr_0)\}\Delta t_A,\quad \Delta x_N = \{1-(1/Fr_0)\}\Delta t_B$$

The right hand side of Eq. (6.15) is expressed by u_1 and h_1 at N.

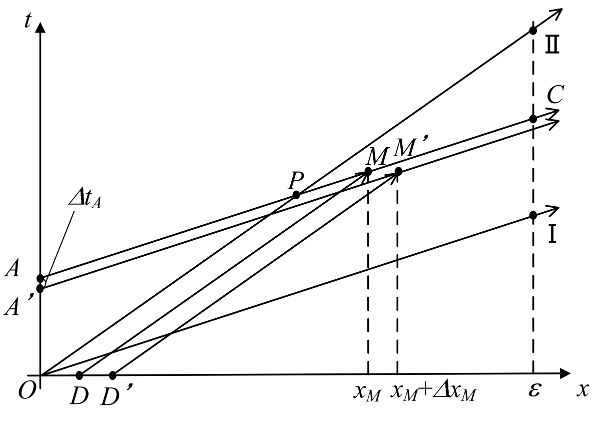

Figure 6.3 Derivation of the 2nd order perturbation solution of point M.

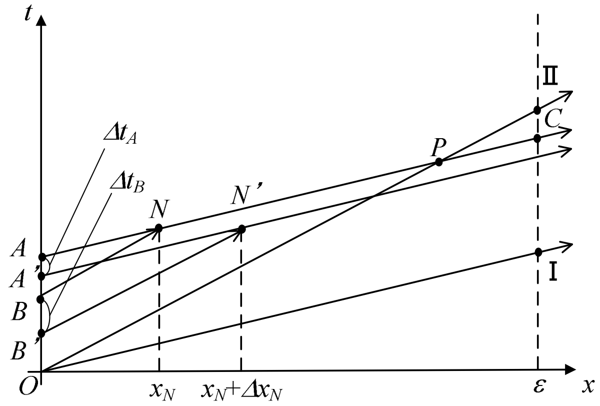

Figure 6.4 Derivation of the 2nd order perturbation solution of point N.

Then, by substituting the first order perturbation solution as noted above into u_1 and h_1 at M, the relation expressions on the characteristic lines which are P→M and D →M are described as below.

$$\frac{D}{Dt}\left(h_2 + Fr_0 u_2\right)_{P\to M} = \frac{3}{4Fr_0 p}\left(2X_2{}^2 t_A^3 + 3X_1 X_2 t_A^2 + X_1{}^2 t_A\right) \tag{6.16a}$$

$$\begin{aligned}\frac{D}{Dt}\left(h_2 - Fr_0 u_2\right)_{D\to M} &= \frac{1}{4}\left(\frac{1}{Fr_0 p}\right)\left[16\left(\frac{1}{Fr_0 p}\right)^3 X_2^2 t^3 + 12\left(\frac{1}{Fr_0 p}\right)^2\left\{X_1 X_2 - 2\left(\frac{x_D}{p}\right)X_2^2\right\}t^2\right.\\ &+ 2\left(\frac{1}{Fr_0 p}\right)\left\{X_1^2 - 6\left(\frac{x_D}{p}\right)X_1 X_2 + 6\left(\frac{x_D}{p}\right)^2 X_2^2\right\}t\\ &\left.+\left\{-\left(\frac{x_D}{p}\right)X_1^2 + 3\left(\frac{x_D}{p}\right)^2 X_1 X_2 - 2\left(\frac{x_D}{p}\right)^3 X_2^2\right\}\right]\end{aligned} \tag{6.16b}$$

In a similar way, respective relational expressions of A→N and B→N are described as below.

$$\frac{D}{Dt}\left(h_2 + Fr_0 u_2\right)_{A\rightarrow N}$$
$$= \frac{1}{4}\left(\frac{1}{Fr_0 p}\right)\Bigg\langle 16\left(\frac{1}{Fr_0 p}\right)^3\left(\frac{p}{q}\right)^4 Y_2^2 t^3$$
$$+\left(\frac{1}{Fr_0 p}\right)^2\left[8\left\{-\left(\frac{p}{q}\right)^2 X_2 Y_2 - 3\left(\frac{p}{q}\right)^4 Y_2^2\right\}t_A\right.$$
$$\left.+4\left\{-\left(\frac{p}{q}\right)^2 X_1 Y_2 - 3\left(\frac{p}{q}\right)^3 Y_1 Y_2\right\}\right]t^2 + \left(\frac{1}{Fr_0 p}\right)\left[12\left\{\left(\frac{p}{q}\right)^2 X_2 Y_2 + \left(\frac{p}{q}\right)^4 Y_2^2\right\}t_A^2\right. \tag{6.17a}$$
$$+4\left\{\left(\frac{p}{q}\right)X_2 Y_1 + 2\left(\frac{p}{q}\right)^2 X_1 Y_2 + 3\left(\frac{p}{q}\right)^3 Y_1 Y_2\right\}t_A$$
$$\left.+2\left\{\left(\frac{p}{q}\right)X_1 Y_1 + \left(\frac{p}{q}\right)^2 Y_1 Y_2\right\}\right]t + \left[2\left\{3X_2^2 - 2\left(\frac{p}{q}\right)^2 X_2 Y_2 - \left(\frac{p}{q}\right)^4 Y_2^2\right\}t_A^3\right.$$
$$+3\left\{X_1 X_2 - \left(\frac{p}{q}\right)X_1 Y_1 - \left(\frac{p}{q}\right)^2 X_1 Y_2 - \left(\frac{p}{q}\right)^3 Y_1 Y_2\right\}t_A^2$$
$$\left.+\left\{3X_1^2 - 2\left(\frac{p}{q}\right)X_1 Y_1 - \left(\frac{p}{q}\right)^2 Y_1^2\right\}t_A\right]\Bigg\rangle$$

$$\frac{D}{Dt}\left(h_2 - Fr_0 u_2\right)_{B\rightarrow N}$$
$$= \frac{1}{4}\left(\frac{1}{Fr_0 p}\right)\Bigg\langle 16\left(\frac{1}{Fr_0 p}\right)^3 X_2^2 t^3 + \left(\frac{1}{Fr_0 p}\right)^2\left[8\left\{3X_2^2 + \left(\frac{p}{q}\right)^2 X_2 Y_2\right\}\frac{q}{p}t_B\right.$$
$$\left.+4\left\{3X_1 X_2 + \left(\frac{p}{q}\right)X_2 Y_1\right\}\right]t^2 + \left(\frac{1}{Fr_0 p}\right)\left[12\left\{X_2^2 + \left(\frac{p}{q}\right)^2 X_2 Y_2\right\}\left(\frac{q}{p}\right)^2 t_B^2\right.$$
$$+4\left\{3X_1 X_2 + 2\left(\frac{p}{q}\right)X_2 Y_1 + \left(\frac{p}{q}\right)^2 X_1 Y_2\right\}\left(\frac{q}{p}\right)t_B + \left\{X_1^2 + \left(\frac{p}{q}\right)X_1 Y_1\right\}t$$
$$+\left[2\left\{X_2^2 + 2\left(\frac{p}{q}\right)^2 X_2 Y_2 - 3\left(\frac{p}{q}\right)^4 Y_2^2\right\}\left(\frac{q}{p}\right)^3 t_B^3\right.$$

$$+3\left\{X_1X_2+\left(\frac{p}{q}\right)X_2Y_1+\left(\frac{p}{q}\right)^2X_1Y_2-3\left(\frac{p}{q}\right)^3Y_1Y_2\right\}\left(\frac{q}{p}\right)^2t_B^2$$
$$+\left\{X_1^2-\left(\frac{p}{q}\right)X_1Y_1-3\left(\frac{p}{q}\right)^2Y_1^2\right\}\left(\frac{q}{p}\right)t_B\Bigg]\Bigg\rangle \quad (6.17b)$$

where, t_A , t_B : time in A and B. X_1, Y_1, X_2, Y_2, p, q are expressed by following equations.

$$X_1=\alpha_1+Fr_0\beta_1,\ Y_1=\alpha_1-Fr_0\beta,\ X_2=\alpha_2+Fr_0\beta_2,\ Y_2=\alpha_2-Fr_0\beta_2$$
$$p=1+(1/Fr_0),\ \ p=1+(1/Fr_0),\ q=1-(1/Fr_0)$$

The right hand side of Eq.(6.16a), Eq.(6.16b), Eq.(6.17a) and Eq.(6.17b) are respectively replaced by following equations.

$$Eq(16a)=\xi_{1,3}t_A^3+\xi_{1,2}t_A^2+\xi_{1,1}t_A \quad (6.18a)$$

$$Eq(16b)=\psi_{4,0}t^3+\psi_{3,0}\,t^2+\psi_{2,0}\,t+\psi_{1,0} \quad (6.18b)$$

$$Eq(17a)=\phi_{4,0}t^3+\left(\phi_{3,1}t_A+\phi_{3,0}\right)t^2$$
$$+\left(\phi_{2,2}t_A^2+\phi_{2,1}t_A+\phi_{2,0}\right)t+\left(\phi_{1,3}t_A^3+\phi_{1,2}t_A^2+\phi_{1,1}t_A\right) \quad (6.18c)$$

$$Eq(17b)=\gamma_{4,0}t^3+\left(\gamma_{3,1}t_B+\gamma_{3,0}\right)t^2$$
$$+\left(\gamma_{2,2}t_B^2+\gamma_{2,1}t_B+\gamma_{2,0}\right)t+\left(\gamma_{1,3}t_B^3+\gamma_{1,2}t_B^2+\gamma_{1,1}t_B\right) \quad (6.18d)$$

The following equation is obtained, integrating Eq. (6.16a) from P to M when t_A is fixed.

$$h_{2M}+Fr_0u_{2M}-h_{2P}-Fr_0u_{2P}=\left(\xi_{1,3}t_A^3+\xi_{1,2}t_A^2+\xi_{1,1}t_A\right)\left(t_M-t_P\right) \quad (6.19a)$$

Similarly Eq. (6.19b) is obtained, integrating Eq. (6.16b) from D to M.

$$h_{2M}-Fr_0u_{2M}=\psi_{1,0}\left(t_M-t_E\right)+\psi_{2,0}\left(\frac{t_M^2}{2}-\frac{t_E^2}{2}\right)+\psi_{3,0}\left(\frac{t_M^3}{3}-\frac{t_E^3}{3}\right)+\psi_{4,0}\left(\frac{t_M^4}{4}-\frac{t_E^4}{4}\right) \quad (6.19b)$$

u_{2P} and h_{2P} are expressed as below by using the relation on the characteristic line from A to P.

$$h_{2P}+Fr_0u_{2P}=\left(\phi_{1,3}t_A^3+\phi_{1,2}t_A^2+\phi_{1,1}t_A\right)\left(t_P-t_A\right)$$
$$+\left(\phi_{2,2}t_A^2+\phi_{2,1}t_A+\phi_{2,0}\right)\left(\frac{t_P^2}{2}-\frac{t_A^2}{2}\right)+\left(\phi_{3,1}t_A+\phi_{3,0}\right)\left(\frac{t_P^3}{3}-\frac{t_A^3}{3}\right)+\phi_{4,0}\left(\frac{t_P^4}{4}-\frac{t_A^4}{4}\right) \tag{6.20}$$

where, t_P is described as follow.

$$t_P=\frac{p}{\left(2/Fr_0\right)}t_A=\frac{p}{\left(2/Fr_0\right)}t_M-\frac{x_M}{\left(2/Fr_0\right)} \tag{6.21}$$

In a similar way, the following equation is obtained, integrating Eq. (6.17a) from A to N when t_A is fixed.

$$h_{2N}+Fr_0u_{2N}=\left(\phi_{1,3}t_A^3+\phi_{1,2}t_A^2+\phi_{1,1}t_A\right)\left(t_N-t_A\right)$$
$$+\left(\phi_{2,2}t_A^2+\phi_{2,1}t_A+\phi_{2,0}\right)\left(\frac{t_N^2}{2}-\frac{t_A^2}{2}\right)+\left(\phi_{3,1}t_A+\phi_{3,0}\right)\left(\frac{t_N^3}{3}-\frac{t_A^3}{3}\right)+\phi_{4,0}\left(\frac{t_N^4}{4}-\frac{t_A^4}{4}\right) \tag{6.22a}$$

Similarly, the following equation is obtained, by integrating Eq. (6.17b) from B to N when t_B is fixed.

$$h_{2N}-Fr_0u_{2N}=\left(\gamma_{1,3}t_B^3+\gamma_{1,2}t_B^2+\gamma_{1,1}t_B\right)\left(t_N-t_B\right)$$
$$+\left(\gamma_{2,2}t_B^2+\gamma_{2,1}t_B+\gamma_{2,0}\right)\left(\frac{t_N^2}{2}-\frac{t_B^2}{2}\right)+\left(\gamma_{3,1}t_B+\gamma_{3,0}\right)\left(\frac{t_N^3}{3}-\frac{t_B^3}{3}\right)+\gamma_{4,0}\left(\frac{t_N^4}{4}-\frac{t_B^4}{4}\right) \tag{6.22b}$$

u_{2_M} and h_{2M} are described the following equations by using the equation which are obtained, substituting respectively Eq. (6.20) and Eq. (6.21) for Eq. (6.19a) and Eq. (6.19b).

$$
\begin{aligned}
&u_{2M} \\
&= \frac{1}{2Fr_0}\left\langle \left[\frac{1}{4}\left\{\left(\frac{p}{2/Fr_0}\right)^4 - 1\right\}\phi_{4,0} + \frac{1}{3}\left\{\left(\frac{p}{2/Fr_0}\right)^3 - 1\right\}\phi_{3,1} \right.\right. \\
&+ \frac{1}{2}\left\{\left(\frac{p}{2/Fr_0}\right)^2 - 1\right\}\phi_{2,2} + \left\{\left(\frac{p}{2/Fr_0}\right) - 1\right\}\phi_{1,3} \\
&\qquad\qquad\qquad\qquad \left. - \frac{1}{4}\left(\frac{p}{2/Fr_0}\right)^4 \psi_{4,0} \right] t_A^4 \\
&+ \left[\frac{1}{3}\left\{\left(\frac{p}{2/Fr_0}\right)^3 - 1\right\}\phi_{3,0} + \frac{1}{2}\left\{\left(\frac{p}{2/Fr_0}\right)^2 - 1\right\}\phi_{2,1} \right. \\
&+ \left\{\left(\frac{p}{2/Fr_0}\right) - 1\right\}\phi_{1,2} + \left(\frac{x_D}{2/Fr_0}\right)\xi_{1,3} \\
&\qquad \left. - \frac{1}{3}\left(\frac{p}{2/Fr_0}\right)^3 \psi_{3,0} - \left(\frac{p}{2/Fr_0}\right)^3 \left(\frac{x_D}{2/Fr_0}\right)\psi_{4,0} \right] t_A^3 \\
&+ \left[\frac{1}{2}\left\{\left(\frac{p}{2/Fr_0}\right)^2 - 1\right\}\phi_{2,0} + \left\{\left(\frac{p}{2/Fr_0}\right) - 1\right\}\phi_{1,1} \right. \\
&+ \left(\frac{x_D}{2/Fr_0}\right)\xi_{1,2} - \frac{1}{2}\left(\frac{p}{2/Fr_0}\right)^2 \psi_{2,0} \\
&\left. - \left(\frac{p}{2/Fr_0}\right)^2 \left(\frac{x_D}{2/Fr_0}\right)\psi_{3,0} - \frac{3}{2}\left(\frac{p}{2/Fr_0}\right)^2 \left(\frac{x_D}{2/Fr_0}\right)^2 \psi_{4,0} \right] t_A^2 \\
&+ \left[\left(\frac{x_D}{2/Fr_0}\right)\xi_{1,1} - \left(\frac{p}{2/Fr_0}\right)\psi_{1,0} - \left(\frac{p}{2/Fr_0}\right)\left(\frac{x_D}{2/Fr_0}\right)\psi_{2,0} \right. \\
&\left.\left. - \left(\frac{p}{2/Fr_0}\right)\left(\frac{x_D}{2/Fr_0}\right)^2 \psi_{3,0} - \left(\frac{p}{2/Fr_0}\right)\left(\frac{x_D}{2/Fr_0}\right)^3 \psi_{4,0} \right] t_A \right\rangle
\end{aligned}
\qquad (6.23a)
$$

$$
\begin{aligned}
&h_{2M} \\
&= \frac{1}{2}\Bigg\langle \Bigg[\frac{1}{4}\left\{\left(\frac{p}{2/Fr_0}\right)^4 - 1\right\}\phi_{4,0} + \frac{1}{3}\left\{\left(\frac{p}{2/Fr_0}\right)^3 - 1\right\}\phi_{3,1} \\
&+ \frac{1}{2}\left\{\left(\frac{p}{2/Fr_0}\right)^2 - 1\right\}\phi_{2,2} + \left\{\left(\frac{p}{2/Fr_0}\right) - 1\right\}\phi_{1,3} \\
&\qquad\qquad\qquad\qquad + \frac{1}{4}\left(\frac{p}{2/Fr_0}\right)^4 \psi_{4,0} \Bigg] t_A^4 \\
&+ \Bigg[\frac{1}{3}\left\{\left(\frac{p}{2/Fr_0}\right)^3 - 1\right\}\phi_{3,0} + \frac{1}{2}\left\{\left(\frac{p}{2/Fr_0}\right)^2 - 1\right\}\phi_{2,1} \\
&+ \left\{\left(\frac{p}{2/Fr_0}\right) - 1\right\}\phi_{1,2} + \left(\frac{x_D}{2/Fr_0}\right)\xi_{1,3} \\
&\qquad + \frac{1}{3}\left(\frac{p}{2/Fr_0}\right)^3 \psi_{3,0} + \left(\frac{p}{2/Fr_0}\right)^3 \left(\frac{x_D}{2/Fr_0}\right)\psi_{4,0} \Bigg] t_A^3 \\
&+ \Bigg[\frac{1}{2}\left\{\left(\frac{p}{2/Fr_0}\right)^2 - 1\right\}\phi_{2,0} + \left\{\left(\frac{p}{2/Fr_0}\right) - 1\right\}\phi_{1,1} \\
&+ \left(\frac{x_D}{2/Fr_0}\right)\xi_{1,2} + \frac{1}{2}\left(\frac{p}{2/Fr_0}\right)^2 \psi_{2,0} \\
&+ \left(\frac{p}{2/Fr_0}\right)^2 \left(\frac{x_D}{2/Fr_0}\right)\psi_{3,0} + \frac{3}{2}\left(\frac{p}{2/Fr_0}\right)^2 \left(\frac{x_D}{2/Fr_0}\right)^2 \psi_{4,0} \Bigg] t_A^2 \\
&+ \Bigg[\left(\frac{x_D}{2/Fr_0}\right)\xi_{1,1} + \left(\frac{p}{2/Fr_0}\right)\psi_{1,0} + \left(\frac{p}{2/Fr_0}\right)\left(\frac{x_D}{2/Fr_0}\right)\psi_{2,0} \\
&+ \left(\frac{p}{2/Fr_0}\right)\left(\frac{x_D}{2/Fr_0}\right)^2 \psi_{3,0} + \left(\frac{p}{2/Fr_0}\right)\left(\frac{x_D}{2/Fr_0}\right)^3 \psi_{4,0} \Bigg] t_A \Bigg\rangle
\end{aligned}
\tag{6.23b}
$$

where, t_A is expressed by t_M as below.

$$
t_A = \frac{2/Fr_0}{p} t_M - \frac{x_D}{p} \tag{6.24}
$$

In a similar way, from Eq. (6.22a) and Eq. (6.22b), u_{2_N} and h_{2N} are described as below.

$$
\begin{aligned}
&u_{2N}\\
&=\frac{1}{2Fr_0}\Bigg[\frac{x_N}{p}\left(\phi_{1,3}+\phi_{2,2}+\phi_{3,1}+\phi_{4,0}\right)t_A^3\\
&\qquad-\frac{x_N}{q}\left(\gamma_{1,3}+\gamma_{2,2}+\gamma_{3,1}+\gamma_{4,0}\right)t_B^3\\
&+\frac{x_N}{p}\left(\phi_{1,2}+\phi_{2,1}+\phi_{3,0}+\frac{1}{2}\frac{x_N}{p}\phi_{2,2}+\frac{x_N}{p}\phi_{3,1}+\frac{3}{2}\frac{x_N}{p}\phi_{4,0}\right)t_A^2\\
&-\frac{x_N}{q}\left(\gamma_{1,2}+\gamma_{2,1}+\gamma_{3,0}+\frac{1}{2}\frac{x_N}{q}\gamma_{2,2}+\frac{x_N}{q}\gamma_{3,1}+\frac{3}{2}\frac{x_N}{q}\gamma_{4,0}\right)t_B^2\\
&+\frac{x_N}{p}\Bigg\{\phi_{1,1}+\phi_{2,0}+\frac{1}{2}\frac{x_N}{p}\phi_{2,1}\\
&\qquad\qquad+\frac{x_N}{p}\phi_{3,0}+\frac{1}{3}\left(\frac{x_N}{p}\right)^2\phi_{3,1}+\left(\frac{x_N}{p}\right)^2\phi_{4,0}\Bigg\}t_A\\
&-\frac{x_N}{q}\Bigg\{\gamma_{1,1}+\gamma_{2,0}+\frac{1}{2}\frac{x_N}{q}\gamma_{2,1}\\
&\qquad\qquad+\frac{x_N}{q}\gamma_{3,0}+\frac{1}{3}\left(\frac{x_N}{q}\right)^2\gamma_{3,1}+\left(\frac{x_N}{q}\right)^2\gamma_{4,0}\Bigg\}t_B\\
&+\left\{\frac{1}{2}\left(\frac{x_N}{p}\right)^2\phi_{2,0}+\frac{1}{3}\left(\frac{x_N}{p}\right)^3\phi_{3,0}+\frac{1}{4}\left(\frac{x_N}{p}\right)^4\phi_{4,0}\right\}\\
&-\left\{\frac{1}{2}\left(\frac{x_N}{q}\right)^2\gamma_{2,0}+\frac{1}{3}\left(\frac{x_N}{q}\right)^3\gamma_{3,0}+\frac{1}{4}\left(\frac{x_N}{q}\right)^4\gamma_{4,0}\right\}\Bigg]
\end{aligned}
\tag{6.25a}
$$

$$
\begin{aligned}
&h_{2N} \\
&= \frac{1}{2}\left[\frac{x_N}{p}\left(\phi_{1,3} + \phi_{2,2} + \phi_{3,1} + \phi_{4,0}\right)t_A^3 \right. \\
&\qquad + \frac{x_N}{q}\left(\gamma_{1,3} + \gamma_{2,2} + \gamma_{3,1} + \gamma_{4,0}\right)t_B^3 \\
&+ \frac{x_N}{p}\left(\phi_{1,2} + \phi_{2,1} + \phi_{3,0} + \frac{1}{2}\frac{x_N}{p}\phi_{2,2} + \frac{x_N}{p}\phi_{3,1} + \frac{3}{2}\frac{x_N}{p}\phi_{4,0} \right)t_A^2 \\
&+ \frac{x_N}{q}\left(\gamma_{1,2} + \gamma_{2,1} + \gamma_{3,0} + \frac{1}{2}\frac{x_N}{q}\gamma_{2,2} + \frac{x_N}{q}\gamma_{3,1} + \frac{3}{2}\frac{x_N}{q}\gamma_{4,0} \right)t_B^2 \\
&+ \frac{x_N}{p}\left\{ \phi_{1,1} + \phi_{2,0} + \frac{1}{2}\frac{x_N}{p}\phi_{2,1} \right. \\
&\qquad\qquad \left. + \frac{x_N}{p}\phi_{3,0} + \frac{1}{3}\left(\frac{x_N}{p}\right)^2\phi_{3,1} + \left(\frac{x_N}{p}\right)^2\phi_{4,0} \right\}t_A \\
&+ \frac{x_N}{q}\left\{ \gamma_{1,1} + \gamma_{2,0} + \frac{1}{2}\frac{x_N}{q}\gamma_{2,1} \right. \\
&\qquad\qquad \left. + \frac{x_N}{q}\gamma_{3,0} + \frac{1}{3}\left(\frac{x_N}{q}\right)^2\gamma_{3,1} + \left(\frac{x_N}{q}\right)^2\gamma_{4,0} \right\}t_B \\
&+ \left\{ \frac{1}{2}\left(\frac{x_N}{p}\right)^2\phi_{2,0} + \frac{1}{3}\left(\frac{x_N}{p}\right)^3\phi_{3,0} + \frac{1}{4}\left(\frac{x_N}{p}\right)^4\phi_{4,0} \right\} \\
&\left. + \left\{ \frac{1}{2}\left(\frac{x_N}{q}\right)^2\gamma_{2,0} + \frac{1}{3}\left(\frac{x_N}{q}\right)^3\gamma_{3,0} + \frac{1}{4}\left(\frac{x_N}{q}\right)^4\gamma_{4,0} \right\} \right]
\end{aligned}
\tag{6.25b}
$$

where t_A and t_B are expressed by t_N as below.

$$
t_A = t_N - \frac{x_N}{1+\left(1/Fr_0\right)}, \quad t_B = t_N - \frac{x_N}{1-\left(1/Fr_0\right)} \tag{6.26}
$$

As shown by Eq. (6.23b) and Eq. (6.25b), second order perturbation solutions of depth are respectively described by the third order expression of time at N and by the fourth order expression of time at M. By substituting the first order and second order perturbation solutions of depth into Eq. (6.5), depth, first order, second order and third order derivatives of depth with respect to time are obtained at each point. Those obtained equations are related with four different types. Hence, when the hydrograph of depth at one site is known, i.e. depth, first order, second order and third order derivatives of depth with respect to time are known, four coefficients are obtained by these values and those obtained equations. That is to say, this indicates a potential of one hydrograph at one site enables boundary conditions to be reproduced by nonlinearity taken in account, when the boundary conditions are quadric functions of time.

6.3 Summary

This chapter is concerned with the reproduction of flash floods with a high Froude number. The possibility of reproducing such flows by using one depth hydrograph at one site is considered. The main findings of this study are listed as follows.

1. The boundary conditions at upstream can be reproduced by using only first order perturbation solution of depth which is obtained by applying the perturbation method, when they are linear functions of time. But they cannot be reproduced incase of quadratic functions of time.

2. The boundary conditions at upstream can be reproduced by taking nonlinearity in account, i.e. by using second order perturbation solution of depth, when they are quadratic functions of time.

In this chapter, we analyzed theoretically the possibility of reproducing flash floods with high Froude number in a horizontal flat channel, as a first step in this issue. Conducting numerical processes including bed slope and bed shear stress will be the next step. We believed that, getting good results from the numerical simulations will be very helpful for prediction of floods with high velocity and steep slopes, if the discharge and depth hydrograph are identified at the upstream end.

Chapter 7

NUMERICAL MODELING OF UNSTEADY FLOW AROUND A BOX CULVERT AND ITS VERIFICATION

7.1 Preliminaries

This chapter deals with a numerical model to simulate flow through a box culvert, which represents flow during flash floods under highways in Oman. We firstly show the typical flow patterns with the transition from free surface flows to pressurized flows and overflows over a culvert, based on hydraulic experiments. Then, a numerical model applicable to the full/partial full pressurized flows is tested to simulate the typical flow patterns under the conditions of experiments.

It is pointed out that although the numerical model used here can simulate the simple flow patterns to some extents, the model should be improved further to get better results.

Oman is one of the arid countries subjected to flash floods. Records show that major flash floods occurred in Oman in 1989, 1997, 2002, 2003, 2005, 2007 and 2010. Such floods run in wadies “valleys or dry rivers incised in the mountains and remain dry except during infrequent heavy rains” are poorly understood. Commonly, wadi basins are suffering from drought conditions all year except during and after a rainstorm as shown in Figure (7.1). They are affected by infrequent rainfall events in a short period of time. Depending on the intensity of rainfall, flow can be in the form of flash flood, if the rainfall is heavy. If the intensity of rainfall is low, surface flow will be consequently low.

The materials of the wadi-bed are varies from region to region depending on the topography. Near the mountains, the bed consists of stone and gravel with high slope, which makes the flow runs with high velocity and low transmission loss. On the other hand, sands with scarce vegetations and low slope are the major characteristics of the wadi-beds in the desert areas. The main wadi channel near the mountain areas far way from the cities has a width over 100 m (it can reach to around 400 m in the major wadies). However, due to the rapid increase in the population that lives in the major cities and the urbanizations beside the channels, the width is decreased to about less than half its original width.

The literature has shown that the modeling in flash floods in arid regions is inadequate for prediction, mitigation or management. Therefore, numerical models are useful tools to improve flash floods prediction by providing better understanding of the hydrological processes governing flash floods in arid regions.

A culvert is a covered channel of relatively short length designed to pass water through an embankment (e.g. highway and railroad) (Chanson, 2000). They are very common, often being constructed to allow rivers to pass under highways or railway embankment. Flow through culverts is controlled by many factors such as size, roughness, slope, inlet geometry, and tailwater conditions. Variety of flow types could take place through culverts. It can be full or partly-full. In order to determine the exact type of flow, laboratory or field investigations are needed.

Due to its proximity to the commercial and business district of Muscat City, the Capital of Oman, wadies intersect with a number of streets, where culverts and bridges have been constructed to provide road flood protection. Culverts were very common used to allow water to pass under highways as shown in Figure 7.2. They had also been used to carry watercourses under built-up areas. In many cases the city is flooded because the culverts capacity was insufficient to carry large flood flows. Figure 7.3 shows water flow through box culverts during flood seasons.

(a) Dry wadi channel

(b) Wadi channel in full flow

Figure 7.1 Flash flood in a wadi channel.

Figure 7.2 A box culverts constructed under a highway in Muscat City.

Figure 7.3 Flow through culverts during flood seasons.

In this study, we analyzed the typical features of flow through and over culverts by fundamental hydraulic experiments and a numerical model, considering the interaction between free surface flow and pressurized flow. The numerical model is verified by carrying out hydraulic experiments.

It was shown that the hydraulic transients of the interaction between open channel flow and pressurized pipe flow inside the culvert could be produced by using a numerical model.

7.2 Hydraulic Experiments

The hydraulic experiments were conducted using a horizontal rectangular flume 140 cm long, 50 cm wide and 30 cm high as shown in Figure 7.4. The flume is equipped with a tailgate to control the tailwater depth. In order to generate submerged flow over the culvert, the width of the flume is reduced in Run 3 and Run 4 to be equal to the width of the culvert. Above the culvert, in Run 1 and Run 2, there is an embankment to prevent overflow. On the other hand, this embankment is removed in Run 3 and Run 4 to let overflow to take place.

Constant discharge is supplied at the upstream end (inlet) into the dry bed flume. After sometime, the unsteady flow reaches the steady state. The hydraulic variables in the steady sate are listed in Table 7.1.

Figure 7.5 shows the typical flow patterns appeared in the steady state adjusting the height of the tailgate. These flow patterns are summarized as follows:

(a) Run 1: Partly-full pipe flow (submerged outlet only, without overflow).
(b) Run 2: Classic full pipe flow (submerged inlet and outlet, without overflow).
(c) Run 3: Free surface open channel flow (submerged inlet only, with overflow).
(d) Run 4: Partly-full pipe flow (submerged inlet and outlet, with overflow).

The water surface profiles in the steady state along the centerline are shown in Figure 7.6. Different types of flow through culverts are taken places depending on the outlets and inlets conditions.

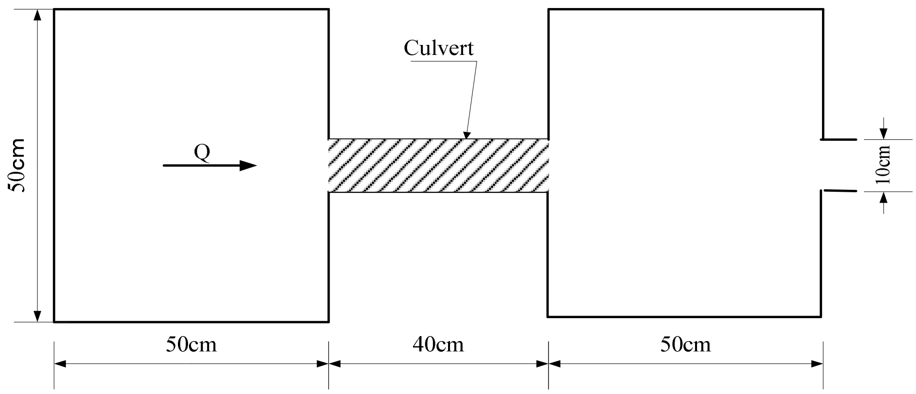

(a) Run 1 and Run 2

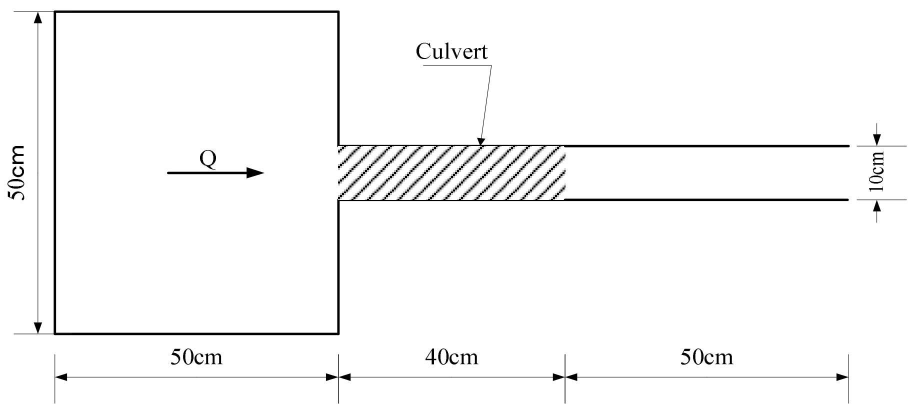

(b) Run 3 and Run 4

Figure 7.4 Schematic illustration of experimental setup.

Table 7.1 Laboratory tests variables.

Run	**Q (cm^3/s)**	**B (cm)**	**B_c (cm)**	**L_c (cm)**	**H_c (cm)**	**$h_{u/s}$ (cm)**	**$h_{d/s}$ (cm)**	**S_0**
1	465.6	50	10	40	3.2	2.04	3.44	1/443
2	465.5	50	10	40	3.2	5.15	6.25	1/443
3	1946	50	10	40	3.2	5.05	2.61	1/26
4	1232	50	10	40	3.2	5.82	5.91	1/271

where Q = flow rate; B = Width of channel; B_c = Width of culvert; L_c = Length of culvert; H_c= Height of culvert; $h_{u/s}$= Water depth upstream culvert; $h_{d/s}$ = Water depth downstream culvert; S_0 = Slope.

The outlet is submerged in Run 1 as shown in Figure 7.5(a) and Figure 7.6(a), which generate the transition from free surface flow to pressurized flow in the barrel of the culvert.

A type of outlet control occurred in Run (2) as shown in Figure 7.5(b) and Figure 7.6(b), in which fully-pressurized flow occurs through the barrel of the culvert. The full-pressurized flow was caused by increasing the tailwater depth, which let backwater to take place. The flow changed gradually from open channel flow to pressurized pipe flow as shown in Figure 7.7.

Over flow was observed in Run 3 and Run 4 as shown in Figure 7.5(c) and Figure 7.5(d), respectively. In Run 3 with submerged inlet, the flow with free stream line is observed inside the culvert. In this case, both flows through and over the culvert are free water surface flows. A clear type of outlet control is shown in Figure 7.5(d) and Figure 7.6(d) where both inlet and outlet are submerged. It occurred by increasing the outlet depth. The transition from free surface flow to pressurized flow occurs through hydraulic jump in the culvert.

(a)

(b)

(c)

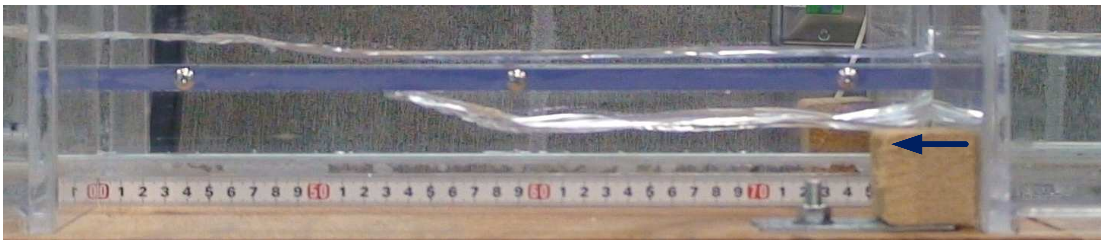

(d)

Figure 7.5 Flow profiles during experiments for (a) Run 1, (b) Run 2, (c) Run 3 and (d) Run 4.

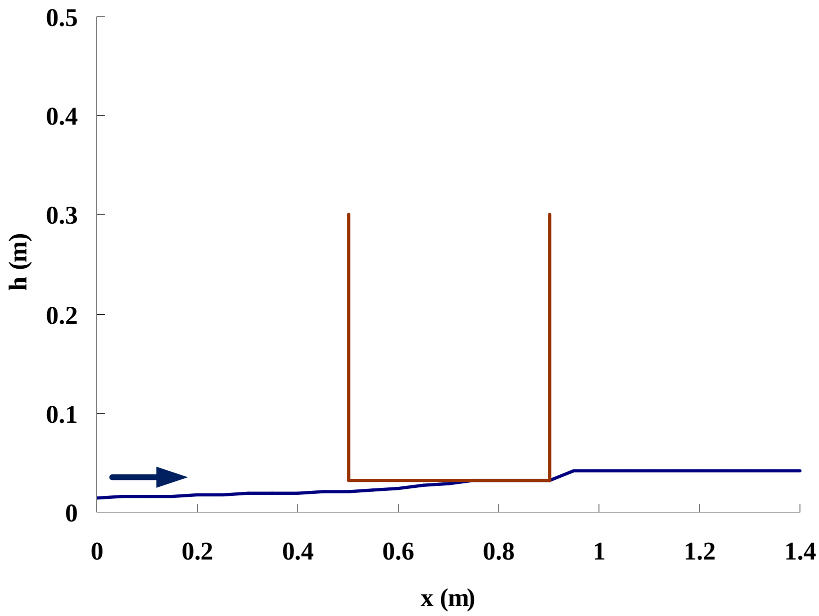
0.5
0.4
0.3
0.2
0.1
0
h (m)
0
0.2
0.4
0.6
0.8
1
1.2
1.4
x (m)

(a)

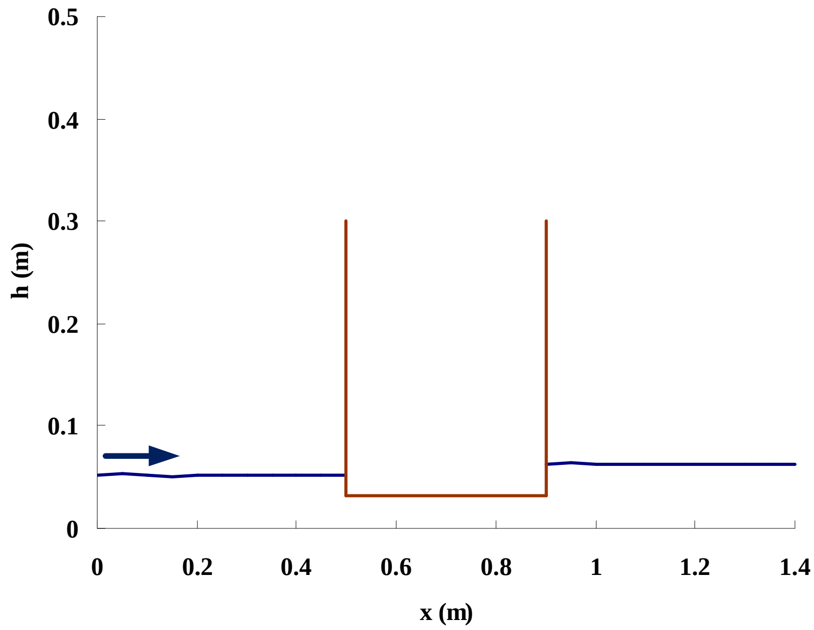
0.5
0.4
0.3
0.2
0.1
0
h (m)
0
0.2
0.4
0.6
0.8
1
1.2
1.4
x (m)

(b)

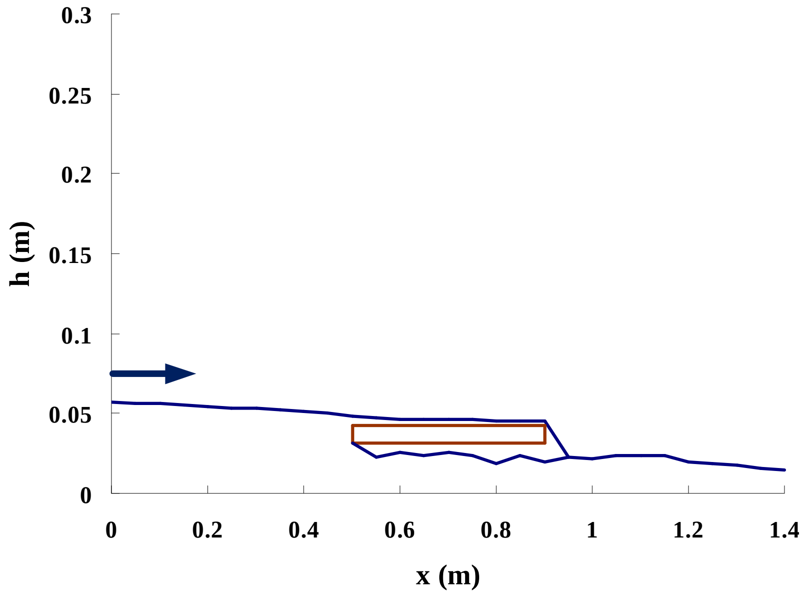

(c)

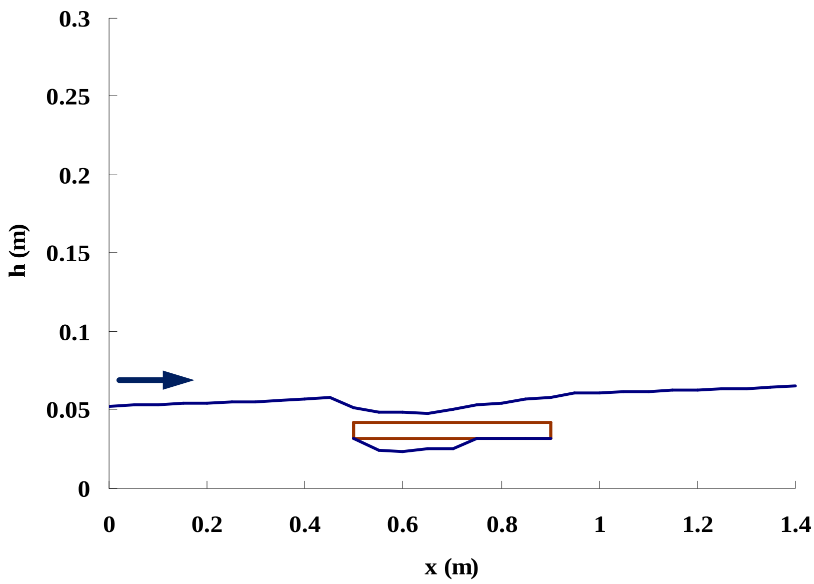

(d)

Figure 7.6 Surface water variations along centerline for experiments: (a) Run 1, (b) Run 2, (c) Run 3 and (d) Run 4.

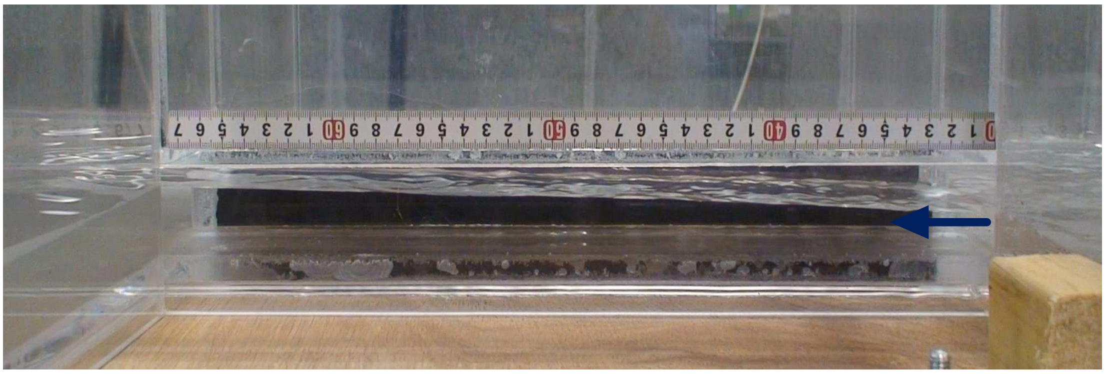

(a) Open channel flow

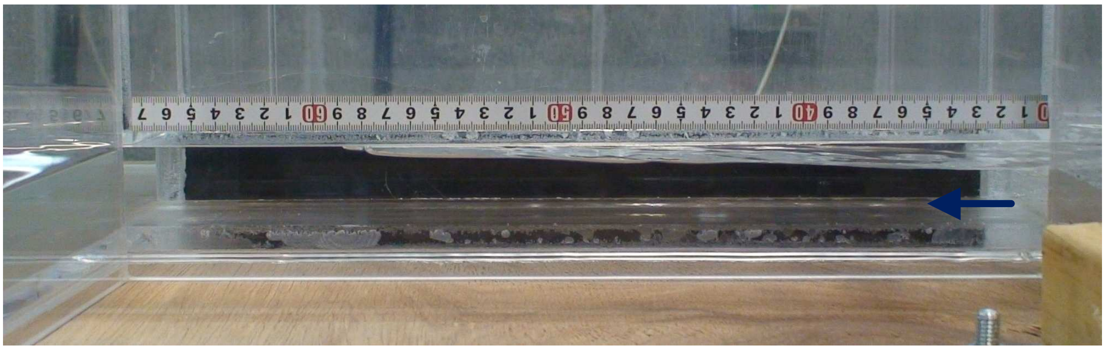

(b) Partial-pressurized flow

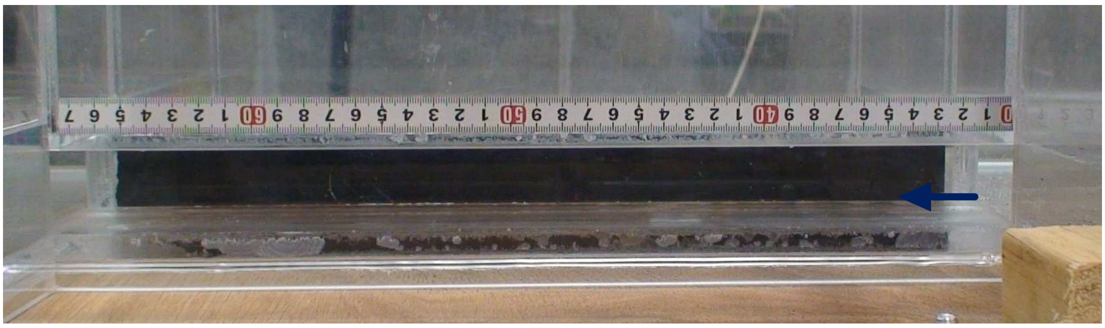

(c) Full-pressurized flow

Figure 7.7 The gradual changes of flow in Run2.

7.3 Numerical Model

The numerical simulations of the hydraulic experiments mentioned above were carried out by using a numerical model developed by Hosoda et al. (1993), which can be used to reproduce the transition from free surface flow to pressurized flow in a plane 2-D system.

The numerical model is composed of the continuity and momentum equations of the plane two-dimensional flows of open channel flows and pressurized pipe flows and the momentum equation of an interface between both flows. The fundamental equations are given as follows:

[Free surface open channel flow]

$$\frac{\partial h}{\partial t}+\frac{\partial M}{\partial x}+\frac{\partial N}{\partial y}=0 \tag{7.1}$$

$$\frac{\partial M}{\partial t}+\frac{\partial UM}{\partial x}+\frac{\partial VM}{\partial y}=-gh\frac{\partial (h+z_b)}{\partial x}-\frac{\tau_{b_x}}{\rho} \tag{7.2}$$

$$\frac{\partial N}{\partial t}+\frac{\partial UN}{\partial x}+\frac{\partial VN}{\partial y}=-gh\frac{\partial (h+z_b)}{\partial y}-\frac{\tau_{b_y}}{\rho} \tag{7.3}$$

[Pressurized pipe flow]

$$\frac{\partial UD}{\partial x}+\frac{\partial VD}{\partial y}=0 \tag{7.4}$$

$$\frac{\partial UD}{\partial t}+\frac{\partial DU^2}{\partial x}+\frac{\partial DUV}{\partial y}=-\frac{D}{\rho}\frac{\partial P_D}{\partial x}-gD\frac{\partial (D+z_b)}{\partial x}-2\frac{\tau_{b_x}}{\rho} \tag{7.5}$$

$$\frac{\partial VD}{\partial t}+\frac{\partial DUV}{\partial x}+\frac{\partial DV^2}{\partial y}=-\frac{D}{\rho}\frac{\partial P_D}{\partial y}-gD\frac{\partial (D+z_b)}{\partial y}-2\frac{\tau_{b_y}}{\rho} \tag{7.6}$$

where h :depth, (U,V) :depth-averaged velocity, (M,N) :discharge flux vector defined as $M\equiv Uh, N\equiv Vh$, D :diameter, P :pressure at a top of pipe, (τ_{b_x},τ_{b_y}) :wall shear stress vectors.

Following the procedure of numerical simulation described in literature (Hosoda et al., 1993), the flow area is divided into three parts: free surface open channel flow, pressurized pipe flow, and the interface of both flows as shown in Figure 7.8. The arrangement of hydraulic variables to apply finite volume method is demonstrated in Figure 7.9.

For the free surface open channel flow region, the common method (Inoue, 1986) of flood invasion analysis in flood plains is used for the time integral of Eq. (7.1) ~ (7.3). The overflow from box culvert is considered as free surface open channel flow, considering the unit discharge at the junction between the channel and the culvert using the weir formula, the critical flow conditions, etc. Eq. (7.4) ~ (7.6) are applied to the pressurized flow region to calculate velocities and pressure. The common numerical method to calculate incompressible fluids is used for this region with the interaction procedures of pressure calculation in SMAC method (Hirt and Cook, 1972). The side view along the x-axis in Figure 7.8 is shown in Figure 7.10. The momentum equation at the interface is derived as Eq. (7.7) by integrating Eq. (7.2) and (7.5) from $x_{i-1/2}$ to $x_{i+1/2}$.

$$\begin{aligned}
&\frac{M^{n+1}_{i,j+1/2} - M^{n}_{i,j+1/2}}{\Delta t}\Delta x + (UM)_{i+1/2,\,j+1/2} - (UM)_{i-1/2,\,j+1/2} \\
&+ \frac{(VM)_{i,j+1} - (VM)_{i,j}}{\Delta y}\Delta x = \\
&- g(\frac{h^2}{2})_{i+1/2,\,j+1/2} + (D\frac{P_D}{\rho} + \frac{gD^2}{2})_{i-1/2,\,j+1/2} - gD(z_{b_{i+1/2,\,j+1/2}} - z_{b_{i-1/2,\,j+1/2}}) - (\frac{\tau_{b_x}}{\rho})_i \frac{3\Delta x}{2}
\end{aligned} \tag{7.7}$$

The common flood invasion analysis mentioned above is firstly applied to reproduce the flow in the steady state from the initial dry bed flume under the experimental conditions.

The constant discharge is given as the inlet boundary condition, and the discharge at the outlet is calculated using the relation between depth and discharge at the tailgate (outlet).

Since transition from free surface flow to pressurized flow occurs inside the culvert by the increase of downstream depth, it is necessary to apply the procedures of interface tracking as follows:

The position of an interface and the depth h at $t=(n-1/2)\Delta t$ and M, N at $t=n\Delta t$ are known. The depth h at $t=(n+1/2)\Delta t$ of both the free surface region and the control volume bordering an interface (Figure 7.8) is calculated by Eq. (7.1). If $h^{n+1/2}$ of the free surface region is greater than D, the control volume is regarded as the volume of the pressurized flow region. If $h^{n+1/2}$ of the volume bordering an interface is smaller than D, the volume becomes the free surface region and the new position of an interface is determined.

Incase that the inlet of culvert is submerged as in Run 3 and Run 4, a model of free surface flow or pressurized flow is selected properly according to the situation of the cell at the inlet of the culvert.

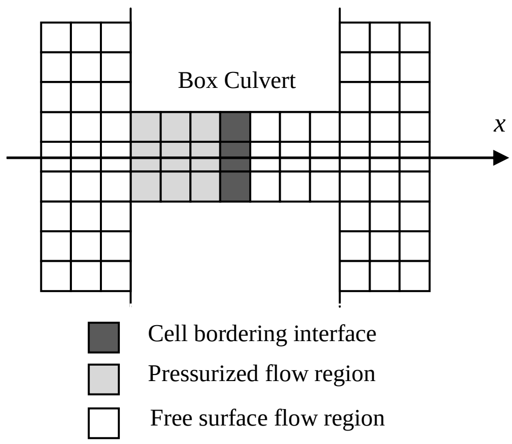

Figure 7.8 Classification of flow domain.

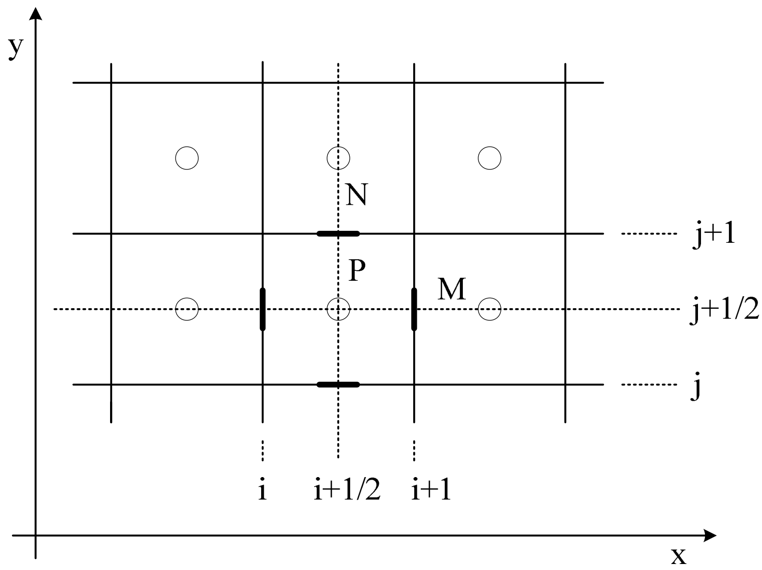

Figure 7.9 Arrangement of hydraulic variables.

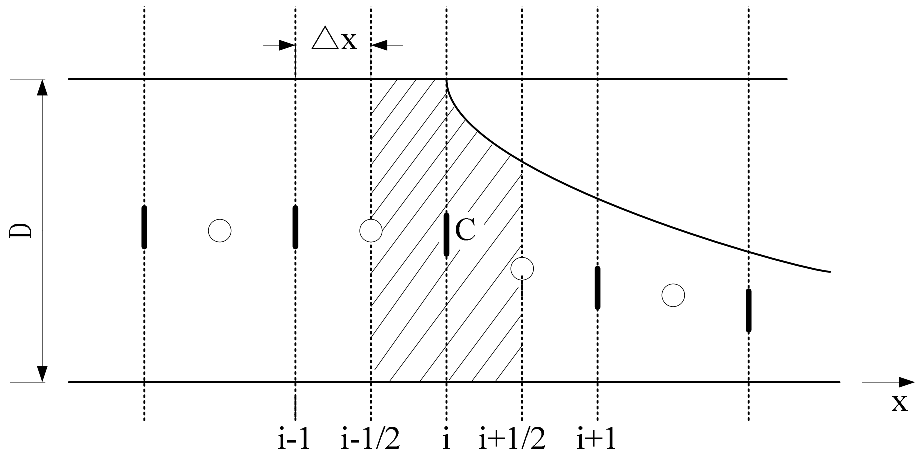

Figure 7.10 Side view along x-axis.

7.4 Verification of Results

The fundamental two-dimensional simulation model is applied under the experimental conditions. Figure 7.11 shows the water depths variations at the centerline after the calculated flow results reach the steady state.

There is a good agreement between the experimental and the numerical results especially in Run 1 and Run 2 as shown in Figure 7.11(a) and Figure 7.11(b). In Run 3 and Run 4, where overflow and air-cavity occurred, the calculated results for the flow through culverts are not matching with observed flow, as shown in Figure 7.11(c) and Figure 7.11(d). These are because the model assuming hydrostatics pressure is not applicable to rapid varied flows with air-cavity inside the culvert.

Using calculated results for Run 1 and Run 2, which include a partially-pressurized flow or fully-pressurized flow in the culvert, respectively, we showed the temporal transition processes from free surface flow to pressurized flow in Figure 7.12 and Figure 7.13. Although we can’t compare the calculated results with the experimental ones, the simulation model can reproduce the transition process reasonably for both cases.

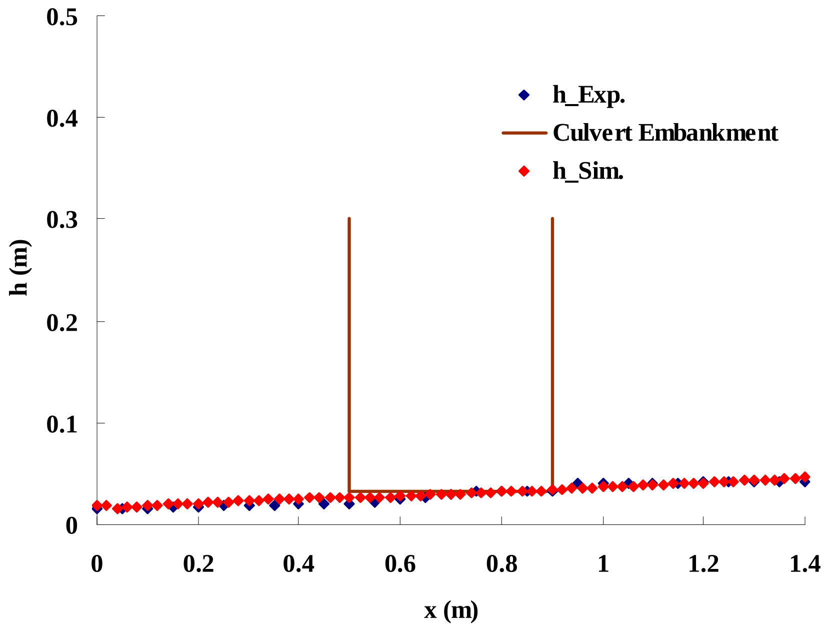
0.5
0.4
0.3
0.2
0.1
0
h (m)
h_Exp.
Culvert Embankment
h_Sim.
0
0.2
0.4
0.6
0.8
1
1.2
1.4
x (m)

(a) Run 1

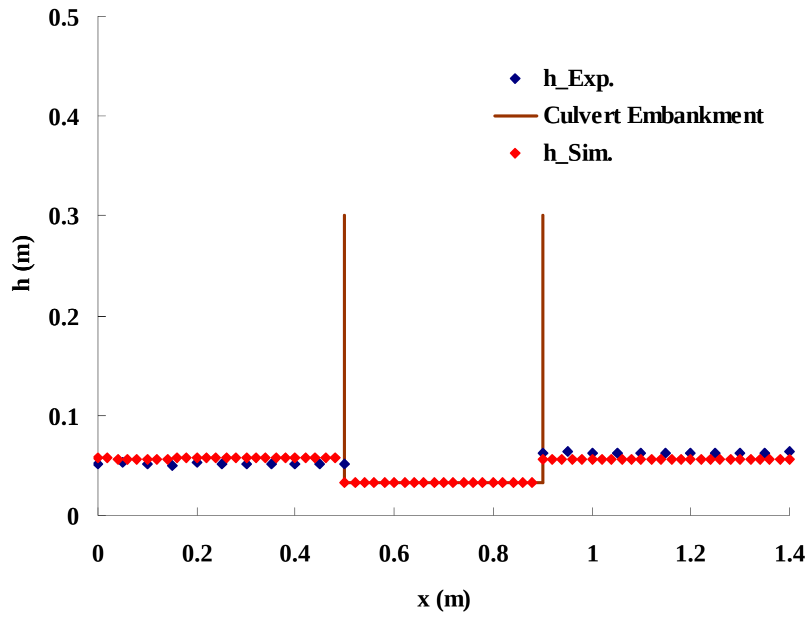
0.5
0.4
0.3
0.2
0.1
0
h (m)
h_Exp.
Culvert Embankment
h_Sim.
0
0.2
0.4
0.6
0.8
1
1.2
1.4
x (m)

(b) Run 2

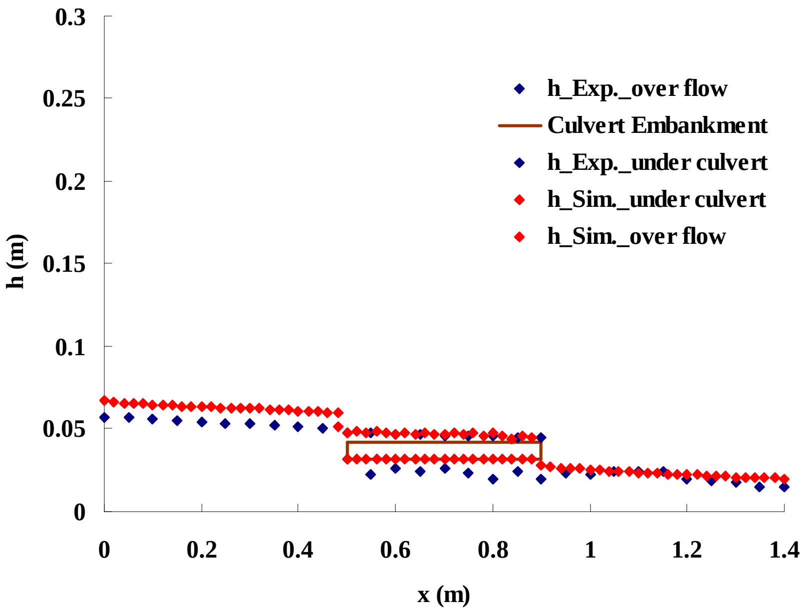

(c) Run 3

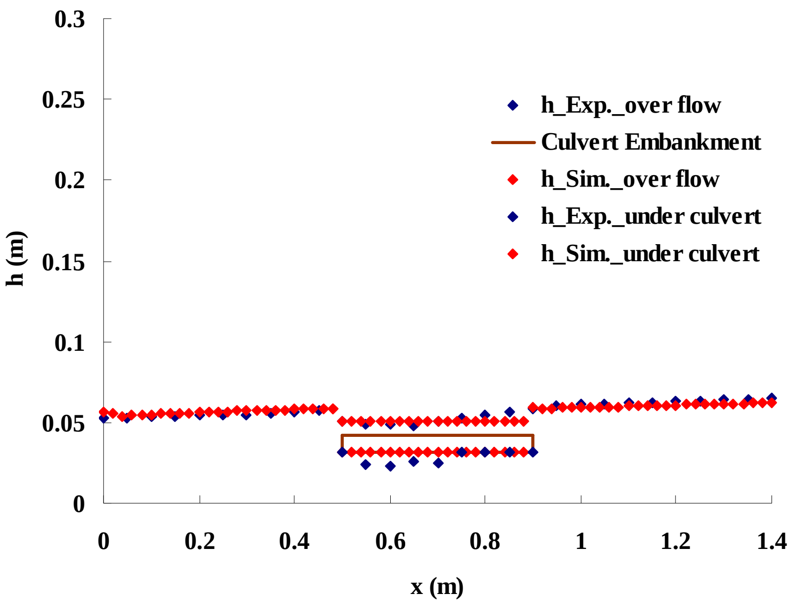

(d) Run 4

Figure 7.11 A verification of water depth along the centerline for both experimental and numerical results.

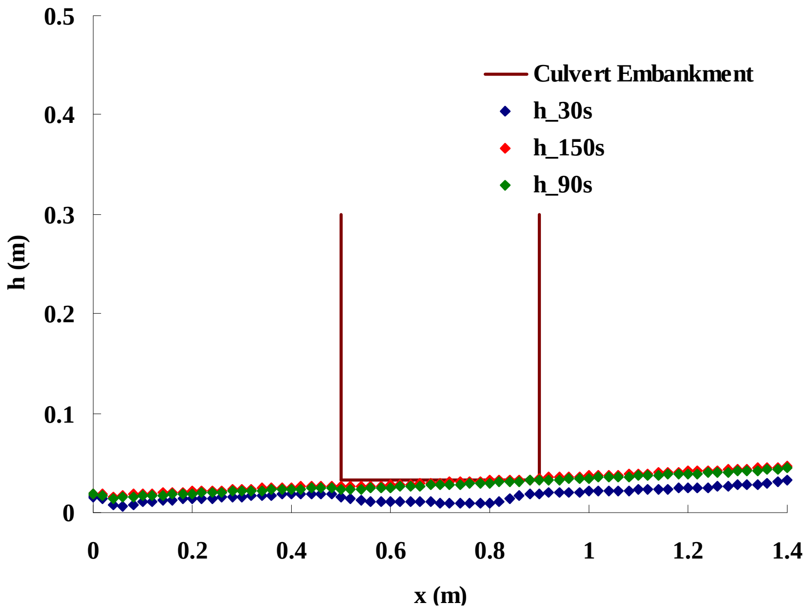

Figure 7.12 The interaction between free surface open channel flow and pressurized flow in Run 1.

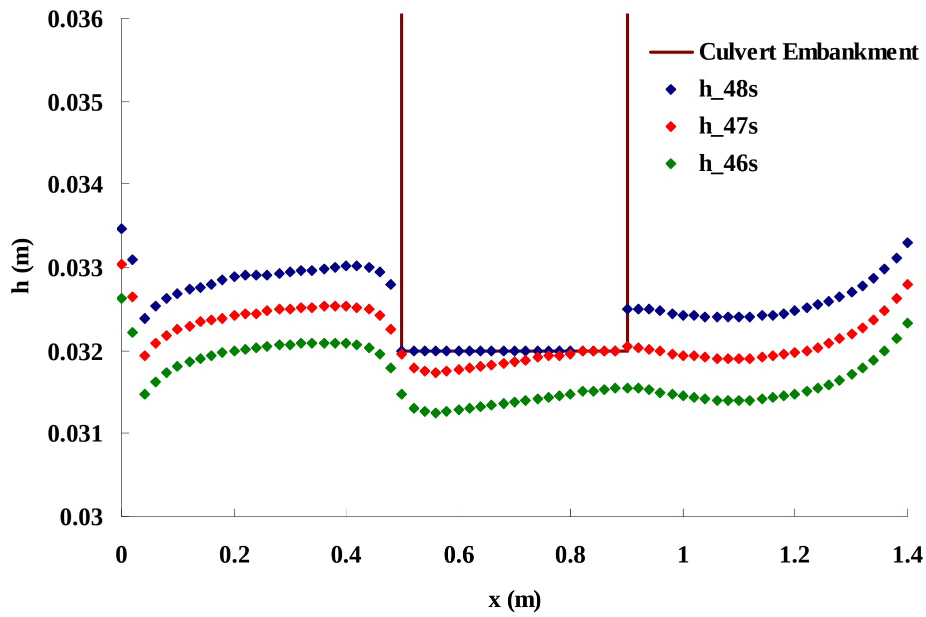

Figure 7.13 The hydraulic transients of the interface between free surface open channel flow and pressurized flow in Run 2.

7.5 Summary

Some of the typical features of flow through and over culverts are studied by fundamental hydraulic experiment, which can represent flow during flash floods under highways in Oman. A two-dimensional numerical simulation model is proposed and applied under the experimental conditions, considering the interaction between open channel free surface flow and pressurized flow. We focus on testing the typical flow patterns in the full/partial full pressurized flow. As a comparison between observed and calculated results, good agreements are found between them. The model can be improved further to get better results and to be applicable to simulate flows around actual box culverts during flash floods.

Chapter 8

CONCLUSIONS AND RECOMMENDATIONS

8.1 Conclusions

This study focuses on some practical analysis of river flows around selected hydraulic structures. Theoretical, experimental and numerical analysis are applied in studying the water flow behavior around these structures.

Firstly, a one-dimensional numerical model is applied to study the formation of the hydraulic jumps downstream steps in a multi backward-facing steps flume. The model is carried out under experimental conditions for three cases: water-free-fall step, partially-submerged step and fully-submerged step. Different grid sizes were tested in this model in order to avoid the numerical oscillation at the immediate downstream of the step and also to improve the reproduction of the hydraulic jump. The calculated results were compared with experimental results. Even the matching between the results is not so accurate, but this numerical model has the ability to represent the hydraulic jumps clearly especially when the smaller grid size is used.

By continuing the study of the flow over the backward-facing steps, two-dimensional physical experiments were implemented in a wooden flume including a single step with a sudden expansion immediately downstream the step. More attention was given to the generation of the oblique shock waves downstream the steps due to the abrupt expansion in the geometry of the channel. A depth-averaged two-dimensional numerical model is established under the observed conditions, using the finite volume method on a curvilinear grid. The results were plotted in the form of surface contour with velocity vectors, which can present the formation of the oblique shockwaves clearly. The backwater effect due to the increase of water depth at the downstream end is also considered. The results were verified with the measured results in the form of the water variation along the centerline, in which it has a good matching for the fully-submerged step condition. However, due to the numerical oscillation that occurred downstream the step, the calculated results for the partially-submerged case don’t represent properly the measured one.

The ecological changes on the ecosystem of the Kamo River also presented in this research by studying the relation between the habitat of an endangered bird called Kamogawa-Chidori and the sandbar formation in the river course. A two-dimensional open channel flow numerical model is executed to simulate both of water flow and sediment transport. It is used to simulate alternate sandbars, in addition to the deposition of sediment downstream the backward-facing steps structures. The model can represent efficiently the scenario of the sandbar formation in the Kamo River. By comparing and analyzing the observed and calculated results, we can conclude that, due to the widening of the main channel and the installation of series of backward-facing steps, the tractive force to transport sediment of riverbed has decreased. As a result, the bare sandbars without vegetation have also decreased. Therefore, the number of chidori birds has been decreased rapidly in the Kamo River.

A part of this thesis contains some description of the spatial variations of flow depth in steady open channel flows downstream of a disturbance attached at one side wall of a flume. The theoretical analysis shows that by using the linearlized equations of two-dimensional shallow flows, periodic wavy patterns exist for supercritical flows (Froude number >1), but the amplitude of periodic wavy patterns always attenuates downstream direction. We noted also that by increasing the Froude number, the attenuation rate also increases. These theoretical results are verified by hydraulic experiments and a two-dimensional numerical model which is executed under the conditions of hydraulic experiments. The numerical calculated results almost fit with the observed one in term of the amplitude of the hydraulic wave length.

Some trials to analyze flash floods especially in arid area in order to propose some mitigations for floods in future researches are described at the last two chapters of this research (Chapter 6 and Chapter 7). In Chapter 6, a theoretical analysis is carried out to investigate the possibility of reproducing flash floods with a high Froude number by using one depth hydrograph at one site. The main output of this theory can be listed as follows. Linear analytical solution can be derived when the boundary conditions at upstream are linear function of time. If the boundary conditions at upstream are quadratic function of time, nonlinearity should be taken in account.

This thesis is ended with a two-dimensional numerical model which is proposed to represent flow during flash floods under highways in Oman. It is applied under observed conditions, considering the interaction between open channel free surface flow and pressurized flow. The typical flow patterns in the full/partial full pressurized flow were considered. Although we failed to make a good comparison between the calculated results and the experimental ones in some cases, the simulation model can reproduce the transition process reasonably for some other cases.

8.2 Recommendations

The work in the analysis of the spatial variations of flow depth in open channel flow around disturbance can be extended with further studies. Since the measured depth distributions show very anti-symmetric feature, the further investigation including the nonlinear effects is necessary to clarify the generation mechanism of anti-symmetric depth distributions. The numerical model needs to be improved to give better results, by considering the vertical acceleration in the future studies.

Since there is a lack in the studies in flash floods in arid areas, physical and numerical models needs to be extended for simulating extreme storms. Therefore, the numerical model which is used in simulating water flow through and over box culverts can be improved further to get better results and to represent flow during flash floods through box culverts.

REFERENCES

Armaly, B., Durst, F., Pereira, J. and Schonung, B. 1983. Experimental and theoretical investigation of backward facing step flow. *J. Fluid Mech.*: 127, 473-496.

Barkley, D., Gomes, M. and Henderson, D. 2002. Three-dimensional instability in flow over a backward-facing step. *J. Fluid Mech.*: 473, 167-190.

Blondeaux, P. and Seminara, G. 1985. A unified bar-bend theory of river meanders, *J. Fluid Mech.*: 15, 449-470.

Callander, R. 1969. Instability and river channels. *J. Fluid Mech.*: 36, 465-480.

Carling, P. 1995. Flow-separation berms downstream of a hydraulic jump in a bedrock channel. *Geomorphology*: 11, 245-253.

Carrasco-Milian, A., Vionnet, C. & Valentine, E. 2009. Experimental study on the formation of alternate bars with fixed and loose banks. *Proceedings RCEM2009*: pp.773-778.

Chang, H. 1982. Mathematical model for erodible channels. *J. Hydraul. Div. Am. Soc. Civ. Eng.*: 108(5), 678-689.

Chanson, H. 1995. Hydraulic Design of stepped Cascades, channels, weirs and spillways. *Pergamon, Oxford, UK*, 292 pages.

Chanson, H. 2000. Introducing originally and innovation in engineering teaching: the hydraulic design of culverts. *EUR. J. ENG. ED.*:Vol. 25, No.4, 377-391.

Chow, V.T. 1959. Open channel hydraulics. *McGraw-Hill Book Co.*, Inc., New York, N.Y.

Denham, M. and Patrick, M. 1974. Laminar flow over a downstream facing step in a two dimensional flow channel. *Trans. Inst. Chem. Engrs.*: 52, 361-367.

Gharangik, A.M. and Chaudhry, M.H. 1991. Numerical simulation of hydraulic jump. *Journal of Hydraulic Engineering*: 117, 1195-1211.

Ghia, K., Osswald, G. and Ghia, U. 1989. Analysis of incompressible massively separated viscous flows using unsteady Navier-Stokes equations. *Intl. J. Numer. Meth. Fluids.*: 9, 1025-1050.

Gill, M. A. 1979. Hydraulics of rectangular vertical drop structures. *J. Hydraul. Res.*: 17, 289-302.

Hager W.H. 1992. Energy Dissipators and Hydraulic Jump. *Kluwer, Dordrecht*.

Han, Q. 1980. A study on the non-equilibrium transportation of suspended load. *Proc., Ist. Int. Symp. on River Sedimentation*, IRTCES, Beijing.

Hasegawa, K. 1981. Bank-erosion discharge based on a non-equilibrium theory. *Proc. Of the JSCE,* No. 316, pp.37-50 (in Japanese).

Hirt, C.W. and Cook, J.L. 1972. Calculating three-dimensional flows around structures and over rough terrain. *J. Computational Physics*: Vol.10, pp.324-340.

Holly, F.M. and Rahuel, J.L. 1990. New numerical/physical framework of mobile-bed modeling, Part I: Numerical and physical principles. *J. Hydraul. Res.*: 21(4), 401-416.

Hosoda, T., Inoue, K. and Tada, A. 1993. Hydraulic transients with propagation of interface between open channel free surface flow and pressurized pipe flow. *Proc. International Symp. On Computational Fluid Dynamics.*, Sendai: Vol. I, pp.291-296.

Hosoda, T., Tada, A. Inoue, K. and Kitahara, M. 1993. Hydraulic analysis of unsteady flows with propagation of interface between free surface flow and pressurized pipe flow, *Journal of Hydraulic, Coastal and Environmental Engineering, JSCE*: No.503/2-29, pp.89-97(in Japanese).

Hosoda, T. and Nishihama, M. 2006. Fundamental characteristics of high velocity flows in a sinuous meandering channel in the vicinity of resonance. *Proceeding of the International Conference on Fluvial Hydraulics (River Flow 2006)*, Lisbon, Portugal, 6-8 September 2006, Vol. 1, pp. 209-218.

Hosoda, T., Muramaki, T., Onda, S., Iwata, M., Puay, H. And Sibayama, Y. 2010. Some considerations on computational method of flood flow without both upstream and downstream boundary conditions. *Annual Journal of Hydraulics Engineering, JSCE*: Vol. 54, pp.1159-1164 (in Japanese).

Inoue, K. 1986. Study on numerical method of unsteady open channel flows and its application in hydraulic engineering field, *PhD thesis, Kyoto University* (in Japanese).

Jaeggi, M., 1984. Formation and effects of alternate bars. *J. Hydraulic Eng.*: 110, 142-156.

Leopold, L. & Wolman, M., 1957. River channel patterns: braided, meandering, and straight. *U.S. Geologicla Survey Prof. Paper* 282-B.

Lin, X. 1999. Flash floods in arid and semi-arid zones, *IHP-V Technical Documents in Hydrology*, no.23.

Matsushima, F., Matsushima, T. and Hagihara, Y. 2007. Relationship between GES system and distribution of aquatic birds in an urban river environment. *The Japan Section of the Regional Science Association International (JSRSAI).*

Meyer-Peter, E. & Muller, R. 1984. Formulas for bed-load transport, *Proc. 2nd JAHR Congr.,* Stockholm: pp.39-64.

Moore, W., L. 1943. Energy loss at the base of freefall. *Trans. Am. Soc. Civ. Eng.*: 108, 1343-1360.

Nagata, N., Hosoda, T. and Muramoto, Y. 2000. Numerical analysis of river channel processes with bank erosion. *Journal of Hydraulic Engineering*: 126, 243-252.

Ohyagi, S., Obara, T., Hoshi, S., Cai, P. and Yoshihashi, T. 2002. Diffraction and re-initiation of detonations behind a backward-facing step. *Shock Waves*: 12, 221-226.

Parker, G. 1976. On the cause and characteristics scales of meandering and braiding in rivers. *J. Fluid Mech.*: 76(3), 457-480.

Puay, H. and Hosoda, T. 2009. Fundamental characteristics of open channel flows near an abrupt expansion with oblique shockwaves. *Cd-proc. of the 23rd Symposium computational fluid dynamics, Japan Society of Fluid Mechanics*, G8-4, Sendia, 2009.

Rand, W. 1955. Flow geometry at straight drop spillways. *Proceedings, ASCE*, Vol. 81, No.791, pp. 1-13.

Rajaratnam, N. and Chamani, M.R. 1995. Energy loss at drops. *J. of Hyd. Res. IAHAR*, Vol. 33, No.3, pp. 373-384.

Shimizu, Y. and Itakura, T. 1989. Calculation of flow and bed deformation with general non-orthogonal coordinate system. *J. Hydraul. Eng. ASCE*: 115(3), 367-384.

Shimizu, Y., Yamaguchi, H. and Itakura, T. 1990. Three-dimensional computation of flow and bed deformation. *J. Hydraul. Eng. ASCE*: 116(9), 1090-1108.

Smith, K. and Ward, R. 1998. Floods – physical processes and human impacts. *John Wiley and Sons, Chichester.*

Spasojevic, M., and Holly, F. 1990. 2-D bed evolution in natural watercourses-New simulation approach. *J. Waterw., Port, Coastal, Ocean Eng.*: 116(4), 425-443.

Struiksma, N., Olesen, K.W., Flokstra, C. and de Vriend, H.J. 1985. Bed deformation in curved alluvial channels, *J. of Hydraulic Research*: 23, 57-79.

Thomas, W. 1982. Chapter 18: Mathematical modeling of sediment movement. Gravel-bed rivers, R. D. Hey et al., eds., Wiley, New York.

White, M. P. 1943. Discussion of Moore (1943). *Trans. Am. Soc. Civ. Eng.*: 108, 1361-1364.

Wongsa, S. and Shimizu, Y. 2006. Numerical simulation of bed deformation in meandering and braiding channels. *Vietnam-Japan Estuary Workshop*, Hanoi, Vietnam: pp. 72-77.

Wu, W., and Vieira, D. 2002. One-dimensional channel network model CCHEID 3.0-Technical manual. Technical Rep. No. NCCHE-TR-2002-1, National Center for Computational Hydroscience and Engineering, the Univ. of Mississippi, University, Miss.

Wu, W. 2004. Depth-averaged two-dimensional numerical modeling of unsteady flow and non-uniform sediment transport in open channels. *Journal of Hydraulic Engineering, ASCE*: 130, 1013-1024.

Yamamoto, K. 1994. Potamology of alluvial rivers. Sankaido, 1994 (in Japanese).

Zhou, J., G. and Stansby, P., K. 1999. 2D shallow water flow model for the hydraulic jump. *Int. J. Numer. Meth. Fluids*: 29, 375-387.

Zolezzi, G., M. Guala, D. Termini, and G. Seminara 2005. Experimental observations of upstream over-deepening. *J. Fluid Mech.*: 531, 191–219.